
AFRL-AFOSR-VA-TR-2016-0327

# (HEL/MRI) 3D META-OPTICS FOR HIGH ENERGY LASERS

**Glenn Boreman**
**UNIVERSITY OF NOTH CAROLINA AT CHARLOTTE**

**09/13/2016**
**Final Report**



Air Force Research Laboratory
AF Office Of Scientific Research (AFOSR)/ RTB1
Arlington, Virginia 22203
Air Force Materiel Command

# REPORT DOCUMENTATION PAGE

*Form Approved*
*OMB No. 0704-0188*



**PLEASE DO NOT RETURN YOUR FORM TO THE ABOVE ORGANIZATION.**

| 1. REPORT DATE *(DD-MM-YYYY)* | 2. REPORT TYPE | 3. DATES COVERED *(From - To)* |
|---|---|---|
| 09/13/2016 | Final Technical Report | 09/30/10 - 09/14/2016 |

**4. TITLE AND SUBTITLE**
(HEL-MRI) 3D Meta-Optics for High Energy Lasers

**5a. CONTRACT NUMBER**
FA9550-10-1-0543

**5b. GRANT NUMBER**
FA9550-10-1-0543

**5c. PROGRAM ELEMENT NUMBER**

**6. AUTHOR(S)**
Boreman, Glenn
Johnson, Eric

**5d. PROJECT NUMBER**

**5e. TASK NUMBER**

**5f. WORK UNIT NUMBER**

**7. PERFORMING ORGANIZATION NAME(S) AND ADDRESS(ES)**
University of North Carolina at Charlotte
9201 University City Boulevard
Charlotte, NC 28223-0001

**8. PERFORMING ORGANIZATION REPORT NUMBER**

**9. SPONSORING/MONITORING AGENCY NAME(S) AND ADDRESS(ES)**
USAF, AFRL DUNS 143574726
AF OFFICE OF SCIENTIFIC RESEARCH
875 NORTH RANDOLPH STREET, RM 3112
ARLINGTON VA 22203

**10. SPONSOR/MONITOR'S ACRONYM(S)**
AFOSR/PKR3

**11. SPONSOR/MONITOR'S REPORT NUMBER(S)**

**12. DISTRIBUTION/AVAILABILITY STATEMENT**
Distribution A

**13. SUPPLEMENTARY NOTES**

**14. ABSTRACT**

The research team was composed of University of North Carolina at Charlotte, Clemson University, University of Texas at Arlington, and University of Minnesota. The scope of this program was to change the way components are designed and fabricated for high energy laser (HEL) applications, engineering electromagnetic fields in 3D dielectric structures. We exploited various methods based on periodic and aperiodic electromagnetic modeling techniques to accurately determine the fields throughout the structures. We developed methods of optimizing the desired spatial, spectral and polarization properties for specific platforms representational of High Energy Laser Components. Fabrication of structures with this degree of complexity requires unique methods of lithographic processing, etching and deposition. Advanced deposition methods were explored to provide high quality coatings based on atomic layer deposition and enable the engineering of structures on a monolayer by monolayer basis, with particular attention to laser-damage mechanisms. Test-beds were used to demonstrate the concept functionality, including solid-state-laser and fiber-laser based HEL systems. From and educational perspective we created a virtual laboratory for 3D Meta-Optics.

**15. SUBJECT TERMS**
Metamaterials; transformational optics; computational electromagnetics; high-energy laser components

| 16. SECURITY CLASSIFICATION OF: | | | 17. LIMITATION OF ABSTRACT | 18. NUMBER OF PAGES | 19a. NAME OF RESPONSIBLE PERSON |
|---|---|---|---|---|---|
| a. REPORT | b. ABSTRACT | c. THIS PAGE | UU | | Glenn Boreman |
| | | | | | 19b. TELEPHONE NUMBER *(Include area code)* 704-687-8173 |

Reset

## INSTRUCTIONS FOR COMPLETING SF 298

**1. REPORT DATE.** Full publication date, including day, month, if available. Must cite at least the year and be Year 2000 compliant, e.g. 30-06-1998; xx-06-1998; xx-xx-1998.

**2. REPORT TYPE.** State the type of report, such as final, technical, interim, memorandum, master's thesis, progress, quarterly, research, special, group study, etc.

**3. DATES COVERED.** Indicate the time during which the work was performed and the report was written, e.g., Jun 1997 - Jun 1998; 1-10 Jun 1996; May - Nov 1998; Nov 1998.

**4. TITLE.** Enter title and subtitle with volume number and part number, if applicable. On classified documents, enter the title classification in parentheses.

**5a. CONTRACT NUMBER.** Enter all contract numbers as they appear in the report, e.g. F33615-86-C-5169.

**5b. GRANT NUMBER.** Enter all grant numbers as they appear in the report, e.g. AFOSR-82-1234.

**5c. PROGRAM ELEMENT NUMBER.** Enter all program element numbers as they appear in the report, e.g. 61101A.

**5d. PROJECT NUMBER.** Enter all project numbers as they appear in the report, e.g. 1F665702D1257; ILIR.

**5e. TASK NUMBER.** Enter all task numbers as they appear in the report, e.g. 05; RF0330201; T4112.

**5f. WORK UNIT NUMBER.** Enter all work unit numbers as they appear in the report, e.g. 001; AFAPL30480105.

**6. AUTHOR(S).** Enter name(s) of person(s) responsible for writing the report, performing the research, or credited with the content of the report. The form of entry is the last name, first name, middle initial, and additional qualifiers separated by commas, e.g. Smith, Richard, J, Jr.

**7. PERFORMING ORGANIZATION NAME(S) AND ADDRESS(ES).** Self-explanatory.

**8. PERFORMING ORGANIZATION REPORT NUMBER.** Enter all unique alphanumeric report numbers assigned by the performing organization, e.g. BRL-1234; AFWL-TR-85-4017-Vol-21-PT-2.

**9. SPONSORING/MONITORING AGENCY NAME(S) AND ADDRESS(ES).** Enter the name and address of the organization(s) financially responsible for and monitoring the work.

**10. SPONSOR/MONITOR'S ACRONYM(S).** Enter, if available, e.g. BRL, ARDEC, NADC.

**11. SPONSOR/MONITOR'S REPORT NUMBER(S).** Enter report number as assigned by the sponsoring/ monitoring agency, if available, e.g. BRL-TR-829; -215.

**12. DISTRIBUTION/AVAILABILITY STATEMENT.** Use agency-mandated availability statements to indicate the public availability or distribution limitations of the report. If additional limitations/ restrictions or special markings are indicated, follow agency authorization procedures, e.g. RD/FRD, PROPIN, ITAR, etc. Include copyright information.

**13. SUPPLEMENTARY NOTES.** Enter information not included elsewhere such as: prepared in cooperation with; translation of; report supersedes; old edition number, etc.

**14. ABSTRACT.** A brief (approximately 200 words) factual summary of the most significant information.

**15. SUBJECT TERMS.** Key words or phrases identifying major concepts in the report.

**16. SECURITY CLASSIFICATION.** Enter security classification in accordance with security classification regulations, e.g. U, C, S, etc. If this form contains classified information, stamp classification level on the top and bottom of this page.

**17. LIMITATION OF ABSTRACT.** This block must be completed to assign a distribution limitation to the abstract. Enter UU (Unclassified Unlimited) or SAR (Same as Report). An entry in this block is necessary if the abstract is to be limited.

# Introduction:

The scope of this program was to radically change the way novel components are designed and fabricated for High Energy Applications. This *3D Meta-Optics platform was and is essentially engineering the electromagnetic fields in 3D dielectric structures*. The results of which have provided a class of transformational optical components that can be integrated at all levels throughout a High Energy Laser system. In order to address this research goal, the following objectives were established prior to this program initiation:

- *Development of Design Tools for 3D Meta-Optics* – Complex electromagnetic modeling tools are a requirement for these types of optical elements. The team exploited various methods based on periodic and aperiodic techniques to accurately determine the fields and how they interact throughout the structures. This included methods of optimizing the structure for desired spatial, spectral and polarization properties and exploiting these tools for specific platforms representational of High Energy Laser Components.

- *Development of Novel Fabrication methods for 3D Meta-Optics* – Fabrication of structures with this degree of complexity requires unique methods of lithographic processing, etching and deposition. This team investigated advanced lithographic methods for patterning structures and subsequent methods for transferring the patterns into a variety of substrates. Advanced deposition methods were explored to provide high quality coatings based on Atomic Layer Deposition and enable the engineering of structures on a monolayer by monolayer basis. Additionally, laser damage physics was explored to develop an understanding of the physics associated with meta-optics.

- *Establish Application Platforms for 3D Meta-Optics* – Test-beds were identified and utilized to demonstrate the functionality of the concepts as proposed. These included solid state laser systems and fiber laser based systems for a variety of optical components at various levels throughout a typical High Energy Laser Platform.

- *Education of 3D Meta-Optic Engineers* – Given the complexity and potential power of the proposed technology, a key objective of the Team was to create a virtual laboratory for 3D Meta-Optics. This program was effective in translating the concepts into course content, laboratories for experimentation, and more than 6 PhD's granted on related subjects.

This final report summarizes the archival publications (> 45) as listed below, followed by brief summaries of the major research accomplishments of the team composed of the University of North Carolina at Charlotte, Clemson University, University of Texas at Arlington, and the University of Minnesota.

**Archival Publications Generated under this MRI Grant:**


1. Morgan, Kaitlyn, Keith Miller, Wenzhe Li, Yuan Li, Brandon Cochenour, and Eric Johnson. "Free Space Propagation of Concentric Vortices through Underwater Turbid Environments." In Propagation Through and Characterization of Atmospheric and Oceanic Phenomena, pp. W2A-3. Optical Society of America, 2016.
2. Baghdady, Joshua, Keith Miller, Kaitlyn Morgan, Matthew Byrd, Sean Osler, Robert Ragusa, Wenzhe Li, Brandon M. Cochenour, and Eric G. Johnson. "Multi-gigabit/s underwater optical communication link using orbital angular momentum multiplexing." Optics express 24, no. 9 (2016): 9794-9805.
3. Li, Yuan, Wenzhe Li, J. Miller, and Eric G. Johnson. "Multiplexing and Amplification of 2 μm Vortex Beams with a Ho: YAG Rod Amplifier." (2016).
4. Yuan Li, Zeyu Zhang, Wenzhe Li, Keith Miller, and Eric Johnson, "Ho:YAG Rod Amplifier For High Order Vortex Modes," in Frontiers in Optics 2015, OSA Technical Digest (Optical Society of America, 2015), paper FTu3G.3.
5. Yuan Li, Zeyu Zhang, Wenzhe Li, Keith Miller, and Eric Johnson, "Simultaneous Amplification of Multiple 2 μm Vortex Beams," in Advanced Solid State Lasers, OSA Technical Digest (online) (Optical Society of America, 2015), paper ATu2A.45.
6. Yuan Li, Zeyu Zhang, J. Keith Miller, and Eric Johnson. "Ho: YAG rod amplifier for vortex beams." In Photonics Conference (IPC), 2015, pp. 321-322. IEEE, 2015.
7. Keith Miller, Yuan Li, Wenzhe Li, Ramesh Shori, and Eric Johnson. "Pulsed Amplification of 2 μm Concentric Vortex Beams." In CLEO: Science and Innovations, pp. STu1M-7. Optical Society of America, 2016.
8. Guoliang Chen; Kyu Jin Lee; Robert Magnusson, "Periodic photonic filters: theory and experiment," Optical Engineering 55(3), 037108 (2016). doi: 10.1117/1.OE.55.3.037108.
9. 2. Jae Woong Yoon, Seok Ho Song, and Robert Magnusson, "Critical field enhancement of asymptotic optical bound states in the continuum," Scientific Reports, vol. 5, article no. 18301, pp. 1–8, November 22, 2015. doi: 10.1038/srep18301 (2015).
10. A. Sincore, J. Cook, W. Li, E. Johnson, J. Bradford, L. Shah, M. Richardson, "Beam propagation of Gaussian and Annual Beams at 2 μm in the presence of thermal lensing," CLEO Science and Innovations 2016, paper JTh2A.77
11. L. N. Taylor and J. J. Talghader, "Subsampling phase retrieval for rapid thermal measurements of heated microstructures," Optics Letters, vol. 41, pp. 3189–3192, 2016.
12. P. R. Armstrong, M. L. Mah, K. D. Olson, L. N. Taylor, and J. J. Talghader, "Reduction of thermal emission background in high temperature microheaters," Journal of Micromechanics and Microengineering, vol. 26, 055004, 2016.

13. Byrd, M.; Pung, A.; Johnson, E.; Kyu Lee; Magnusson, R.; Binun, P.; McCormick, K., "Wavelength Selection and Polarization Multiplexing of Blue Laser Diodes," in Photonics Technology Letters, IEEE , vol.27, no.20, pp.2166-2169, Oct.15, 15 2015
14. Indumathi Raghu Srimathi, Yuan Li, William F. Delaney, and Eric G. Johnson, "Subwavelength grating based metal-oxide nano-hair structures for optical vortex generation," Opt. Express 23, 19056-19065 (2015)
15. Li, Yuan, Zeyu Zhang, Wenzhe Li, Jerome Miller, and Eric Johnson. "Ho: YAG Rod Amplifier ForHigh Order Vortex Modes." In Frontiers in Optics, pp. FTu3G-3. Optical Society of America, 2015.
16. Li, Yuan, Zeyu Zhang, Wenzhe Li, Keith Miller, and Eric Johnson. "Simultaneous Amplification of Multiple 2 μm Vortex Beams." In Advanced Solid State Lasers, pp. ATu2A-45. Optical Society of America, 2015.
17. A. Brown, A. Ogloza, L. Taylor, J. Thomas, and J. Talghader, "Continuous wave laser damage and conditioning of particle-contaminated optics," Applied Optics, vol. 54, no. 16, pp. 5216-5222, 2015.
18. E. McKee, E. Maddox, L. Shah, R. Gaume, M. Richardson, "Rapid thermo-optical quality assessment of laser gain media," C.C.C. Willis, J.D. Bradford, J. Haussermann, Optical Materials Express 5, 6 (2015) 1389-1398.
19. L. Shah, R.A. Sims, P. Kadwani, C.C.C. Willis, J.B. Bradford, A. Sincore, M. Richardson, "High-power spectral beam combining of linearly polarized Tm:fiber lasers," Applied Optics 54, 1 (2015) 757-762.
20. Byrd, M.; Woodward, R.; Pung, A; Johnson, E.; Lee, K.; Magnusson, R.; McCormick, K.; Binun, P., "Blue laser diode wavelength selection with a variable reflectivity resonant mirror," Photonics Technology Letters, IEEE (2014).
21. Kyu J. Lee, Jerry Giese, Laura Ajayi, Robert Magnusson, and Eric Johnson, "Resonant grating polarizers made with silicon nitride, titanium dioxide, and silicon: Design, fabrication, and characterization," Opt. Express 22, 9271-9281 (2014).
22. M. Gebhardt, C. Gaida, P. Kadwani, A. Sincore, N. Gerlich, L. Shah, M. Richardson, "High peak power mid-IR ZnGeP2 optical parametric oscillator pumped by Tm:fiber master oscillator power amplifier system," Opt. Lett 39 1212-1215 (2014).
23. Lucas N. Taylor, Andrew K. Brown, Aaron J. Pung, Eric G. Johnson, Joseph J. Talghader, "Continuous-wave laser damage of uniform and nanolaminate hafnia and titania optical coatings," Optics Letters, vol. 38, no. 21 pp. 4292-4295, Nov 1, 2013.
24. Indumathi Raghu Srimathi, Aaron J. Pung, Yuan Li, Raymond C. Rumpf, and Eric G. Johnson, "Fabrication of metal-oxide nano-hairs for effective index optical elements," Opt. Express 21, 18733-18741 (2013).
25. Pung, A. J., Srimathi, I. R., Li, Y., & Johnson, E. G. (2013, September). Fabrication Method for Encapsulation of Low-Index, Narrowband Guided-Mode

Resonance Filters. In Photonics Conference (IPC), 2013 IEEE (pp. 227-228). IEEE.
26. Pung, A. J., Carl, S. R., Srimathi, I. R., & Johnson, E. G. (2013). Method of fabrication for encapsulated polarizing resonant gratings. IEEE Photon. Technology Letters, 25(15), 1432-1434.
27. L. N. Taylor, A. K. Brown, A. J. Pung, E. G. Johnson, and J. J. Talghader, "Laser Damage of Nanolaminate HfO2 and TiO2 Optical Coatings," Technical Digest of the 2013 OSA Optical Interference Coatings Conference, Whistler, British Columbia, Canada, June 2013, 3 pages.
28. Robert Magnusson, Tanzina Khaleque, and Mohammad J. Uddin, "Optical filters enabled by the Rayleigh anomaly: Theory and experiment," IEEE Photonics Conference 2013, Bellevue, Washington, September 8–12, 2013.
29. Robert Magnusson, "Flat-top resonant reflectors with sharply delimited angular spectra: an application of the Rayleigh anomaly," Optics Letters, vol. 38, no. 6, pp. 989–991, March 15, 2013.
30. Yuan Li; Srimathi, I.R.; Woodward, R.H.; Pung, A.J.; Poutous, M.K.; Shori, R.K.; Johnson, E.G., "Guided-Mode Resonance Filters for Wavelength Selection in Mid-Infrared Fiber Lasers," Photonics Technology Letters, IEEE , vol.24, no.24, pp.2300,2302, Dec.15, 2012.
31. Indumathi Raghu Srimathi, Menelaos K. Poutous, Aaron J. Pung, Yuan Li, Ryan H. Woodward, Eric G. Johnson, and Robert Magnusson, "Mid-Infrared Guided Mode Resonance Reflectors for Applications in High Power Laser Systems," IEEE Photonics Conference 2012, Burlingame, California, September 23–27, 2012
32. Yuan Li, Ryan H. Woodward, Indumathi Raghu Srimathi, Aaron J. Pung, Menelaos K. Poutous, Eric G. Johnson, and Ramesh Shori," 2.78 μm Fluoride Glass Fiber Laser Using Guided Mode Resonance Filter as External Cavity Mirror," IEEE Photonics Conference 2012, Burlingame, California, September 23–27, 2012.
33. K. J. Lee, J. Giese, I. L. Ajayi, R. Magnusson, and E. Johnson, "Resonant dielectric-grating polarizers for normal incidence operation," IEEE Photonics Conference 2012, Burlingame, California, September 23–27, 2012, paper MX2.
34. Lawrence Shah, R. Andrew Sims, Pankaj Kadwani, Christina C.C. Willis, Joshua B. Bradford, Aaron Pung, Menelaos K. Poutous, Eric G. Johnson, and Martin Richardson, "Integrated Tm:fiber MOPA with polarized output and narrow linewidth with 100 W average power," Opt. Express 20, 20558-20563 (2012).
35. Roth, Z.A., Srinivasan, P., Poutous, M.K., Pung, A.J., Rumpf, R.C., Johnson, E.G." Azimuthally Varying Guided Mode Resonance Filters." Micromachines, 3, 180-193 (2012).
36. Pung, M. Poutous, R. Rumpf, Z. Roth, and E. Johnson, "Monolithic, Low-index Guided-mode Resonance Filters: Fabrication and Simulation," in Optical Fabrication and Testing, OSA Technical Digest (online) (Optical Society of America, 2012), paper OTu4D.6.

37. Yuan Li, Ryan H. Woodward, Indumathi Raghu Srimathi, Menelaos K. Poutous, Ramesh K. Shori, and Eric G. Johnson, "Guided mode resonance filter as wavelength selecting element in Er:ZBLAN fiber laser," 2012 OSA Specialty Optical Fibers (SOF) Topical Meeting, 1361447.
38. Indumathi Raghu, Menelaos K. Poutous, Aaron Pung, Yuan Li, Ryan Woodward, and E. G. Johnson, "Design and Fabrication of Mid-IR Guided Mode Resonance Filters," 2012 OSA Integrated Photonics Research, Silicon and Nano Photonics (IPR) Topical Meeting, 1361387.
39. Robert Magnusson, "Spectrally dense comb-like filters fashioned with thick guided-mode resonant gratings," Optics Letters, vol. 37, no. 18, pp. 3792-3794, September 15, 2012.
40. K. J. Lee, J. Curzan, M. Shokooh-Saremi, and R. Magnusson, "Guided-Mode Resonance Polarizers With 200-nm Bandwidth," Optical Society of America Frontiers in Optics, OSA's 95th Annual Meeting, San Jose, California, October 16–20, 2011; published in Frontiers in Optics, OSA Technical Digest, paper FWU2.
41. Kyu J. Lee, James Curzan, Mehrdad Shokooh-Saremi, and Robert Magnusson, "Resonant wideband polarizer with single silicon layer," Applied Physics Letters, vol. 98, no. 21, pp. 211112-1–211112-3, May 25, 2011.
42. Aaron J. Pung, Menelaos K. Poutous, Raymond C. Rumpf, Zachary A. Roth, and Eric G. Johnson, "Two-dimensional guided mode resonance filters fabricated in a uniform low-index material system," Opt. Lett. 36, 3293-3295 (2011).
43. Pung, M. Poutous, Z. Roth, and E. Johnson, "Fabrication of Low Contrast Homogenous Guided Mode Resonance Filters," in CLEO:2011 - Laser Applications to Photonic Applications, OSA Technical Digest (CD) (Optical Society of America, 2011), paper JTuI24.
44. N. T. Gabriel and J. J. Talghader, "Thermal conductivity and refractive index of hafnia-alumina nanolaminates," Journal of Applied Physics, vol. 110, 043526 (2011); doi:10.1063/1.3626462 (8 pages).
45. Menelaos K. Poutous, Aaron Pung, Pradeep Srinivasan, Zachary Roth, Eric G. Johnson, "Polarization selective, graded-reflectivity resonance filter, using a space-varying guided-mode resonance structure," Optics Express 2010, Vol. 18, No. 26, 27764-27776 (Dec 2010).

**Students:** PhD students supported:

1. Zachary Roth

Space Variant Guided Mode Resonance Filters
PhD, Optical Science and Engineering, University of North Carolina at Charlotte, May 2012

2. Aaron Pung

Encapsulated and Monolithic Resonant Structures for Laser Applications
PhD, Photonics, Clemson University, Dec 2013

3. Guoliang Chen

Design and fabrication of guided-mode resonance devices
PhD, Electrical Engineering, UT Arlington, Dec 2015.

4. Luke Taylor

Going Deeper into Laser Damage: Experiments and Methods for Characterizing Materials in High Power Laser Systems.
Ph.D. in Electrical and Computer Engineering, University of Minnesota, May 30, 2016.

5. Manoj Niraula

Guided-mode resonant filters and reflectors: Principles, design, and fabrication
PhD, Electrical Engineering, UT Arlington, May 2016.

6. Indumathi Raghu Srimathi

Meta-Optics for High Power Lasers
PhD, Electrical Engineering, Clemson University, Dec 2016

7. S. Andrew Sims

Development of thulium fiber lasers for high average power and high peak power operation
University of Central Florida, College of Optics & Photonics, 2013

## Design and Fabrication of Meta-Optics (Clemson and UT Arlington)

**Mid-infrared Guided-Mode Resonance Reflectors for Applications in High Power Laser Systems**

A Guided-Mode Resonance Filter (GMRF) [1, 2] is an optically resonant structure consisting of a subwavelength grating (SWG) and a high-index waveguide layer fabricated on a supporting substrate. The devices work based on the electromagnetic coupling of a narrow spectral band from the incident light, due to diffraction by the SWG into leaky waveguide modes, which in turn re-couples to the SWG, and exit the device from the incidence side. This effect results in high reflectance at the desired wavelength band of interest. The advantage of such devices over conventional optical filters such as the Distributed Bragg Reflectors (DBR) is in their simple construction. The GMRF devices require few layers of dielectrics, compared to their conventional counterpart, while providing equivalent or better spectral characteristics, in terms of achieving high reflectance, suppressed sideband reflections, polarization sensitivity and, arbitrarily narrow resonance linewidths [3,4]. The cost and complexity associated with the GMRF device fabrication is greatly reduced, when wafer scale fabrication is used. This project presents the design and fabrication of mid-infrared optical reflection filters, based on GMRF principles, for applications at 2.94μm and based on hafnium dioxide ($HfO_2$)/quartz material system. The wavelength band has potential applications in high power lasers based on Er:YAG which are used in sensors, dentistry, laser surgery, spectroscopy, IR countermeasures, etc. [5]. Narrowband devices based on a silicon nitride/soda lime glass system [6] and, broadband GMRF devices based on a

germanium/fused silica system [7] have been reported for use in absorption spectroscopy, VCSELs, and similar mid-IR applications.

*Device Design* – The mid-IR GMRF devices described in this paper use a 2D periodic square lattice of holes to form the SWG. The period of the SWG is 1.90μm and the hole radius is 0.76μm. The major challenge in the mid-IR arises due to the limited choices of material substrates that have little or no absorption and the fabrication challenges of such material systems using conventional lithographic techniques. A material system that has low absorption and an adequate refractive index contrast would be the ideal choice for high reflectance mirrors.

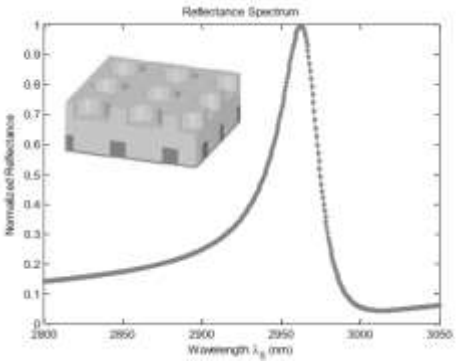


Fig. 1. Spectral reflectance of the GMRF device simulated using RCWA, with a peak resonance wavelength at 2962.5nm and FWHM of 35nm. (Inset) – Profile of the square periodic lattice for the GMRF device with period 1.90μm, hole radius 0.76μm, SWG depth of 270nm and HfO2 (light shaded region) overcoated layer thickness of 556nm, on a quartz substrate (dark shaded region).

Infrared grade quartz substrates (Heraeus Infrasil 301) were used for this design. The SWG was formed into the quartz substrate ($n_{sub}$ = 1.4206), with a depth of 270nm. $HfO_2$ ($n_{wg}$ = 1.9695) conformally overcoats the patterned SWG and, functions as the waveguide layer, is chosen for its high power damage threshold properties. The device structure is shown in the inset of Figure 1. The device spectral performance was simulated using Rigorous Coupled Wave Analysis (RCWA), assuming plane wave illumination. The symmetry of the square lattice SWG, results in polarization insensitive device design at normal incidence. The simulated resonance has a peak reflectance of 100% at 2962.5nm with a FWHM of 35nm (Fig. 1).

*Device Fabrication and Testing* – The devices were fabricated on a double-sided polished quartz substrate using conventional lithographic processes. The square lattice SWG with period 1.9μm and hole radius of 0.76μm was exposed on a photoresist coated substrate using a GCA g-line 5X-reduction stepper. The surface topography was transferred into the substrate to a depth of 270nm using a Unaxis Versaline Inductively Coupled Plasma (ICP) oxide etcher. The high index waveguide layer consisting of 556nm of $HfO_2$ was deposited on the patterned substrate using Ion Beam Sputtering (IBS). Fig. 2 shows a cross-sectional SEM image of the fabricated device. The RCWA simulations were modified to account for the rounding and funneling that occurs during the device

fabrication, to track the resonance wavelength change more precisely, accounting for changes in the effective index of the dielectric layers.

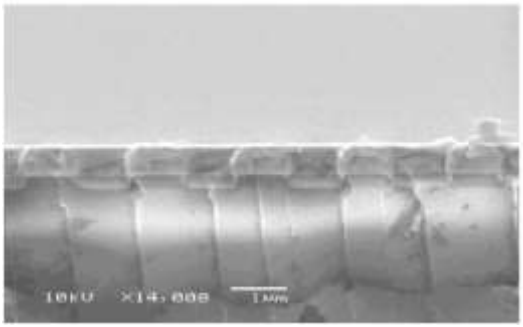

Fig. 2. Cross-sectional SEM micrograph of the fabricated mid-IR GMRF device. The rounding of HfO2 layer deposited on quartz substrate can be clearly seen from the micrograph.

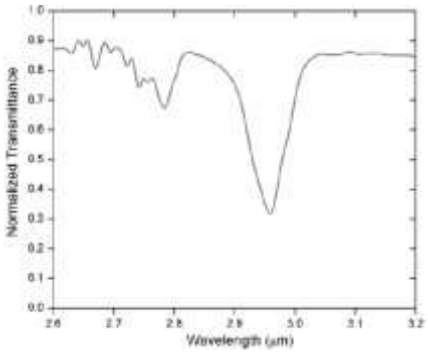


Fig. 3. Measured transmittance spectrum of mid-IR GMRF devices at normal incidence. The minimum in transmission is at 2954nm with a FWHM of 45nm. The spectrum looks identical for both TE and TM polarization states.

The transmission at normal incidence was measured using J. A. Woollam's IR-VASE ellipsometer. The experimentally measured resonance has a minimum in transmission at 2954nm and it has a FWHM of 45nm (Fig. 3). The minimum transmittance of the fabricated device was approximately 30%. Both the TE and TM polarization states produce a similar response and can be used for applications in optical systems that require polarization insensitive components.

*Conclusions* – The fabrication of mid-infrared reflectors, based on guided mode resonance device design, utilizing a hafnium dioxide/quartz material system was presented. The modified simulations accounting for the structure variations arising during fabrication is in a good agreement with the experimentally determined transmittance spectrum. The periodic 2D symmetry of the SWG helped in fabrication of polarization insensitive devices. The mirrors have a high reflectance around 2.94μm making them a viable choice for use as external wavelength selective feedback elements in an Er: YAG laser system that has potential applications in the fields of spectroscopy and laser surgery.

*References*

[1] S. S. Wang and R. Magnusson, "Theory and applications of guided mode resonance filters," Appl. Opt. **32**, 2606-2613 (1993).
[2] Z. S. Liu, S. Tibuleac, D. Shin, P. P. Young, and R. Magnusson, "High-efficiency guided-mode resonance filter," Opt. Lett.**23**, 1556- 1558 (1998).
[3] Raymond C. Rumpf and Eric G. Johnson, "Modeling fabrication to accurately place GMR resonances," Opt. Express **15**, 3452-3464 (2007).
[4] M. K. Poutous, Z. Roth, K. Buhl, A. Pung, R. C. Rumpf, and E. G. Johnson, "Correlation of fabrication tolerances with the performance of guided-mode-resonance micro-optical components," in Advanced Fabrication Technologies for Micro/Nano Optics and Photonics II, (SPIE, San Jose, CA, USA, 2009), pp. 72050Y–72059.
[5] Dominic Faucher, Martin Bernier, Nicolas Caron, and Real Vallee, "Erbium-doped all-fiber laser at 2.94 μm," Opt. Lett. **34**, 3313-3315 (2009).
[6] Anil K. Kodali, Matthew Schulmerich, Jason Ip, Gary Yen, Brian T. Cunningham, and Rohit Bhargava, "Narrowband midinfrared reflectance filters using Guided Mode Resonance", *Analytical Chemistry* **2010** *82* (13), 5697-5706.
[7] Juha M. Kontio, Janne Simonen, Kari Leinonen, Markku Kuittinen, and Tapio Niemi, "Broadband infrared mirror using guided-mode resonance in a subwavelength germanium grating," Opt. Lett. **35**, 2564-2566 (2010).

*Publication* – I. R. Srimathi, M. K. Poutous, A. J. Pung, Y. Li, R. H. Woodward, E. G. Johnson, and R. Magnusson, "Mid-infrared guided-mode resonance reflectors for applications in high power laser systems," in *Proceedings of IEEE Photonics Conference IPC* (IEEE, 2012), pp.822-823.

## Fabrication Method for Encapsulation of Low-Index, Narrowband Guided-Mode Resonance Filters

Highly reflective, narrowband optical components are essential components in modern laser systems. Given their influence over the characteristics of the laser cavity, device versatility and robustness are strongly desired. In comparison, distributed Bragg reflectors (DBR) utilize multiple layers of alternating materials to produce broadband reflectance, and are of limited use at off-normal angles of incidence. Alternatively, guided-mode resonance filters (GMRFs) exploit phase matching to produce a strong narrowband resonance [1]. However, conventional GMRF designs leave critical features of the structure exposed to the environment, exposing the device to contamination or damage.

We present a method of fabrication to fully encapsulate a resonant waveguide grating. The device geometry is designed such that the thickness of the protective cladding layer is decoupled from the resonance wavelength. Optically, the resonance in the leaky waveguide is a result of phase matching between the grating vector components and the guided modes in the buried grating layer [2]. Thinly coated resonant gratings were first explored as a means of suppressing the sidebands of the resonance [3]. Although a thin cladding layer can act as a thin protective layer and AR coating, the cladding must be significantly thicker to sufficiently protect the device from contamination and leave the resonance wavelength unaffected.

To obtain the desired reflectance profile, an ideal structure was simulated using rigorous coupled-wave analysis [4]. The ideal device geometry and spectral response are shown in Fig. 1. Simulations suggest that resonance location becomes decoupled from the cladding thickness when the cladding reaches a minimum height of 1500 nm, as shown in Fig. 1.

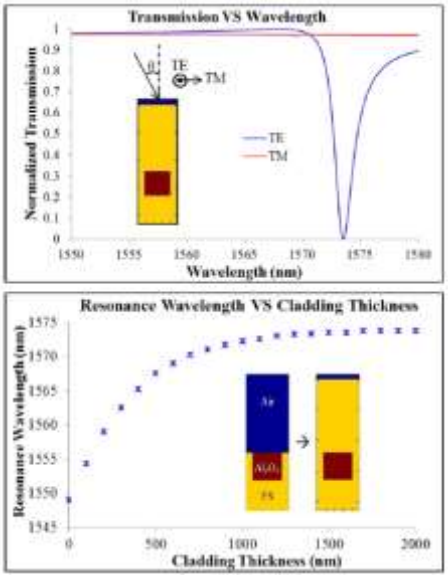


Fig. 1. (Top) Transmission versus wavelength is plotted for an ideal encapsulated geometry (shown in inset). (Bottom) The convergence of the resonance wavelength is shown as a function of cladding thickness.

In the ideal geometry, aluminum oxide ($Al_2O_3$) pillars are embedded in a fused silica grating and coated with silicon oxide ($SiO_x$). The grating has a lateral period and ridge width of 950 nm and 475 nm. The thickness of the cladding and grating layers are 2000 nm and 550 nm, respectively. The device is simulated with at a 10° angle of incidence, yielding complete reflection at 1573.5 nm. The full-width at half-maximum of the TE resonance is 2 nm.

*Fabrication & Experiment* – Prior to device fabrication, 1 mm thick fused silica substrates were cleaned with a piranha solution. SPR 700 photoresist was spun onto the primed substrates to a thickness of 1 μm. Initial approximations of the exposure parameters were obtained using KLA-Tencor's lithography simulation software. Following a post applied bake, the photoresist was patterned on a GCA I-line 5X reduction stepper tool, creating an array of devices each 100 $mm^2$ in area. After the post-exposure bake, the photoresist was developed on a Hamatech-steag HMP 900 developer tool utilizing 726 MiF developer. Prior to the transfer etch, a pre-etch descum was performed with a Plasmalab 80 Plus to eliminate remaining photoresist in the grating trenches. The pattern was transferred 550 nm into the substrate with an Oxford 82 etcher. An Oxford 100 tool was used to perform an oxygen clean to eliminate remaining photoresist on the substrate.
Atomic layer deposition (ALD) on an Oxford OpAL tool conformally coated the etched grating with 350 nm of $Al_2O_3$. This coating fills the etched structure and planarizes above the grating. An STS III-V plasma etcher selectively removed the planar Al2O3 layer. To prevent over-etching into the waveguide, 40 nm of alumina was left unetched. Finally, plasma-enhanced chemical vapor deposition (PECVD) was used to deposit 2000 nm of SiOx on the surface of the device. To eliminate interference fringes caused by the top and bottom interfaces, an antireflection coating of silicon nitride (Si3N4) and SiOx was deposited on the backside of the wafer. A cross-section SEM of the fabricated device is shown in the inset of Fig. 2.

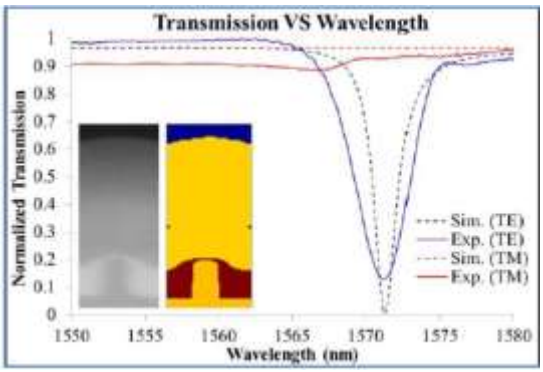


Fig. 2. Transmission versus wavelength is plotted for the fabricated structure and its equivalent simulation profile. The inlay shows the cross-section SEM of the fabricated device (left) and the imported MATLAB refractive index profile (right).

Fabrication of this geometry hinges on the conformal nature of the ALD deposition. As the length of the deposition time increases, all surfaces of the grating are equally coated; given a sufficiently long deposition, etched trenches of any aspect ratio can be filled. In

contrast with other coating schemes, this eliminates the risk of encapsulating unwanted air pockets [5, 6].

Spectral testing was performed by coupling light from a broadband ASE between two 300 μm fiber collimators. The randomly polarized incident light is passed through a linear polarizer to pre-determine the incidence state of polarization. The polarizer can be rotated to examine both polarization states. Similarly, the devices can be tilted to ensure optimal alignment; the angle of incidence was similar to that of the initial simulations. The transmission signal through the device was normalized to the transmitted signal through the wafer next to the device. The signal was evaluated with an optical spectrum analyzer. Fig. 2 compares the experiment and simulation data for the fabricated device. In TE polarization, 13% of the incident light was transmitted at resonance, demonstrating a strong extinction ratio ($R_{TE}/R_{TM}$) between the two polarization states. No appreciable resonance was seen in orthogonal (TM) polarization.

Simulation accuracy of the fabricated structures was improved by directly importing cross-section SEM data to modify the refractive index profile of the device. For TE polarization, simulations predict complete reflection at 1571.25 nm, with a 1.75 nm FWHM. Experimentally, the TE resonance is at 1571.21 nm, with a 3.1 nm FWHM. Difference between the spectral width of the experiment and theory is due to slight modulation of the grating. This modulation arises during the exposure step in the fabrication process. These modulations cause the transmitted signal to be integrated over slight variations in the resonance. This gives the effect of a broadened resonance.

*Conclusions* – Successful fabrication, simulation, and experimental confirmation of an encapsulated resonant structure whose resonance wavelength is independent of the device's cladding thickness was demonstrated. Extending this principle, it is possible to increase the height of the cladding as with two bonded substrates. In this case, the resonant structure would be encapsulated between two substrates, yielding a strong resonance while being protected from external damage.

*References*


[1] S. S. Wang and R. Magnusson (1993, May). "Theory and applications of guided-mode resonance filters," *Appl. Opt.32 (14),* 2606-2613.

[2] S. Boonruang, A. Greenwell, and M. G. Moharam (2006, March). "Multiline two-dimensional guided-mode resonant filters," *Appl. Opt.45 (22),* 5740-5747.

[3] S. S. Wang and R. Magnusson (1995, May). "Multilayer waveguide-grating filters," *Appl. Opt. 34 (14).*

[4] M.G. Moharam and T.K. Gaylord (1981, July). "Rigorous coupled-wave analysis of planar-grating diffraction," *J. Opt. Soc. Am. 71 (7),* 811-818.

[5] A.J. Pung, M.K. Poutous, Z.A. Roth, and E.G. Johnson, "Fabrication of low contrast homogenous guided mode resonance filters," presented at the Quantum Electronics and Laser Science Conference, Baltimore, Maryland, United States, May 1, 2011.

[6] A.J. Pung, M.K. Poutous, R. Rumpf, Z.A. Roth, and E.G. Johnson (2011, Aug.). "Two-dimensional guided mode resonance filters fabricated in a uniform low-index material system," *Opt. Lett. 36 (4),* 436-438.

*Publication* – A. J. Pung, I. R. Srimathi, Y. Li, and E. G. Johnson, "Fabrication method for encapsulation of low-index, narrowband guided-mode resonance filters," in *Proceedings of IEEE Photonics Conference IPC* (IEEE, 2013), pp.227-228.

## ***Fabrication of Subwavelength Grating Based Optical Nano-Hairs Using ALD Nano-Patterning***

Subwavelength gratings (SWGs) based artificial dielectric elements are used to obtain the same optical functionalities as a conventional diffractive optical element (DOE). SWGs have lateral periods smaller than the wavelength of the incident light, and the grating layer can be approximated as a homogeneous layer based on effective medium theory (EMT) [1]. The effective index structures should be capable of providing amplitude and phase modulation (0-2$\pi$) to fully mimic the functionalities of a DOE. The phase modulation is typically obtained by varying the fill fraction of the planar grating layer in a specific fashion based on the intended application [2]. Many of the investigated structures have been based on plasmonics [3] or high contrast grating structures [4]. Plasmonic metasurfaces suffer from high intrinsic absorptions and limit the efficiencies of the fabricated device. In contrast, dielectric metasurfaces can provide high diffraction efficiencies but have not been explored in much detail due to the aspect ratio requirements of the devices. Optical nano-hair structures have been realized on fully dielectric platforms in [5]. This is important for miniaturization and integration of refractive optical elements.
The geometry of the optical nano-hair based devices is shown in Fig. 1. Optical nano-hair structures are composed of pillars partially embedded into the substrate. The phase variation in transmission is obtained by modulating the fill fraction of devices. Overall phase obtained from these devices is a combination of the two regions present above and below the substrate. The devices can be realized with a single material or multiple materials in each of the cylindrical posts. The devices are fabricated by exploiting the conformal coating nature of the atomic layer deposition (ALD) tool. Precise thickness control is obtained since the chemical reactions leading to the formation of the films are self-limiting. This gives rise to excellent step coverage and conformal deposition even on high aspect ratio structures.

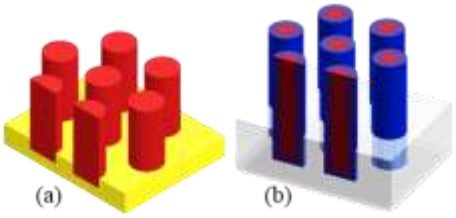


Fig 1. Geometry of an optical nano-hair based structure. (a) single material, and (b) multiple material based devices.

*Numerical Simulations* – When an optical wave is incident on this device, depending on the fill fraction it encounters, there is a phase delay that is induced. This property can be used on a gradient fill fraction pattern within the same device to tailor the spatial properties of the transmitted beam. The material system chosen for this study consisted of fused silica substrate with hafnium dioxide ($HfO_2$) nano-hair structures. The choice of the materials is dependent on the wavelength of operation and the final targeted application. The variation of the effective index becomes more linear with the fill fraction of the subwavelength grating if the spatial period is a lot smaller compared to the incident wavelength ($\Lambda << \lambda_o$), as seen in Fig. 2. The effective refractive indices of the devices

can be engineered to obtain wavefront control of transmitted beams. A 2D grating structure has been used that results in a polarization insensitive response.

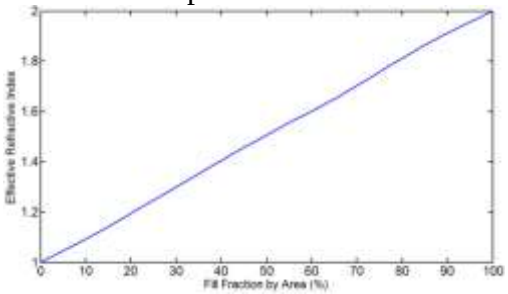


Fig. 2. Variation of effective refractive index of a 2D hexagonal lattice at $\lambda_o$ = 2.1 μm. The lateral period of the grating was 1.0 μm. The grating material is hafnia which is surrounded by air.

The spectral properties of the devices are simulated using rigorous coupled wave analysis (RCWA) [6]. The lateral period of the hexagonal grating lattice was fixed as 1.0 μm. Fused silica was chosen as the substrate material. The height of the hafnia cylindrical post above the substrate was 4.0 μm, while the thickness of the supporting base below the substrate was 1.0 μm. The parameters were chosen such that the entire 2π phase variation can be obtained in the transmitted beam when the fill fraction of the subwavelength grating is varied from 40% to 80%. High peak transmittance (> 89%) can be obtained with this material combination for all the different fill fractions under consideration due to the inherent low-index contrast (~ 0.55) between them. The reported phase variation and transmission amplitude were calculated only from the zeroth diffracted order. The plot of the phase variation vs. the changing fill fraction has been shown in Fig. 3.

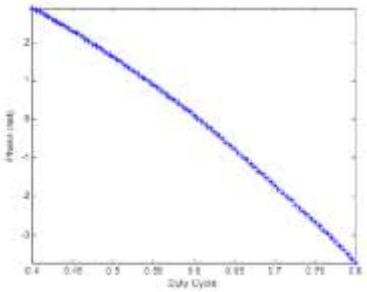

Fig. 3. Transmitted phase variation with duty cycle variation ranging from 40-80 %. The entire 2π phase variation is obtained.

*Fabrication Sequence* – A brief description of the fabrication sequence is shown in Fig. 4. The substrates are patterned with the necessary space variant grating patterns using a projection lithography tool. This step ensures that large area patterns and multiple devices can be obtained in one lithographic step on a substrate. Space variant patterns are obtained by superimposing a base hexagonal grating pattern with a secondary mask. The grating patterns are deep etched into the substrate (typically, fused silica) using a $CHF_3/O_2$ etch chemistry as shown in Fig. 4(a).

High aspect ratio structures are coated with metal oxides using an ALD tool (Fig. 4(b)). The role of the ALD tool is crucial in the fabrication sequence. The amount of material required to fill the holes entirely is equal to half the diameter of the holes irrespective of

the aspect ratio. This cannot be achieved in other non-conformal deposition processes. Planar layer obtained from the deposition process is back etched using a chlorine etch tool (Fig. 4(c)) to expose the completely filled holes. As a last step, the substrate around the filled holes are etched to obtain the optical nano-hair space variant grating patterns (Fig. 4(d)).

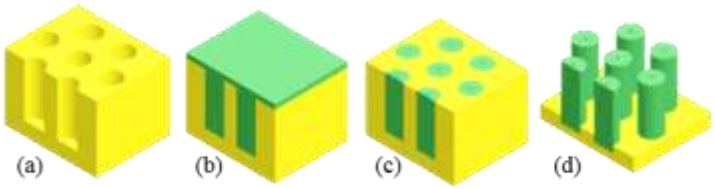


Fig. 4. Fabrication sequence of the optical nano-hair structures. (a) High aspect ratio structures in the substrate. (b) ALD used to fill in the holes with a metal-oxide completely. (c) Back etch the planar metal-oxide layer to expose the filled holes. (d) Etch the substrate around the holes to obtain the nano-hair structure.

Fused silica and alumina material system was used to generate cylindrical beam array patterns in [5] with an experimentally measured diffraction efficiency of over 93%. The concept was extended to a SWG based Fresnel lens structure as shown in Fig. 5. The material system used in this example consists of hafnia on a fused silica substrate. Fill fraction of the gratings are varied in each of the zones of the Fresnel lens structure (Fig. 5(b)). Fabrication sequence of these devices were very similar to the one shown in Fig. 4.

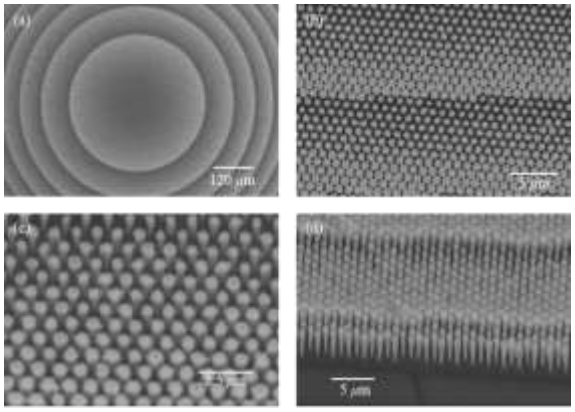

Fig. 5. (a) Fresnel lens structure. (b) Fill fraction variation seen in each of the zones of the Fresnel lens. (c, d) Fabricated hafnia nano-hair structures mimicking a lens profile. The grating material is hafnia which is surrounded by air.

To reduce the effects of stresses in a pure hafnia film, a laminate structure based on hafnia and alumina was used to fabricate multi-material optical nano-hair structures for generating an optical vortex beam as shown in Fig. 6. An azimuthal fill fraction variation was obtained by superimposing the hexagonal grating profile with a secondary vortex mask. Once the grating profile was obtained in the fused silica substrate (Fig. 6(b)), the high aspect ratio holes were coated with alternate layers of hafnia and alumina using an ALD tool. The presence of the alternate layers in the holes relaxes the aspect ratio requirements of the devices and also minimizes Fresnel losses in the effective index

structure. The planar metal oxide layer consisting of alumina and hafnia was etched using a $BCl_3$/Ar chemistry. As a final step, the substrate around the filled holes was etched to expose the multi-material nano-hair vortex patterns. Experimental testing of these devices showed a diffraction efficiency around 90%. The fully demonstrated concept can be extended to many geometries that can help realize arbitrary continuous and discrete phase functions in the transmitted beam profile.

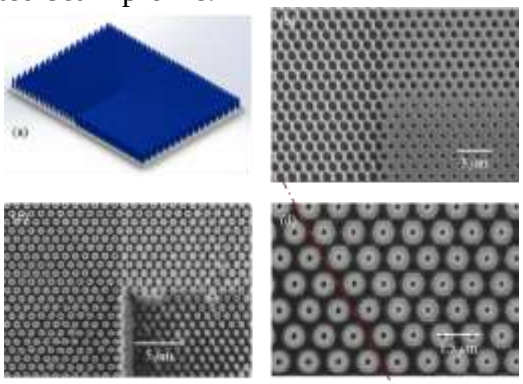

Fig. 6. (a) Optical nano-hair based vortex generator. (b) Azimuthal fill fraction variation of the vortex device. (c) Fabricated multi-material nano-hair vortex device. (d) Fill fraction variation and the presence of multiple material within each of the holes.

*Conclusions* – New device implementation based on an optical nano-hair based structure has been introduced. Working principle of the devices are based on effective medium theory approximation of the SWGs. Nano-patterning techniques and conformal coating nature of an ALD tool is exploited to form these novel nano-hair structures. Single material or multiple materials can be filled in each of the high aspect ratio holes to engineer the dispersion properties of the optical device. The space variant grating structure is obtained in a single lithographic step that eliminates the need for complex and precise alignment between the different layers. These composite structures can be extended to spectral and polarization control of optical waves.

*References*


[1] S. M. Rytov, "Electromagnetic Properties of a Finely Stratified Medium", Soviet Physics JETP 2, 466 – 475 (1956).

[2] Christophe Sauvan, Philippe Lalanne, and Mane-Si Laure Lee, "Broadband blazing with artificial dielectrics," Opt. Lett. 29, 1593-1595 (2004).

[3] P. Genevet, N. Yu, F. Aieta, J. Lin, M. A. Kats, R. Blanchard, M. O. Scully, Z. Gaburro, and F. Capasso, "Ultra- thin plasmonic optical vortex plate based on phase discontinuities," Appl. Phys. Lett. 100(1), 013101 (2012).

[4] Y. Yang, W. Wang, P. Moitra, I. I. Kravchenko, D. P. Briggs, and J. Valentine, "Dielectric meta-reflectarray for broadband linear polarization conversion and optical vortex generation," Nano Lett.14(3), 1394–1399 (2014).

[5] I. Raghu Srimathi, A. J. Pung, Y. Li, R. C. Rumpf, and E. G. Johnson, "Fabrication of metal-oxide nano-hairs for effective index optical elements," Opt. Express 21, 18733-18741 (2013).

[6] M. G. Moharam and T. K. Gaylord, "Rigorous coupled-wave analysis of planar-grating diffraction," J. Opt. Soc. Am. 71, 811-818 (1981).

*Publications* – a. I. R. Srimathi**,** A. J. Pung, E. G. Johnson, and R. C. Rumpf, "Optical nano-hairs for micro-optical applications," in *Proceedings of IEEE Photonics Conference IPC* (IEEE, 2013), pp. 478-479.
b. I. R. Srimathi, and E. G. Johnson, "Fabrication of Subwavelength Grating Based Optical Nano-Hairs Using ALD Nano-Patterning," in *Proceedings of IEEE Photonics Conference IPC* (IEEE, 2015), pp. 516-517.

***High-power laser testing of 3D meta-optics***

Many applications of modern optical systems rely heavily on the ability to customize the output beam of an optical system to fit the application requirements. Applications in telecommunications, for instance, place the operation wavelength at 1.55 μm while medical applications utilize 2.94 μm to take advantage of water absorption in the skin. 3D Meta-Optics are optical components that are based on the engineering of the electromagnetic fields in 3D dielectric structures. The results of which will provide a class of transformational optical components that can be integrated at all levels throughout a High Energy Laser system.
Additionally, operation in optical fibers and laser systems typically requires the use of a narrowband spectral selectivity. The beam shape can also play a vital role in the success of a device. For instance, a Gaussian beam profile may be optimal for investigating high power laser damage, while spatial multiplexing can take advantage of a non-Gaussian beam profile. If the components are to be used as out-couplers in bulk lasers, the optics must be able to operate at high power densities.

*Broadband Guided Mode Resonance Filters (GMRF)* – The first meta-optics device investigated was chosen to be a broadband GMRF [1]. The grating and waveguide layers are silicon and the substrate is modeled as silicon dioxide. The spectral response of this device can be computationally estimated using Rigorous Coupled-Wave Analysis (RCWA) [2].

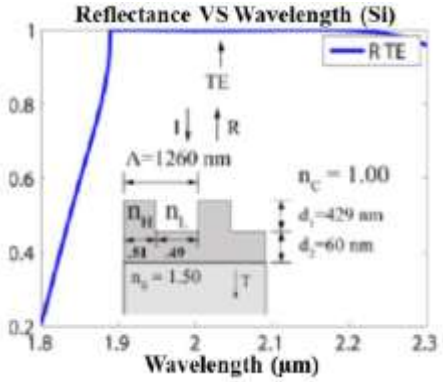


Fig. 1. Reflectance is plotted versus wavelength for a Silicon-based resonant structure.

The Si-based structure demonstrated a FWHM greater than 400 nm. The optimized grating period was found to be Λ=1270 nm with a grating duty cycle of 51%. The grating and waveguide thicknesses were found to be 429 nm and 60 nm, respectively. The refractive indices of the superstrate and substrate were simulated to be 1.00 and 1.50.

Once the optimized device parameters were obtained, the silicon-based device was fabricated using holographic lithography. Cleaned fused silica substrates were coated with a thin film of silicon prior to being coated with photoresist. A 266 nm laser was used in a two-beam holographic interference system to pattern the photoresist. The photoresist was then developed prior to a thin-film etching process, transferring the pattern into the silicon coating. The photoresist was then removed, leaving the final polarization sensitive device. To ensure a successful fabrication process, atomic force microscope (AFM) images were obtained. Subsequent experimental testing employed an IPG laser, tunable between 1.9 and 3 μm. Reflected power from the incident polarized beam was recorded as a function of wavelength on a power meter. The resonant structure was mounted on a rotational stage, to eliminate feedback into the laser cavity. The experiment is illustrated in Fig. 2; a comparison between the simulated and experimental data is shown in Fig. 3.

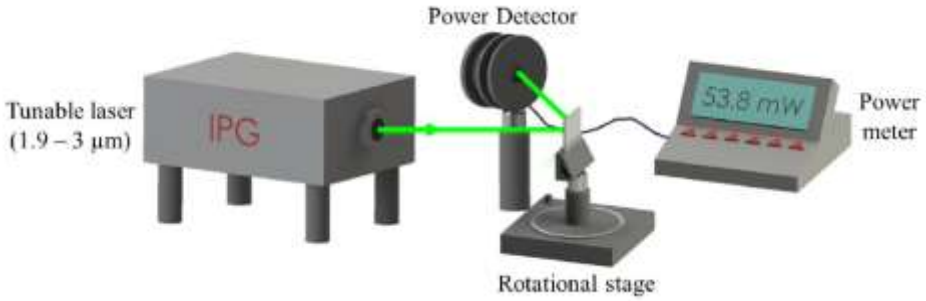


Fig. 2. The experimental arrangement is illustrated. An IPG laser, tunable between 1.9 and 3 μm, provides polarized illumination on the device. A rotational stage is used to ensure there is no feedback into the laser. Power measurements are taken with a detector to measure reflected power versus wavelength.

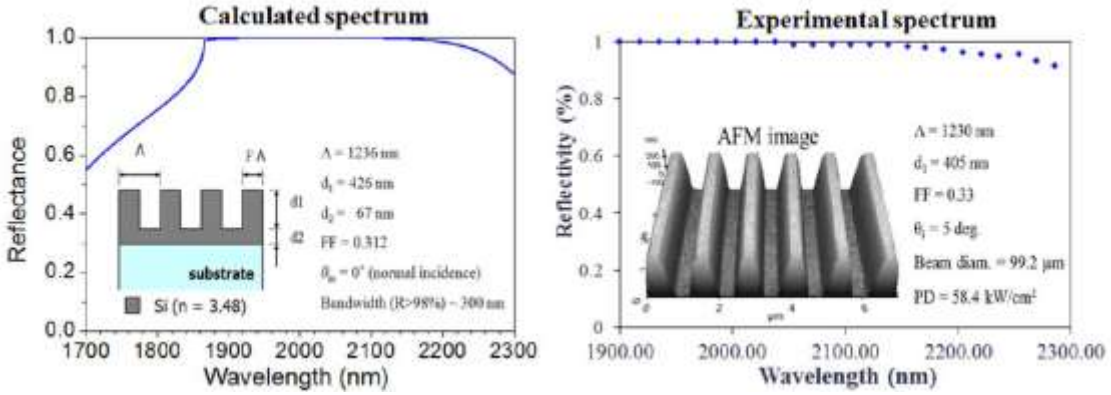


Fig. 3. (Left) Simulated reflectance is plotted versus wavelength. (Right) Experimental reflectivity is measured as a function of wavelength. The device geometry and fabrication parameters for the ideal and fabricated structures are shown as insets.

As illustrated in Fig. 3, the ideal structure has a lateral period and duty cycle of 1236 nm and 31.2%, respectively. The grating thickness and waveguide thickness were simulated to be 426 nm and 67 nm. Simulations were performed at normal incidence, with TE polarization. The AFM image of the fabricated device a lateral period of 1230 nm and 33% duty cycle. The grating thickness was measured to be 405 nm. With a 99.2 μm beam diameter, a power density of 58.4 kW/cm$^2$ was achieved. Experimental spectral measurements were found to agree well with the simulated data between 1.9 and 2.3 μm.

*Narrowband Guided Mode Resonance Filters* – To demonstrate spectral filtering, a single-layer GMRF geometry was explored. In contrast to the broadband resonant structure, the narrowband resonance device is designed for off-normal angle-of-incidence operation. This allows the device to be used for spectral beam combining as well as out-coupling for various laser systems. In order to achieve the narrow-linewidth profile, low contrast materials were used.

The low-index contrast design was simulated using RCWA. The reflectance versus wavelength is plotted for incident TE polarization. The ideal device is a single-layer waveguide grating. The linear grating has a lateral period and fill factor of 950 nm and 68%, respectively. The fused silica grating pillars are 900 nm tall and 304 nm wide. The grating grooves are filled with Aluminum Oxide (Al2O3). With an angle of incidence of 4.9 degrees, the device demonstrates a resonance at 1550 nm with a 2 nm FWHM as shown in Fig. 4 [3].

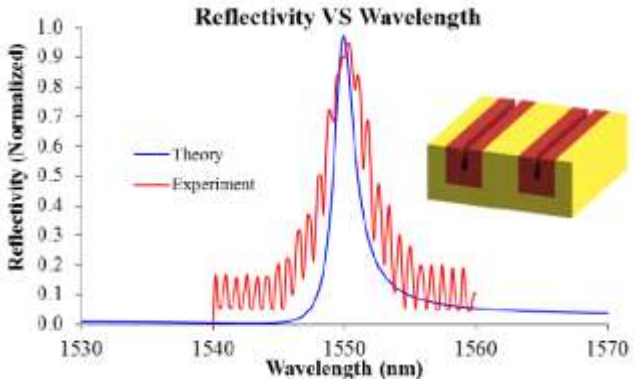


Fig. 4. Simulated reflectance is plotted versus wavelength for both theory and experiment. Incident light is polarized in TE plane (E-field along grating grooves). The inset illustrates the device geometry.

Device fabrication utilized conventional lithography techniques. A 4" diameter fused silica wafer is cleaned and primed before being coated with photoresist. The photoresist is patterned with an I-line stepper tool. The photoresist acts as an etch mask to transfer the linear grating pattern into the resist. At this point, the waveguide material ($Al_2O_3$) is deposited on the grating via atomic layer deposition (ALD). As the thickness of the deposition increases, the grooves fill equally from all directions. This eliminates unwanted air void formation during the deposition process. The deposition process is stopped short of completely filling the grating, and selectively etching off the top deposition layer. The final steps of the fabrication process are illustrated in Fig. 5.

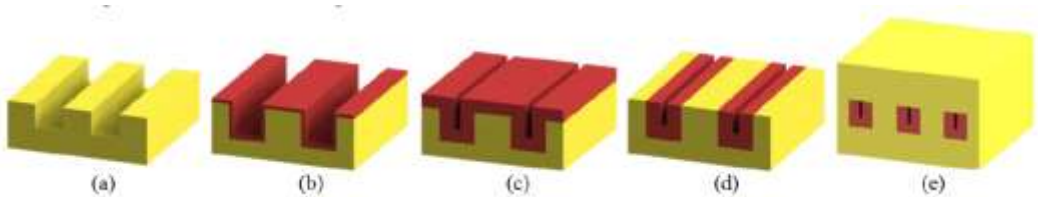


Fig. 5. Final steps of the fabrication process are illustrated for the narrowband resonant GMRF. Following initial fabrication steps, (a) patterned photoresist is transferred into the substrate. (b-c) The etched substrate is coated conformally via ALD deposition. (d) The top layer is selectively removed via III-V plasma etching. (e) Following the top layer removal, an optional cladding layer may be added to protect the resonant waveguide grating [3].

The CW source operates with a tunable semiconductor seed laser centered on 1.55 μm. The output beam is amplified and sent into collimating and refocusing optics. For high power testing, a lens combination was chosen that demonstrated a focused spot diameter of 90 μm, yielding a 244 kW/cm$^2$ power density. A knife edge profiling arrangement was installed alongside the lasing system that allowed the beam diameter to be measured at the point of incidence on the sample. The beam transmitted through the sample continues to a power detector, while the reflected signal is fed to a second power detector. In doing so, the power and reflectivity from the device may be measured in-situ. The two experimental arrangements are shown in Fig. 6.

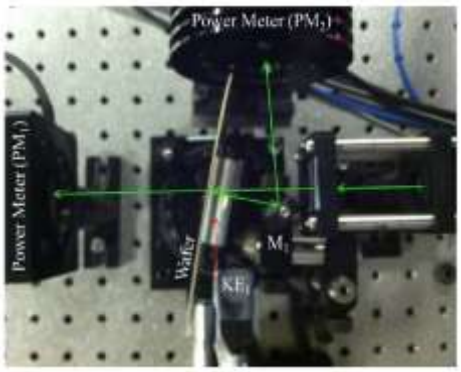


Fig. 6. Experimental arrangement is shown for the amplified CW semiconductor source.

Due to the small beam diameter, influence of the finite beam size on the device's reflectivity was investigated. Based on diffraction, it is known that the incident beam diameter is inversely proportional to the angular spread of the beam [4-6]. The angular spread was used with RCWA simulations to estimate the reflectance at various beam diameters ranging from 90 μm to 2.6 mm. Reflectivity was plotted versus beam diameter for simulation and experimental data, shown in Fig. 7. To eliminate finite beam effects on the spectral measurements, a beam size of 2.6 mm was used; the experimental measurements are shown overlapped with the ideal simulations in Fig. 4. It was found that the fringes are caused by interference produced within the substrate.

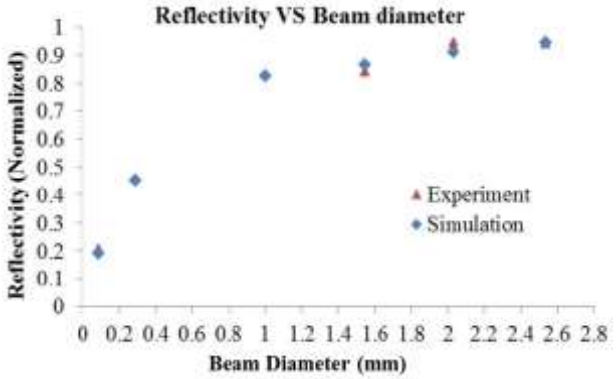


Fig. 7. Reflectivity is plotted against beam diameter for simulation and experimental data.

*Effective Index Structures* – Lastly, high-transmission meta-optic structures [7] were examined. With applications in beam conditioning and higher order mode coupling, the effecting index structures are capable of modifying the beam transmitted through the device. Simulations were performed for a range of duty cycles to ensure high transmission at 1.55 μm. The transmitted field was also simulated at the selected wavelength to demonstrate a non-Gaussian profile. Finally, simulations of the electric field inside the device were performed to demonstrate the effective index nature (no field confinement) within the device. These simulation results and the device geometry are shown in Fig. 8.

The fabrication of the nanohair structures utilized conventional microlithography. Fused silica substrates are coated with a chrome mask to aid in the etching process. The chrome is coated with photoresist, and a hexagonal grating is patterned with an I-line stepper tool. The pattern is transferred into the chrome; subsequently, the two materials act as an etch mask to transfer the pattern into the substrate. ALD deposition conformally fills the circular holes, forming a nearly planar layer of alumina on top of the grating. The top layer is selectively etched off, revealing the top of the pillars and the wafer substrate. A inductively coupled plasma is used to etch back the fused silica substrate, revealing the alumina pillars. The fabrication process is illustrated in Fig. 9. An SEM image of the fabricated device is shown in Fig. 10.

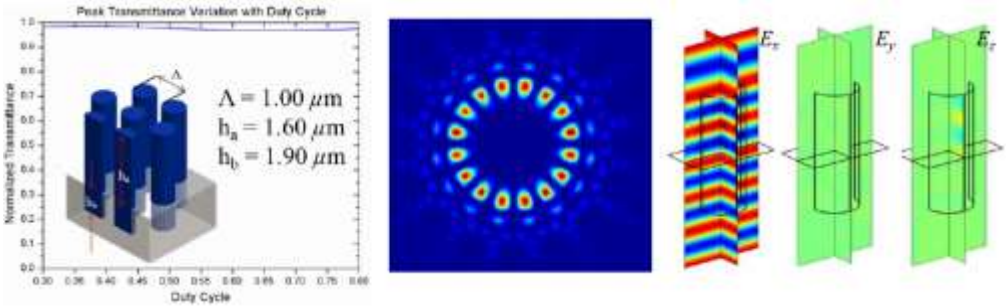


Fig. 8. (Left) Transmission versus duty cycle is plotted for an ideal nanohair geometry. The geometry and corresponding parameters are shown in the inset. (Middle) The simulated transmitted field profile is illustrated at 1.55 μm. (Right) The electric field is simulated along the X, Y, and Z planes of the device; no field confinement is observed.

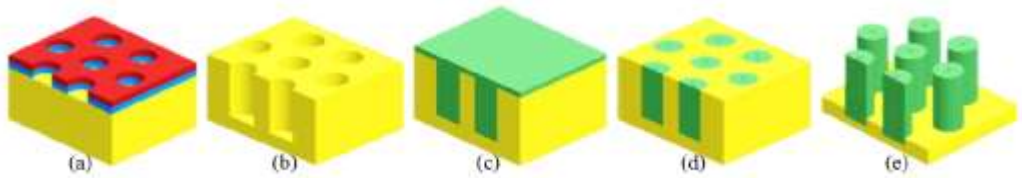


Fig. 9. Steps of the fabrication process are illustrated for the nanohair structure. A wafer coated with a thin layer of chrome is coated with photoresist. (a) The hexagonal grating pattern is transferred into the chrome mask prior to (b) the final transfer etch into the substrate. (c) ALD coating fills the cylindrical holes and forms a deposition layer over the grating. (d) The top layer is selectively etched away, before an RIE ICP etcher (e) removes the fused silica surrounding the nanohairs.

To experimentally verify the functionality of the device, an experiment similar to that shown in Fig. 6 was used with a collimated beam. The transmitted beam profile was obtained using a CCD array at 1.55 μm. The output beam was then modified to obtain a 94 μm beam diameter, yielding a power density of 206 kW/cm$^2$. The power in the incident beam was scaled, and the transmission through the device was measured. The transmitted power versus power density is shown in Fig. 10 along with an image of the transmitted beam profile from a larger collimated beam.

*Conclusions* – Responses of different kinds of optical devices were examined, and tested at high power densities exceeding 200 kW/cm$^2$. The fabricated broadband devices based on silicon on fused silica were tested experimentally, and shown to withstand 58 kW/cm$^2$, while achieving broadband resonance between 1.9 – 2.3 μm. Narrowband resonance devices also exhibited strong reflectivity around their designed wavelength. For the CW case, the device withstood power densities of 244 kW/cm$^2$. Finally, high transmission beam conditioning optics were fabricated and tested. Experimental results agree well with simulations, and were shown to withstand 206 kW/cm$^2$.

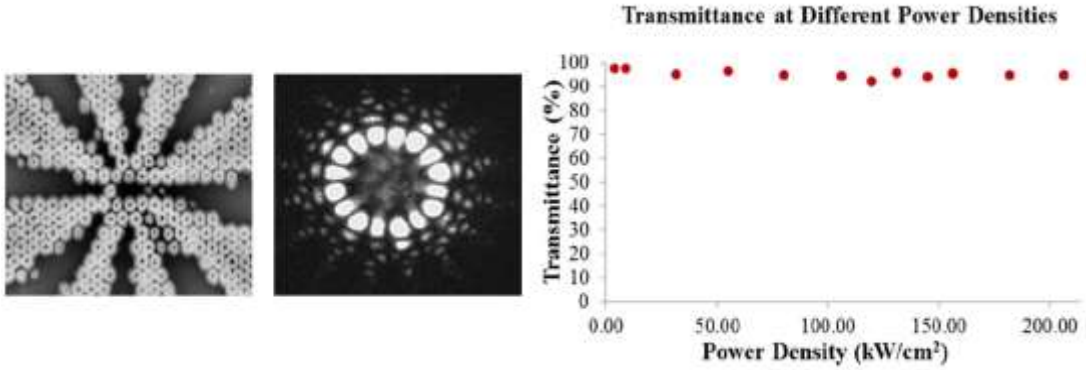


Fig. 10. (Left) An SEM image of the fabricated nanohair structures. (Middle) The transmitted beam profile at 1.55 μm. (Right) Transmission versus incident power density is plotted.

*References*

[1] S. S. Wang and R. Magnusson, "Theory and applications of guided-mode resonance filters," *Appl. Opt.*, 32(14), 1993.

[2] M. G. Moharam and T. K. Gaylord, "Rigorous coupled-wave analysis of planar-grating diffraction," J. Opt. Soc. Am. 71, 811-818 (1981).
[3] A. J. Pung, S. R. Carl, I. R. Srimathi, E. G. Johnson, and S. Member, “Method of Fabrication for Encapsulated Polarizing Resonant Gratings,” *IEEE Photonics Technol. Lett.*, vol. 25, no. 15, pp. 1432–1434, 2013.
[4] J. M. Bendickson, E. N. Glytsis, T. K. Gaylord, and D. L. Brundrett, “Guided-mode resonant subwavelength gratings: effects of finite beams and finite gratings.,” *J. Opt. Soc. Am. A*, vol. 18, no. 8, pp. 1912–28, Aug. 2001.
[5] D. W. Peters, S. A. Kemme, and G. R. Hadley, “Effect of finite grating , waveguide width , and end-facet geometry on resonant subwavelength grating reflectivity,” *J. Opt. Soc. Am. A*, vol. 21, no. 6, pp. 981–987, 2004.
[6] I. A. Avrutsky and V. A. Sychugov, “Reflection of a beam of finite size from a corrugated waveguide,” *J. Mod. Opt.*, vol. 36, no. 11, 1989.
[7] I. R. Srimathi, A. J. Pung, Y. Li, R. C. Rumpf, and E. G. Johnson, "Fabrication of metal-oxide nano-hairs for effective index optical elements," *Opt. Express* 21, 18733-18741 (2013).

*Publication* – A. Pung, I. Raghu Srimathi, Y. Li, E. Johnson, M. D. Shinn, K. J. Lee, R. Magnusson, J. Talghader, L. Taylor, L. Shah, M. Richardson, “High-power laser testing of 3D meta-optics”, Proc. SPIE 8885, Laser-Induced Damage in Optical Materials, 88850K (2013).

## Diffractive Orbital Angular Momentum Demultiplexing Elements for Underwater Optical Communications

The electric field distribution of beams that carry orbital angular momentum (OAM) can be represented as $E \sim \exp(jm\varphi)$, where $\varphi$ is the azimuthal angle distribution and $m$ is the topological charge [1]. The spatial modes are orthogonal to each other, have low inter-modal crosstalk – enabling them to be used in space division multiplexing (SDM) systems to increase the bandwidth of communication links [2]. Fast and efficient solutions are desired for multiplexing and demultiplexing the spatial modes. Many existing techniques for OAM demultiplexing are power inefficient. For instance, sorting N states requires (N-1) beam splitters, each with a 3 dB loss, to be cascaded [2].
To circumvent this problem, coordinate transformations [3] can be utilized by employing two complex phase only elements to demultiplex different OAM states. In the past, systems based on this principle were either implemented with spatial light modulators [3] or by individually diamond machining [4] the elements limiting their effectiveness for practical applications. In this project, diffractive versions of the two phase elements have been implemented on a fused silica substrate that can be used to efficiently demultiplex OAM eigenstates for potential application to an underwater wireless optical communications (UWOC) link operating at $\lambda = 450$ nm [5].

*Log-polar coordinate transformations* – The first phase only element (Fig. 1(a)) performs the geometric log-polar coordinate mapping of the input beam ($u = -a\ln((x^2+y^2)^{1/2}/b)$ and $v = a\arctan(y/x)$, where $a$ scales and $b$ translates the position of the transformed image) by converting a ring profile with azimuthal phase to a rectangle with a linear phase. The second phase element (Fig. 1(b)) placed on the Fourier plane of the first element, corrects for the phase of the transformed beam. Finally, a focusing lens is used to convert the rectangles with linear phase gradients to a spot in the focal plane that shift depending on the incident topological charge. The phase profiles of the two elements are given by –

$$\phi_1(x,y) = \frac{2\pi a}{\lambda f_1}\left[ y\arctan\left(\frac{y}{x}\right) - x\ln\left(\frac{\sqrt{x^2+y^2}}{b}\right) + x - \frac{1}{a}\left\{\frac{1}{2}\left(x^2+y^2\right)\right\}\right] \quad (1)$$

$$\phi_2(u,v) = -\frac{2\pi ab}{\lambda f_2}\exp\left(-\frac{u}{a}\right)\cos\left(\frac{v}{a}\right) - \frac{\pi}{\lambda f_1}\left(u^2+v^2\right) \quad (2)$$

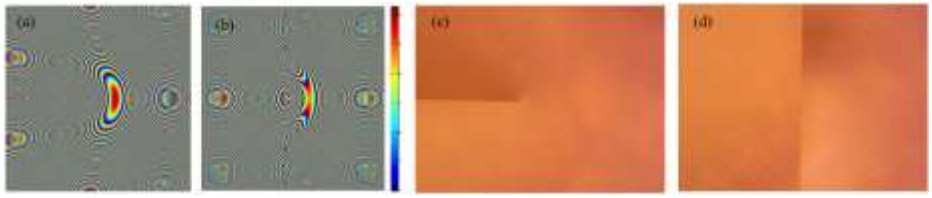

Fig. 1. Simulated mod $2\pi$ phase profiles of (a) first, and (b) second OAM demultiplexing elements. Optical microscope images of fabricated (c) first, and (d) second diffractive phase elements.

The proposed diffractive elements were fabricated on a fused silica substrate using a $2^4$ lithographic process (16 level device with ~98% diffraction efficiency). The size of each of the phase elements was 7 mm X 7 mm and multiple devices can be fabricated on each substrate. The $2\pi$ phase depth for $\lambda$ = 450 nm was calculated to be 967 nm. Optical microscope images of the two fabricated phase elements are shown in Fig. 1(c,d).

*Simulation Results and Experimental Testing* – The first log-polar coordinate transformation element $\Phi_1$ converts the ring shaped beam carrying an azimuthal phase to a rectangular beam with a linear phase gradient at the Fourier plane located $f_1$ = 200 mm away (Fig. 2(a,b)). The second phase correcting element $\Phi_2$ is present at this Fourier plane and a focusing lens ($f_3$ = 75 mm) placed right after $\Phi_2$ sorts the input OAM state, generates a spot and laterally shifts it in the focal plane (Fig. 2(c,d)).

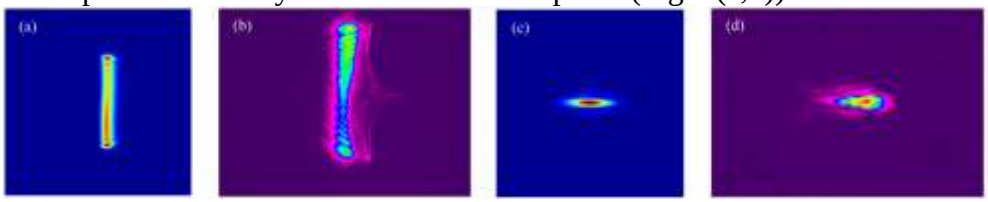


Fig. 2. (a) Numerical simulation, and (b) experimentally obtained intensity profile of the unwrapped OAM +2 beam after the log-polar coordinate transformation, at the plane of the second element ($f_1$ = 200 mm). (c) Numerical simulation, and (d) experimentally obtained spot at the focal plane of the focusing lens placed after the second element ($f_3$ = 75 mm) corresponding to the incident OAM +2 beam.

Lateral spacing between two desired OAM states can be controlled with the focal length of the focusing lens. In the present configuration, two OAM states differing by 2 are separated by 18.75 μm. The fabricated diffractives were used to experimentally demultiplex collinearly propagating OAM beams (Fig. 3(a)). On the first optical table, 450 nm fiber-pigtailed laser diodes were used as the source to generate different OAM states using spiral phase plates. OAM carrying beams were propagated to the demultiplexing end situated about 10 feet away on a second optical table. 7 different beams (OAM 0, OAM ±2, OAM ±4, OAM ±8) were used to analyze the performance of the fabricated elements. Fig. 3(b) shows the theoretical and experimentally obtained peak locations in the focal plane of the 75 mm lens. It is evident from the results that there is very good agreement between theoretical predictions and experimentally observed lateral shifting of the spots in the focal plane. Efficiency of the system was computed by measuring the power incident on the first element $\Phi_1$ and the power in the spots on the final focal plane. Overall efficiency of the system was calculated to be ~80%, including the Fresnel losses present at different interfaces.

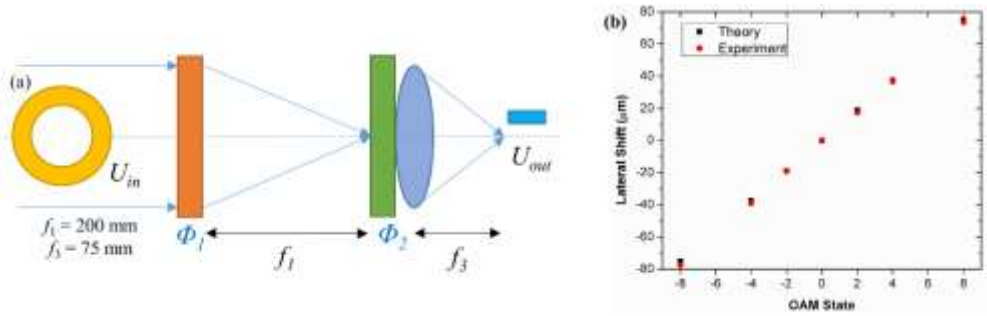


Fig. 3. (a) Experimental setup for demultiplexing collinearly propagating OAM states. (b) Theoretical and experimentally obtained peak locations of the spots on the focal plane of the 75 mm focusing lens vs the incident OAM states.

*Conclusions* – Diffractive optical elements were designed, fabricated and tested to efficiently demultiplex OAM carrying beams at $\lambda$ = 450 nm. Successful demultiplexing of 7 different OAM states has been demonstrated. Overall efficiency of the system was measured to be ~80% enabling the technology to be used in UWOC links employing SDM techniques.

*References*

[1] L. Allen, M. W. Beijersbergen, R. J. C. Spreeuw, and J. P. Woerdman, "Orbital angular momentum of light and the transformation of Laguerre-Gaussian laser modes," Phys. Rev. A **45,** 8185 (1992).

[2] J. Wang, J. Y. Yang, I. F. Fazal, N. Ahmed, Y. Yan, H. Huang, Y. Ren, Y. Yue, S. Dolinar, M. Tur, and A. E. Willner, "Terabit free-space data transmission employing orbital angular momentum multiplexing," Nat. Photonics **6**, 488–496 (2012).

[3] G. C. G. Berkhout, M. P. J. Lavery, J. Courtial, M. W. Beijersbergen, and M. J. Padgett, "Efficient sorting of orbital angular momentum states of light," Phys. Rev. Lett. **105**, 153601 (2010).

[4] M. P. J. Lavery, D. J. Robertson, G. C. G. Berkhout, G. D. Love, M. J. Padgett, and J. Courtial, "Refractive elements for the measurement of the orbital angular momentum of a single photon," Opt. Express **20**, 2110-2115 (2012).

[5] J. Baghdady, K. Miller, K. Morgan, M. Byrd, S. Osler, R. Ragusa, W. Li, B. M. Cochenour, and E. G. Johnson, "Multi-gigabit/s underwater optical communication link using orbital angular momentum multiplexing," Opt. Express **24**, 9794-9805 (2016).

*Publication*

1. I.R. Srimathi, K. Miller, W. Li, K. S. Morgan, J. Baghdady, and E. G. Johnson, "Diffractive Orbital Angular Momentum Demultiplexing Elements for Underwater Optical Communications," in *Frontiers in Optics 2016*, paper FTh4E.2.

## Design, Fabrication and Application of Mid-IR Guided Mode Resonance Filters

Conventional optical elements and Multi-Layer Dielectric (MLD) mirrors have been used for a number of discrete components in laser systems. The power requirements vary from component to component; however, a scalable concept would be optimal for most applications and one that lends itself to high volume manufacturing. Other potential applications reside in the Mid IR wavelengths and beyond, where material systems are somewhat limited and coatings become more of a challenge. In recent years, an alternative to MLD has been proposed and adopted in a number of applications using Guided Mode Resonance (GMR) [1-5]. This approach uses a grating to couple incident light into a leaky waveguide mode that reflects a narrow spectral band of the incident light. A number of devices have been realized based on this concept for applications in beam shaping and fiber lasers [6-8]. Others have introduced designs that operate in the Mid-IR based on Ge for broadband polarization mirrors [5], but challenges still exist in the design and fabrication of these devices due to limited material choices. Moreover, coatings are generally limited in their power handling capability.
In this project, design and fabrication of two devices working at around 2.8 μm are investigated. The first one uses a square lattice and the second one uses a hexagonal lattice as the subwavelength grating. The spectral characteristics of the GMR devices are simulated under plane wave illumination using rigorous coupled-wave analysis (RCWA) to study the response of the devices [9, 10]. The fabrication is performed with projection lithography, dry etching and deposition of Hafnium Oxide for the guiding layer.

*Design and Fabrication of Devices* – Design and fabrication of two devices working at around 2.82 μm are investigated. The first one uses a square lattice in the subwavelength grating region and the second one uses a hexagonal lattice as the subwavelength grating. The spectral characteristics of the GMRF devices were simulated under plane wave illumination using rigorous coupled-wave analysis (RCWA) to study the response of the devices. Fig. 1 shows the two GMRF structures and their spectral characteristics at normal incidence. The simulations included the rounding, or funneling, of the features as a result of the lithography and etching processes.

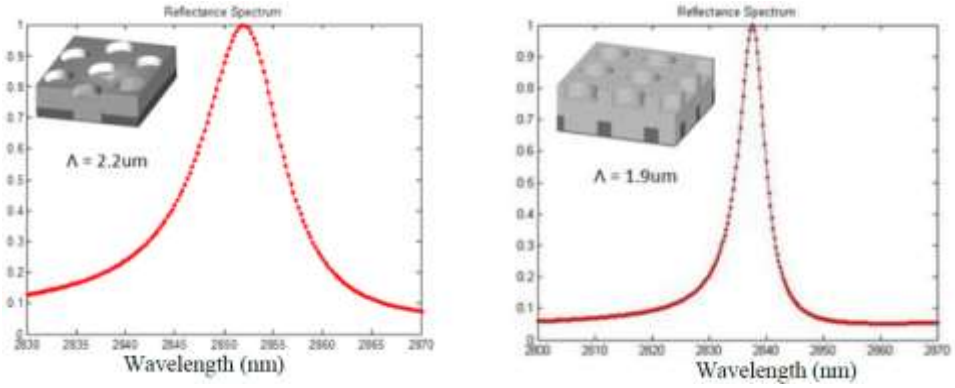


Fig. 1. Modified GMRF profiles and resonance characteristics. (a) Modified square profile, (b) Modified resonance location of square profile, (c) Modified hexagonal profile, and (d) Modified resonance location of hexagonal profile.

The devices were fabricated on 100 mm diameter, double-sided polished, quartz wafers (substrates). The device fabrication was achieved in a three-step process. The first step in the fabrication process was to pattern the subwavelength gratings on the quartz wafer. To carry out the exposures, Shipley 1805 was coated on the wafer to obtain a 380 nm photoresist coating. The spatial period of the subwavelength square grating was 1900 nm and the hole radii were 650 nm and the spatial period of the hexagonal grating was 2200 nm and hole radii were 730 nm. The exposures were carried out using a GCA g-line 5X reduction stepper. The second step in the fabrication process was to transfer the patterns into the quartz substrate. The patterned photoresist was used as a mask to transfer the topography 270 nm into the substrate for both the square and hexagonal lattices. This was accomplished by using a Unaxis Versaline Inductively-Coupled Plasma (ICP) oxide etcher. The third step was to fabricate the waveguide layer which consists of 615 nm of Hafnium-Oxide. This layer was grown using Ion Beam Sputtering (IBS) technique for both the designs. Since the etch depths and the waveguide thicknesses were the same for both the square and the hexagonal designs, it was possible to fabricate both the devices on the same substrate which was easier for uniformity comparisons. To gain understanding of the device structure after the fabrication process, cross-sectional SEM images were taken for the hexagonal lattice. Fig. 2 shows the SEM images of the hexagonal device. The devices were modeled to account for the curvatures arising from the deposition of the waveguide layer during fabrication of devices, see Fig. 1.

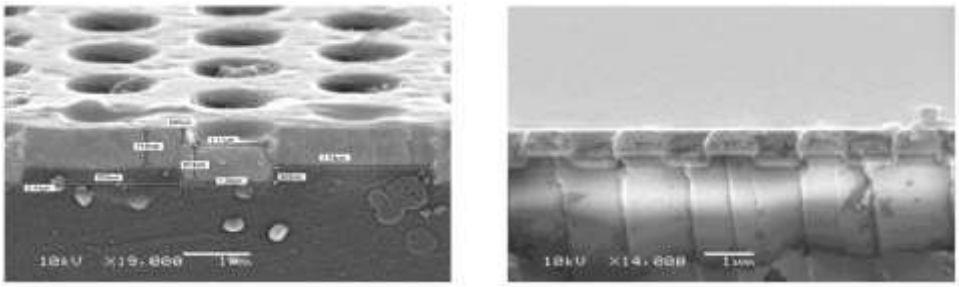

Fig. 2. Cross-sectional SEM images of the hexagonal lattice. (Left) Hexagonal GMRF stack at 15 degrees tilt. (Right) Side view of the device clearly indicating the deposition process.

*Device Testing and Characterization* – For the square lattice, the resonance was located at 2838 nm with a linewidth of 5 nm whereas the hexagonal lattice resonance is at 2852 nm with a linewidth of 10 nm. Since the resonances of both GMRF devices are outside the spectrum of our current laser (maximum wavelength possible was 2814 nm), the GMRF was used at angle in a Mid-IR fiber laser setup. The angular variation of the resonance location has been plotted. The fiber gain media is a 4.2 m long, 6 mol. % Er-doped double-clad fluoride fiber provided by FiberLabs. A fiber-coupled laser diode operating at 975 nm is used a CW pump source. The pump is collimated, redirected and sent into the inner clad of the fiber. The laser cavity is formed between fiber-end facet and an external cavity Littrow grating. By tuning the angle of the grating, the output laser wavelength is also tuneable across a broad range. The output is monitored by a monochromator equipped with a PbSe detector. Then the GMRF is inserted into the output of the Littrow locked laser. By tuning of the angle of the GMRF respect to incident laser beam for maximum reflected power, the angular dependence of wavelength

(angle $\theta$) is determined. Fig. 3 illustrates the optical setup for this characterization and for a modification to the system to use the GMR as a feedback element in the fiber laser itself to verify the linewidth of the GMR.
Fig. 4 illustrates the angular dependence on the resonance. The shift seems to trend with the predictions, but the fabrication and/or material properties may have introduced a shift in the resonance. The spectral width was verified using the fiber laser setup, GMR as the feedback element at an angle.

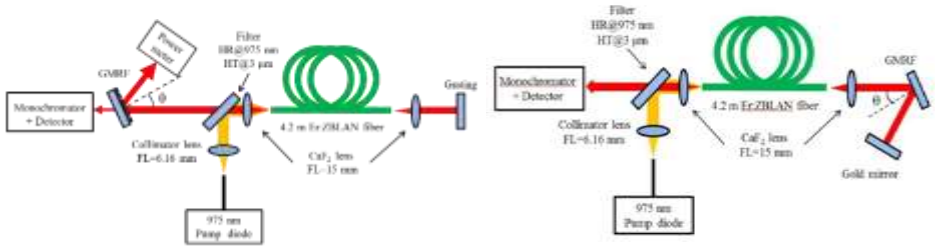


Fig. 3. Fiber laser setup for measuring characteristics of the GMR at Mid-IR wavelengths using a Er-doped ZBLAN fluoride fiber laser (left) angular measurements and (right) direct feedback.

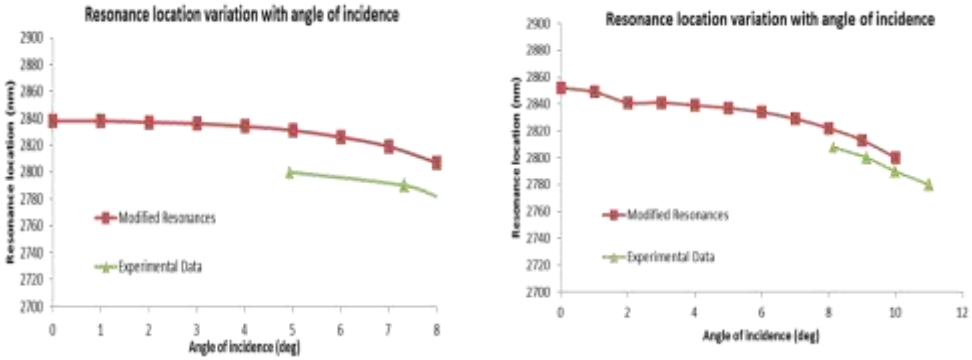


Fig. 4. The resonance location variation with angle of incidence for the GMRF devices. (Left) Square grating GMRF (Right) Hexagonal grating GMRF.

<u>*Conclusions*</u> – Design and fabrication of Mid-IR GMR's have been realized with this effort using Quartz substrates and Hafnia films for the guiding layer. Two designs were investigated: hexagonal array and a rectangular array. Both design types have similar performance and exhibit polarization splitting off normal incidence. The angular dependence of both designs correlated well with those predictions from RCWA. The peak location was slightly different, but that is likely due to tolerances in the fabrication process. Moreover, the devices were also able to externally line narrow the ZBLAN fiber laser, which shows it to be a viable approach for external wavelength control of Mid-IR fiber lasers.

One of the applications of GMRFs is as a spectrally selective feedback mirror in external fiber laser configuration. For the 2.8 μm fiber laser system, a two-layer GMRF was designed to act as the HR. It simply consists of a hexagonal lattice SWG formed into the low index quartz substrate ($n_{sub}$ = 1.4239). A 541 nm thick high-index $HfO_2$ layer was deposited over the SWG to act as the waveguide region ($n_{guide}$ = 1.9695). Using the present choice of the materials, the refractive index contrast between the materials is

fairly low. This results in a narrow linewidth GMRF device of only a few nm's width. The spatial period of the sub-wavelength hexagonal grating was 2200 nm and the duty cycle of the grating was 66%, which results in a theoretical resonance wavelength of 2782 nm with a FWHM of 6.8 nm, as shown in Fig.1. The gain spectrum of the Er:ZBLAN fiber is widely distributed within 2.65-2.85 µm. The resonance wavelength of the device was designed such that it is near the maximum gain region around 2.79 µm. The simulated device performance and characteristics were obtained using the Rigorous Coupled Wave Analysis (RCWA), under plane wave illumination conditions.

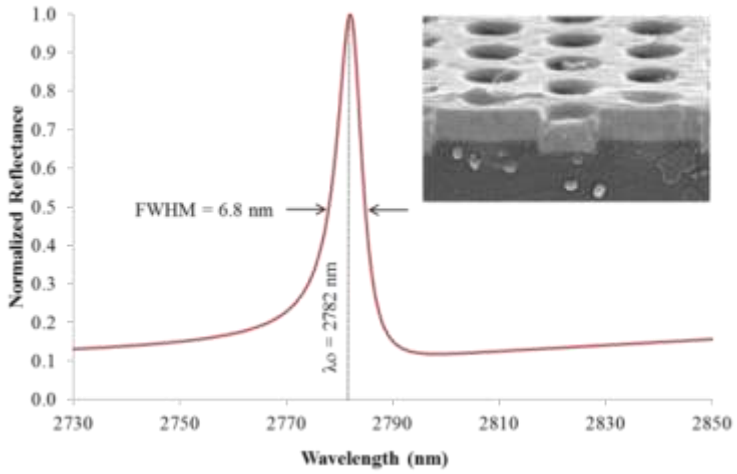


Fig.1. Simulated resonance spectrum of the GMRF. (Inset) SEM micrograph of the fabricated device.

The fiber laser setup is shown in Fig.2. The 4.2 m, 6 mol % Er-doped double-clad ZBLAN fluoride fiber has a core diameter of 15 µm and a 0.12 NA surrounded by a D-shaped inner cladding with a 350 µm diameter and 0.50 NA. The cladding absorption for the 975 nm pump light was measured to be ~3.9 dB/m using the cut-back method. A fiber-coupled laser diode operating at 974 nm with a maximum output power of 50 W was used as the CW pump source. The output fiber of the laser diode has a core diameter of 200 µm and a 0.22 NA. The pump was collimated by an aspheric lens with a focal length of 6.16 mm. An optical edge filter at 45 degrees angle of incidence (AOI) was used to re-direct to pump without affecting the output laser. The filter has a reflectivity of 88% for 974 nm pump and ~95% transmission for 2.8 µm laser wavelength at 45 Deg. AOI. The pump beam was launched into the inner cladding of the fiber using a $CaF_2$ lens with a focal length of 15 mm, with a total coupling efficiency of 66%. The fiber was manually cut at both ends, and the fiber cavity is formed between one fiber-end facet and the external cavity HR device (GMRF or gold mirror). The wavelength of the output laser was measured by a monochromator equipped with a PbSe/PbS detector.

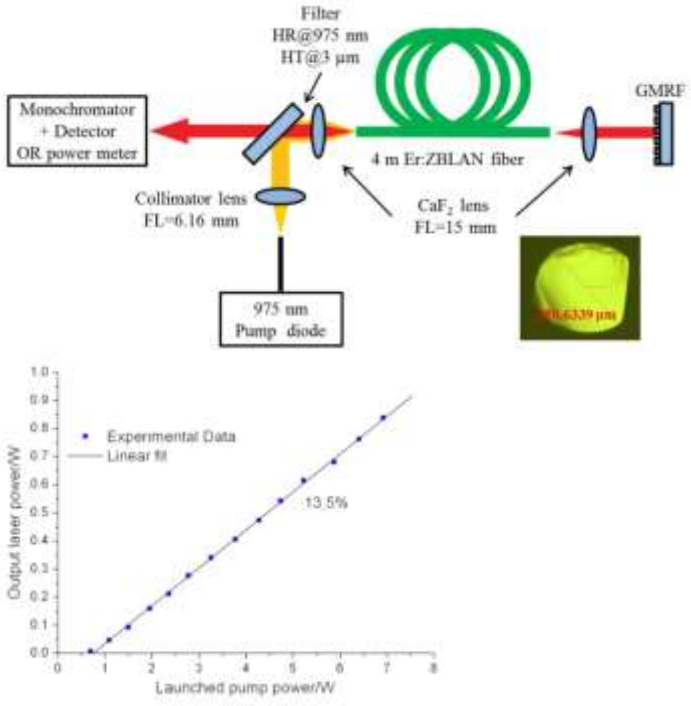


Fig.2. Left, Fiber laser setup with GMRF as external HR. Right, measured laser power.

The maximum output power was 1 W with a slope efficiency of 13.5%. Due to the high wavelength selectivity of the GMRF, when used as the HR, the lasing emission is limited within a narrow linewidth with a well-defined, lasing line less than 2 nm. Fig. 3 shows the laser spectrum taken under two different pump power levels using GMRF mirror as HRs. Compared to the free-running laser spectrum using a gold mirror as the external HR shown in fig.3, it is clear that GMRF selects and maintains a specific lasing wavelength that does not red-shift with increasing pump power.

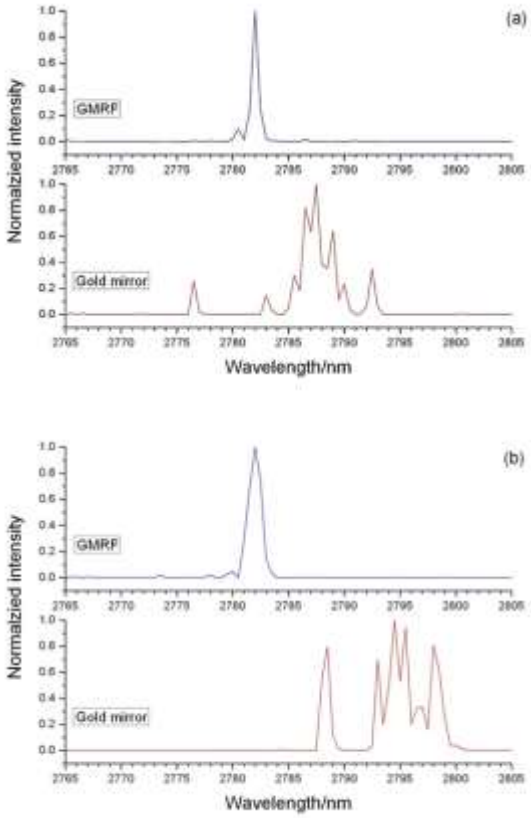


Fig. 3. Comparison of laser spectrum using GMRF and gold mirror as HR, under same launched pump power, (a), pump power is 2.34 W; (b), pump power is 7.05 W.

Another application of GMRF in fiber laser is utilizing the polarization selectivity at angular incidence.

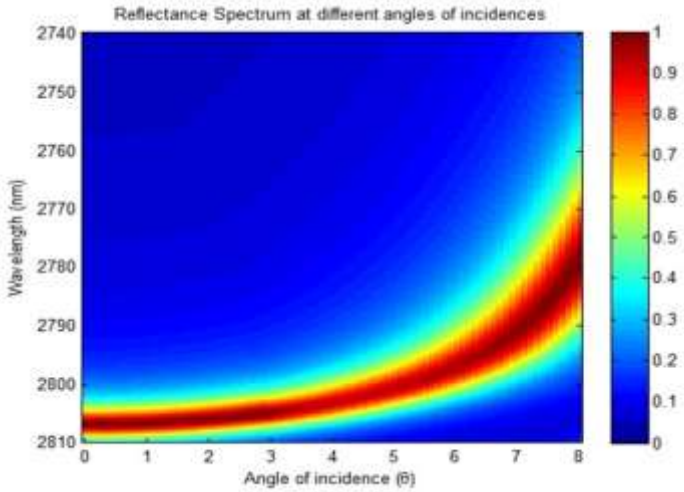


Fig. 4. Angular dependence of the GMRF.

The fiber laser setup is shown in Fig. 5(a). The GMRF is placed at an angle relative to the fiber tip along with a gold mirror that forms an external HR which serves as wavelength selective feedback element. The output laser spectrum with the GMRF at varying θ is shown in fig. 5(b).

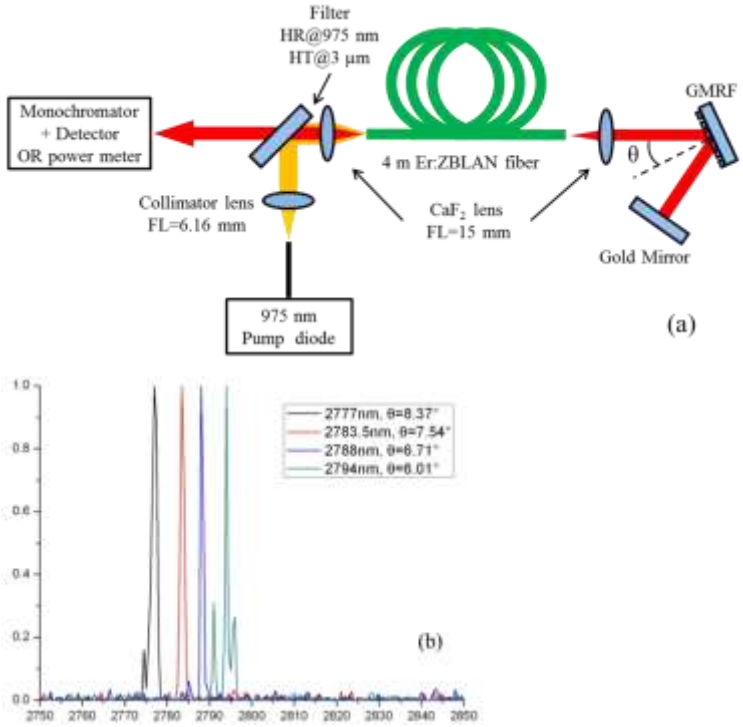


Fig.5. (a) Experimental setup; (b) laser spectrum with GMRF placed at different angle.

GMRFs with a resonance wavelength in the mid-IR regime was designed, fabricated, and utilized in a Er:ZBLAN fiber laser as an external HR. While the correlation between the GMRF simulation and experiment is good, fabrication and alignments can shift the resonance from the desired location. Polarization can also be exploited in GMRFs as shown in the GMRF for 2 μm Tm:fiber laser, as well as single and multiple resonance lines.

*References*


[1] S. S. Wang and R. Magnusson, "Theory and applications of guided-mode resonance filters," Appl. Opt. 32, 2606-2613 (1993).

[2] S. Peng and G. M. Morris, "Experimental demonstration of resonant anomalies in diffraction from two-dimensional gratings," Opt. Lett. **21**, 549-551 (1996).

[3] D. Rosenblatt, A. Sharon, and A. A. Friesem, "Resonant grating waveguide structure," IEEE J. Quantum Electron. **33**, 2038-2059 (1997).

[4] Z. S. Liu, S. Tibuleac, D. Shin, P. P. Young, and R. Magnusson, "High-efficiency guided-mode resonance filter," Opt. Lett. **23**, 1556-1558 (1998).

[5] Juha M. Kontio, Janne Simonen, Kari Leinonen, Markku Kuittinen, and Tapio Niemi, "Broadband infrared mirror using guided-mode resonance in a subwavelength germanium grating", Optics Letters, Vo. 35, No. 15, 2564-2566 (2010).

[6] A. Mehta, R. C. Rumpf, Z. A. Roth, and E. G. Johnson, "Erbium-Ytterbium Doped Double Cladding Optical Fiber Laser Utilizing a Guided Mode Resonance Filter as an External Feedback Element", IEEE Photonics Tech. Letters, v. 19, 24, pp. 2030-2032 (2007).
[7] Sims, R Andrew; Roth, Zachary A; Willis, Christina C C; Kadwani, Pankaj; McComb, Timothy S; Shah, Lawrence; Sudesh, Vikas; Poutous, Menelaos; Johnson, Eric G; Richardson, Martin, "Spectral narrowing and stabilization of thulium fiber lasers using guided-mode resonance filters," Optics Letters, Vol. 36 Issue 5, pp.737-739 (2011).
[8] P. Srinivasan, M. K. Poutous, Z. A. Roth, Y. O. Yilmaz, R. C. Rumpf, and E. G. Johnson, "Spatial and Spectral Beam Shaping with Space Variant Guided Mode Resonance Filters", Opt. Exp. 17, 22, 20365-20375 (2009).
[9] M. G. Moharam, and T. K. Gaylord, "Rigorous coupled-wave analysis of planar-grating diffraction," J. Opt. Soc. Am., 71(7), 811-818 (1981).
[10] R. Rumpf and E. G. Johnson, "Modeling fabrication to accurately place GMR resonances," Optics Express, Vol. 15, No. 6, pp. 3452-3464, March 19 (2007).

*Publication* –

1. E. G. Johnson, R. Woodward, M. Poutous, A. Pung, Y. Li, and I. Raghu, "Design and Fabrication of Mid-IR Guided Mode Resonance Filters," in *Integrated Photonics Research, Silicon and Nanophotonics*, OSA Technical Digest (online) (Optical Society of America, 2012), paper ITu3B.2.
2. Li, Yuan, Indumathi Raghu Srimathi, Ryan H. Woodward, Aaron J. Pung, Menelaos K. Poutous, Ramesh K. Shori, and Eric G. Johnson. "Guided-mode resonance filters for wavelength selection in mid-infrared fiber lasers."*IEEE Photonics Technology Letters* 24, no. 24 (2012): 2300-2302.
3. Li, Yuan, Ryan H. Woodward, Indumathi Raghu Srimathi, Aaron J. Pung, Menelaos K. Poutous, Eric G. Johnson, and K. Ramesh. "2.78 μm fluoride glass fiber laser using guided mode resonance filter as external cavity mirror." In *IEEE Photonics Conference 2012*, pp. 826-827. IEEE, 2012.
4. Johnson, Eric G., Yuan Li, Ryan Woodward, Menelaos Poutous, Indumathi Raghu, and Ramesh Shori. "Guided mode resonance filter as wavelength selecting element in Er: ZBLAN fiber laser." In *Specialty Optical Fibers*, pp. STu3F-1. Optical Society of America, 2012.
5. Johnson, Eric G., Yuan Li, Indumathi Raghu Srimathi, Ryan H. Woodward, Menelaos K. Poutous, Aaron J. Pung, Martin Richardson, Lawrence Shah, Ramesh Shori, and Robert Magnusson. "Resonant optical devices for IR lasers." In *SPIE LASE*, pp. 85991G-85991G. International Society for Optics and Photonics, 2013.

## MetaOptic Beam-shaping and amplification with Ho:YAG rod amplifier

As a super-position of vortex beams, concentric vortex beams are interesting mainly due to the propagation properties and their application in communication systems. The amplification of concentric vortex beams has been demonstrated for the first time in a rod amplifier. A rod amplifier is a frontier approach in solid state systems combing the advantages of the conventional bulk crystal materials and optical fiber systems. Typically the seed goes through the rod as in free space while the pump is wave-guided by the rod. However, the design can be rather flexible depending on the applications, such as to increase the modal overlap between the seed and the pump and therefore increasing the gain performance.

Figure 1(a) shows the single-pass, co-pumping amplifier setup utilizing the 1% Ho:YAG rod. The ends of the 1mm diameter × 60 mm long Ho:YAG rod were polished to flat/flat finish and AR coated for both the pump and the seed wavelengths (1.9 – 2.1 μm). A 1908 nm single mode Tm:fiber laser (IPG TLR-50) was used as the pump source operating in a modulated mode reduce the thermal load in the crystal rod. The output of a CW tunable laser (IPG HPTLM Cr:ZnS/Se) at 2091 nm was coupled into a 10/125 polarization-maintaining (PM) fiber and used as the seed delivery fiber to ensure high mode quality. Without the concentric phase plate, the focused single-mode seed beam diameter was approximately 200 μm at the focal point located at the center of the rod. D1 and D2 are identical dichroic filters oriented at a 45 degree angle of incidence (AOI) with high transmission at the pump wavelength and high reflection at the seed wavelength. The images of the amplified vortex beam are captured using an IR camera (Ophir Pyrocam IV).

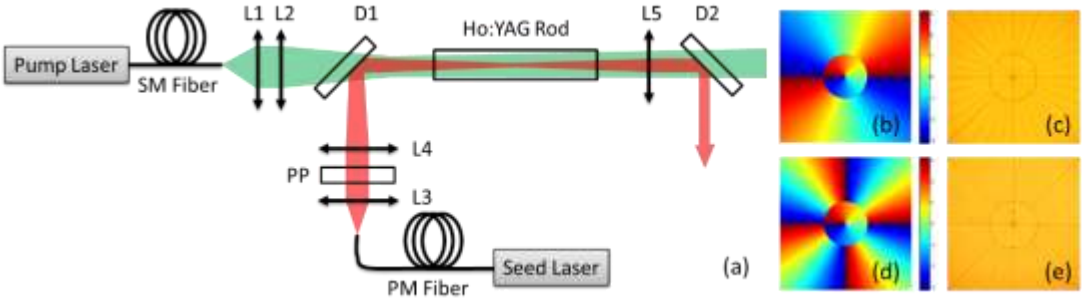


Fig. 1. (a) Experimental setup of the Ho:YAG rod amplifier. (b) The simulated phase wrap; (c) the microscope image of the fabricated phase plate for the 3-lobe concentric vortex. (d) The simulated phase wrap; (e) the microscope image of the fabricated phase plate for the 5-lobe concentric vortex.

The phase plate converts the Gaussian seed beam into the desired concentric vortex beam shape. The phase plate can be designed for any wavelength. In the current effort, the phase plate was designed to operate at 2091 nm. The concentric vortex phase plate consists of an inner vortex with a counter-clockwise phase wrap of ($n\times 2\pi$) and an outer vortex with a clockwise phase wrap of ($-m\times 2\pi$). By choosing the proper Gaussian beam size so as to cover both the inner and outer parts of the phase plate, the far field pattern of the beam will contain several spatially separated lobes due to interference of the wavefronts from the inner and outer vortices, and the number of the lobes is determined by the total charge number (n+m). . In this work, the (1+2) and (1+4) concentric vortices,

corresponding to 3-lobe and 5-lobe vortices, were investigated. Illustrations of the phase wrap and the microscope images of the fabricated phase plates are shown in Figs. 1(b)-1(e). The phase plates were fabricated on a fused silica wafer. The fused silica wafer was cleaned, coated with photoresist and patterned using optical lithography. Then the wafer was developed and the patterns were transferred from the photoresist to the silica wafer by etching method. The refractive index of the fused silica wafer is 1.436 at 2091 nm, so the total etching depth into the wafer corresponds to 4531 nm for a $2\pi$ phase (with 1% etching depth error). Each $2\pi$ phase wrap was approximated by 16 different etching depths into the wafer, which corresponding to a calculated 98.7% diffraction efficiency. The simulated and actual images of the concentric vortex are shown in Fig. 2.

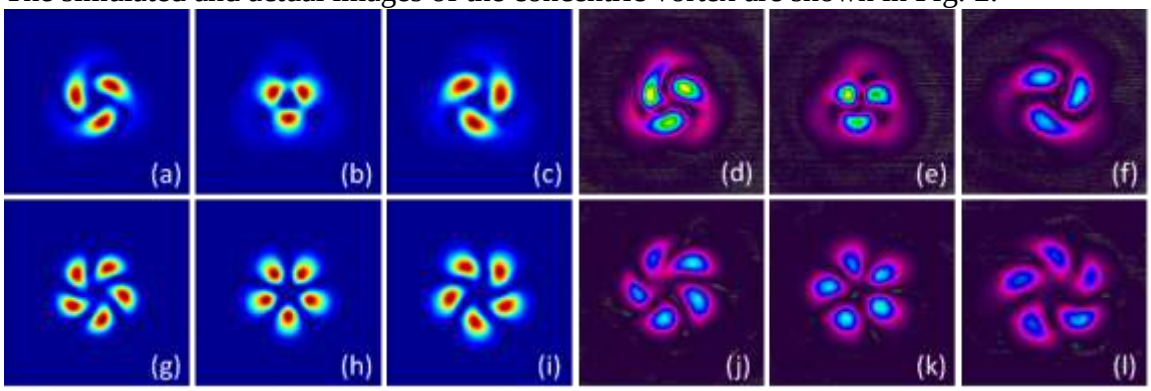


Fig. 2. Upper row, the 3-lobe concentric vortex beam. (a)-(c), the simulated beam at the entrance facet of the rod, at the focal point inside the rod and at the exit facet of the rod. (d)-(f) the images of the beam taken by the IR camera at the corresponding locations. Lower row, the 5-lobe concentric vortex beam. (g)-(i), the simulated beam at the entrance facet of the rod, at the focal point inside the rod and at the exit facet of the rod. (j)-(l), the images of the beam taken by the IR camera at the corresponding locations.

Figures 5(a) and 5(b) shows the output seed power versus the incident pump power for 0.1 W incident seed power and 0.5 W incident seed power, respectively. With 0.1 W of seed power and 20 W incident pump power, the output power for 3-lobe vortex and 5-lobe vortex was 0.88 W and 0.49 W, respectively. The corresponding single-pass gain is 8.8 and 4.9. With 0.5 W of seed power and 20 W incident pump power, the output power for 3-lobe vortex and 5-lobe vortex was 2.40 W and 1.83 W, respectively. The corresponding single-pass gain is 4.8 and 3.7. In both cases, the single-pass gain for the 3-lobe vortex beam was higher than the gain for the 5-lobe vortex. The simple explanation for this could be the pump/signal modal overlap.

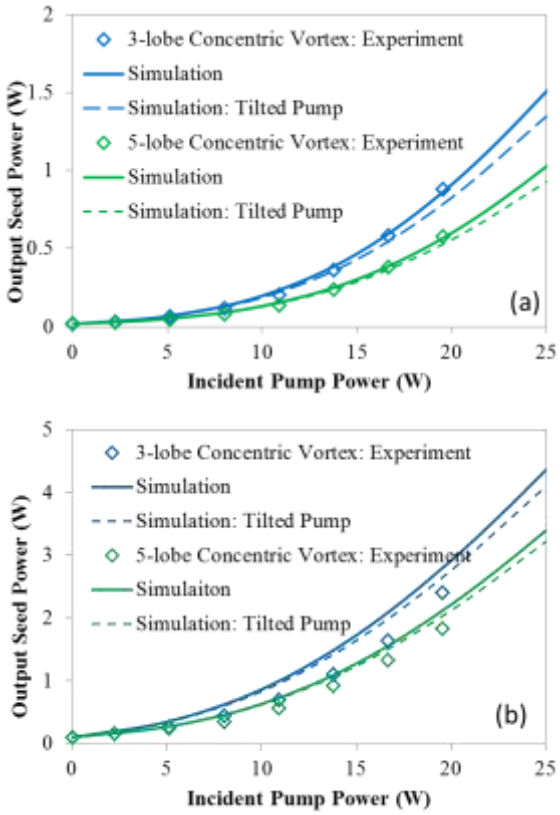


Fig. 3. The measured output seed power for different concentric vortex beams. (a) Incident seed power of 0.1 W; (b) incident seed power of 0.5 W. Blue for 3-lobe concentric vortex and green for 5-lobe concentric vortex.

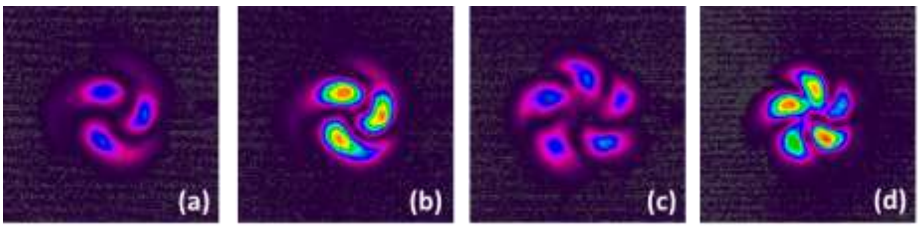


Fig. 4. The images of the concentric vortex beam through the rod amplifier; (a) and (c), with no pump; (b) and (d) with 20 W of incident pump power.

The images of the output seed through the rod without the pump were also taken, shown in Figs. 4(a) and 4(c). The beam is exactly the same compared with images in free space (shown in Figs. 3(f) and 3(l)), supporting the premise that spatial characteristics of vortex beam are preserved propagating through the rod. Comparing the output seed images in Fig. 4 with and without pump power, the seed beam quality maintains well at a high pump power level in both cases, except for some slight distortions in the 5-lobe vortex case. Such distortions mainly arise from input seed asymmetry and pump alignment. The input 5-lobe seed itself shows slight asymmetry and such asymmetry gets intensified with pumping. Also, the pump beam is Gaussian and it is not truly uniformly distributed across the cross-section of the rod, any slight misalignments, including tilt and off-axis incidence, will result in unevenly amplification among the lobes.

Publication

1. Li, Yuan, Wenzhe Li, Zeyu Zhang, Keith Miller, Ramesh Shori, and Eric G. Johnson. "Concentric vortex beam amplification: experiment and simulation."*Optics express* 24, no. 2 (2016): 1658-1667.

## Meta-Optics for multi spectral band optical vortices

A 2090 nm concentric vortex phase plate with topological charge numbers of m = 1, -2 has been designed and fabricated. The phase equation of the phase plate is given by

$$\varphi(r,\theta)=\begin{cases}\exp(jm_{in}\,\theta), & r \le r_{in}\\ \exp(jm_{out}\,\theta), & r \ge r_{in}\end{cases} \quad (1)$$

where $r$ is the radius on the phase plate, $\theta$ is the azimuthal angle, j is the imaginary number, $m_{in}$ is the charge number of the inner vortex phase plate, $m_{out}$ is the charge number of the outer vortex phase plate, and $r_{in}$ is radius of the inner vortex phase plate. In our design, $m_{in}$ = 1, $m_{out}$ = -2, and $r_{in}$= 0.625 mm. One interesting thing to note is that 2090 nm is approximately twice the wavelength of 1064 nm. If the 1064 nm laser goes through the same concentric vortex phase plate, the beam sees 8 phase levels within a 2π wrap instead of 16 levels in the 2090 nm case, and for 1064 nm the same concentric vortex phase plate charge numbers will be m = 2, -4 instead of m = 1, -2.

The experimental setup is shown in Fig. 2. The 2090 nm and 1064 nm lasers were multiplexed to go through a single concentric vortex phase plate with charge numbers of m = 1, -2 for 2090 nm and m = 2, -4 for 1064 nm.

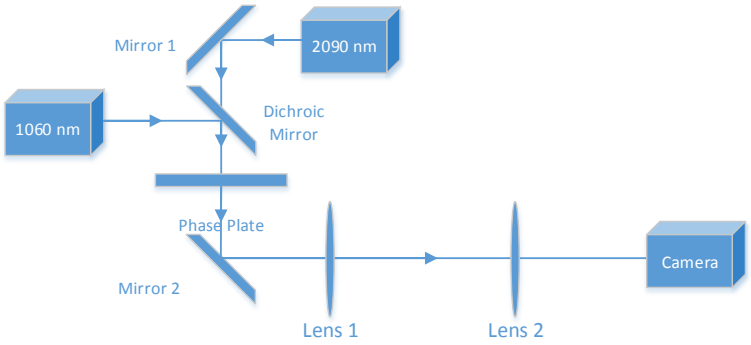


Fig. 2. Experiment setup to multiplex the 2090 nm and 1064 nm lasers through a single concentric phase plate.

The inner and outer vortices have diameters of 1.25 mm and 5 mm, respectively. Lens 1 is a Fourier lens which is used for the convenience of the observation of Fraunhofer diffraction patterns, and Lens 2 is an imaging lens to help image the diffraction patterns after Lens 1 on the IR camera. By moving the imaging lens, the diffracted patterns at different location after the Fourier lens along the propagation direction has been collected on the IR camera.

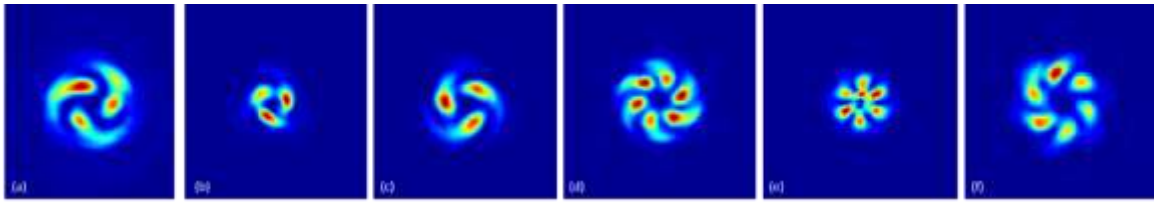

Fig. 2. Experimental images after the Fourier lens for the 2090 nm 3 petal patterns at (a) 156.6 mm, (b) 208.9 mm, (c) 259 mm; and for the 1064 nm 6 petal pattern at (d) 156.6 mm, (e) 208.9 mm, and (f) 259 mm.

The focal length of the Fourier lens is 200 mm. The images of the diffracted patterns located at 156.6 mm, 208.9 mm, and 259 mm after the Fourier lens have been captured by an IR camera. The experimental images are shown in Fig. 2. The results show that the diffraction patterns rotate $2\pi/N$ azimuthally while propagating away from the Fourier lens, where N as the number of petals. The images at 208.9 mm after the Fourier lens are approximately at the back Fourier plane. As one can tell from Fig. 2 (b) and (e), the tails of the petals have disappeared at this point.
Examples of measurement and simulation are shown in the Fig. 3.

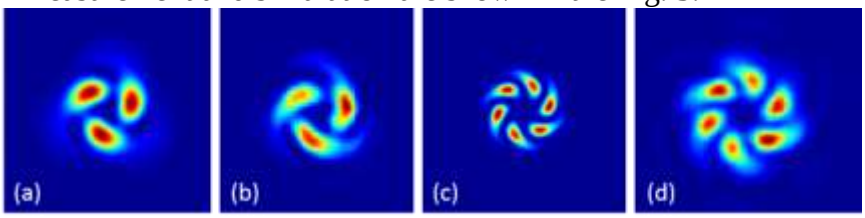


Fig. 3. Petal like diffraction patterns for 2090 nm (a) simulation, (b) experiment; and for 1064 nm (c) simulation, (d) experiment.

Publication

1. Wenzhe Li; Yuan Li; Keith Miller; Eric G. Johnson, "Multiple Wavelength Concentric Vortex Optics: $\lambda$ = 1064 nm and 2090 nm," in Frontiers in Optics 2016, OSA Technical Digest, paper FF5G.5.

**Periodic photonic guided-mode resonance filters**

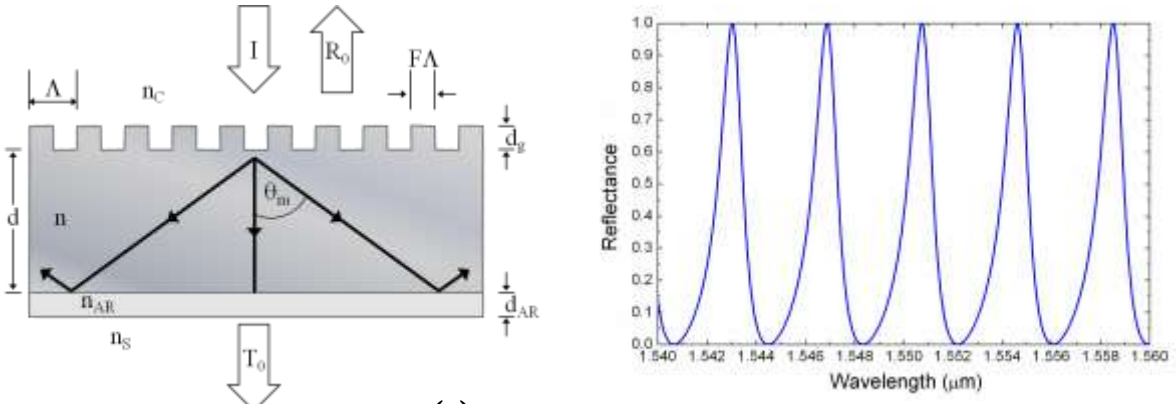


**(a)** **(b)**

**Fig. 1. (a)** Model of a multiline GMR filter denoting thicknesses (d) of the layers and refractive indices (n) of the various regions as well as the period (Λ) and fill factor (F) of the grating. In particular, we consider a thick dielectric slab with a periodic boundary illuminated at normal incidence as shown. The period is sufficiently small such that only the zero-order transmitted ($T_o$) and reflected ($R_o$) waves propagate. An antireflection (AR) layer is placed on the bottom surface. **(b)** Calculated spectral response of an example designed GMR filter for TE-polarized incident light. Parameters: $d_g$ = 500 nm, d = 100 μm, $d_{AR}$ = 245 nm and $n_{AR}$ = 1.581, n = 2.5, $n_c$ = 1.00, $n_s$ = 1.00; grating period Λ = 1050 nm; fill factor F = 0.5.

We (UTA) invented multiline guided-mode resonance filters designed with extremely thick dielectric films. The filter spectral lines appear approximately periodic. We realize these devices as dielectric membranes in air with a subwavelength grating inscribed into one surface. As the film is very thick on the scale of the wavelength, it supports a large number of resonant modes. In general, the resonant modes yield a dense reflectance spectrum with irregular appearance. We show that by placing an antireflection layer on the backside of the slab, the interference between the directly transmitted zero order and the diffracted order generating the waveguide modes is eliminated. Thus, a well-shaped unperturbed comb-like spectrum is realized. For example, a titanium dioxide membrane that is 500 μm thick generates a spectrum with more than 1000 channels separated by ~0.8 nm near the 1.55 μm wavelength.

Figure 1(a) shows the model under study. The device is a thick dielectric slab possessing a shallow periodic surface. We limit the study to normal incidence and transverse-electric (TE) polarization. TE-polarized input light has an electric field vector normal to the plane of incidence. We set the refractive index of the film to n = 2.5 corresponding to titanium dioxide in this example. Figure 1(b) shows the zero-order reflectance $R_o$ of a 100-μm-thick dielectric membrane in air in the C-band of the telecommunications spectrum. In general, for such structures, multiple high-efficiency reflectance peaks appear in the spectrum having irregular shapes. Placing a quarter-wave antireflection (AR) layer centered at λ = 1.55 μm on the device as shown in Fig. 1 eliminates interference from the directly-transmitted wave and renders a well-shaped

reflectance spectrum; this is shown shown in Fig. 1(b). The full-width at half-maximum (FWHM) of each resonance peak is ~1 nm. For the parameters in Fig. 1(b), the first-order diffraction angle $\theta_{\square}$ is such that total internal reflection (TIR) occurs. These computations are performed using rigorous coupled-wave analysis (RCWA).

This theory has been verified with multiple prototype devices fabricated and tested. Figures 2 and 3 show the simulated and measured spectra for surface gratings made with Si and $TiO_2$, respectively. Both devices employ thick Si wafer slabs and operate across wide spectral bands; we focus on the 1545-1555 nm wavelength range in our investigation. For the Si-grating devices, the experimental parameters are approximately $\Lambda$ = 798 nm, F = 0.17, $d_g$ = 193 nm, $n_{AR}$ = 1.93 and $d_{AR}$ = 203 nm; For the $TiO_2$ grating devices, the experimental parameters are approximately $\Lambda$ = 800 nm, F = 0.36, $d_g$ = 209 nm, $n_{AR}$ = 1.9 and $d_{AR}$ = 205 nm. The figures show that the experimental spectra for both device types are in good agreement with the numerical spectra in the resonance locations and spectral shape. Reasonable peak efficiency and sideband levels are achieved for both devices. The $TiO_2$ devices with lower grating modulation strength $\Delta\varepsilon=n_g^2-n_c^2$ exhibit smaller spectral linewidths as expected. The spectral width of each filter peak is ~0.1 nm with free spectral range of ~0.8 nm. Also flatter sidebands are achieved for $TiO_2$ grating devices.

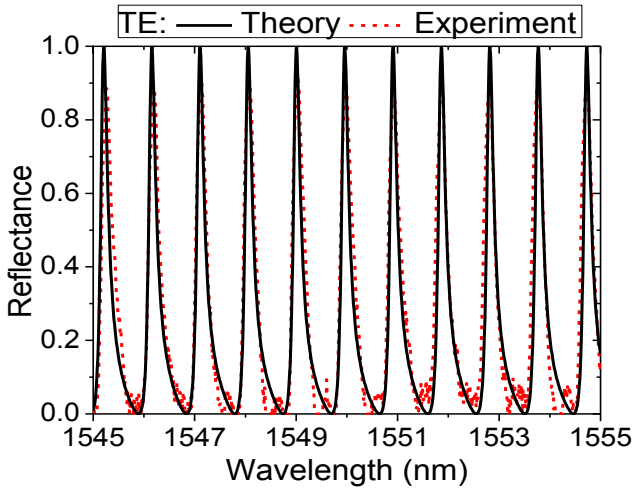


**Fig. 2.** Measured vs. simulated reflectance spectra of GMR devices with Si waveguide and Si gratings. Measured parameters are $\Lambda$ = 798 nm, F = 0.17, $d_g$ = 193 nm, d=300 □m, $n_{AR}$ = 1.93, and $d_{AR}$ = 203 nm with corresponding design parameters as $\Lambda$ = 800 nm, F = 0.16, $d_g$ = 190 nm, d=300 □m, $n_{AR}$ = 1.865, and $d_{AR}$ = 208 nm.

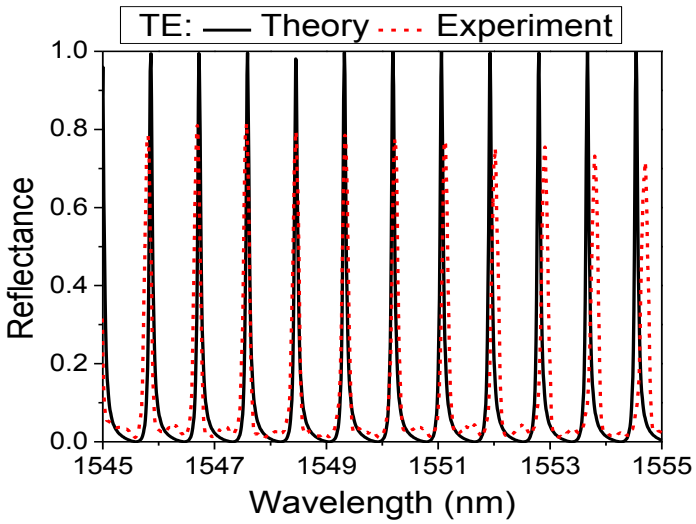


**Fig. 3.** Measured vs. simulated reflectance spectra of GMR devices with Si waveguide and $TiO_2$ gratings. Measured parameters are $\Lambda$ = 800 nm, F = 0.36, $d_g$ = 209 nm, d=300 □m, $n_{AR}$ = 1.9, and $d_{AR}$ = 205 nm. The design parameters are $\Lambda$ = 800 nm, F = 0.32, $d_g$ = 204 nm, d=300 □m, $n_{AR}$ = 1.865, and $d_{AR}$ = 208 nm.

**Experimental demonstration of a mode-competing multiline resonant laser**

We applied the multiline guided-mode resonance (GMR) filter as a reflector to implement an external cavity laser. We design the resonant element using rigorous numerical methods and fashion an experimental prototype by thin-film deposition, patterning, and etching. A ~100-nm $TiO_2$ grating layer on a ~170-μm-thick glass slab supports thousands of resonant modes. We detect ~10 narrow resonance peaks within a ~10-nm wavelength range centered at the 840-nm wavelength. We apply this multiline GMR device to a gain chip and obtain several simultaneous resonant laser lines that compete for the gain. Precise tuning enables a stable laser line that can be selected from the multiple available resonant lines.

The gain chip is an electrically pumped laser diode with a GaAlAs/GaAs quantum well (QW) and a thin waveguide layer that possesses a gain bandwidth range spanning 820-850 nm. The gain chip is electrically pumped with a precision current source and its temperature is kept constant with a temperature controller. Fig. 4(a) shows the laser measurement setup. A near-infrared spectrometer operating at a resolution of 0.1 nm is used to gather the spectral data of the output signal. Figure 4(b) shows the measured gain spectrum with (blue) and without (red) GMR device feedback. The transmission spectrum shows comb-like multi-resonance peaks within the gain chip's emission bandwidth spanning 830-850 nm. The experimental spectra show reasonable agreement with the simulated spectra in the number of resonance peaks per spectral interval.

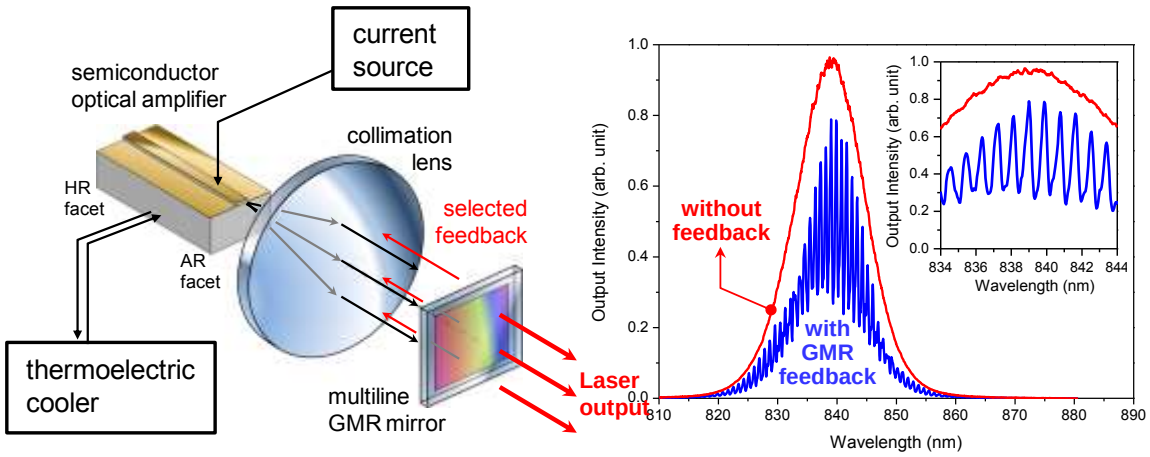


**(a)** **(b)**

**Fig. 4 (a)** Wavelength-selective external cavity laser output measurement setup. **(b)** Measured gain spectrum with (blue) and without (red) GMR device feedback. Device parameters are $\Lambda$ = 700 nm, F = 0.39, and $d_g$ = 107 nm. The injection current is ~40 mA for this measurement.

Figure 5 shows the measured stable laser lines and corresponding lasing characteristics at different mode wavelengths. Within the 835- to 845-nm wavelength range, the thick GMR devices have ~10 resonance peaks and every peak can generate a laser line. We select three typical peaks (left, middle, and right) to illustrate the lasing mode wavelength selectivity and its associated properties. Fig. 5(a) shows the selected stable laser lines at 836.6 nm, 840.5 nm, and 843.7 nm where the linewidth is $\Delta\lambda$ (FWHM) < 0.5 nm. This spectral width is defined by the linewidth of the GMR mirror. Figure 5(b) compares the emitted peak power to the injection current for the corresponding laser lines in Fig. 5(a). These three curves show typical nonlinear lasing characteristics with a threshold current of ~65 mA

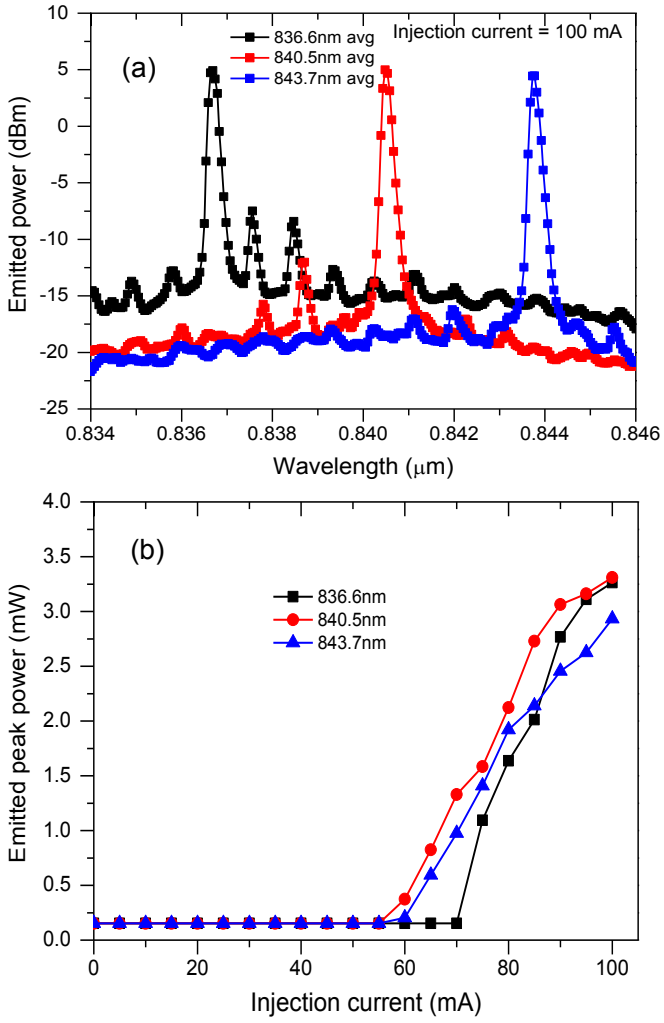


**Fig. 5.** Measured selected stable laser lines and their lasing characteristics. Lasing wavelengths are 836.6 nm (black), 840.5 nm (red), and 843.7 nm (blue). **(a)** Three typical lines with different wavelengths measured at a 100-mA injection current. **(b)** Corresponding lasing characteristics.

## The Rayleigh reflector filter concept

Among goals of the project is development of resonant high-energy laser mirrors and other related optical components. On testing of such mirrors at oblique angles, dangerous levels of radiation can emanate out of the substrate; thus optical engineers must be well aware of this effect. Simulations conducted to evaluate this effect showed extraordinarily rapid transitions of power between the reflected wave and substrate wave near the Rayleigh angle. The Rayleigh anomaly is most famous for deteriorating optical spectra in spectroscopic applications; never have there been any real uses found for it. Here we show a new optical filter concept enabled by the Rayleigh anomaly.

We designed, fabricated, and tested resonant devices that we call Rayleigh reflectors; these devices connect the fundamental concepts of guided-mode resonance (GMR) and the Rayleigh anomaly with interesting possible applications including new filters and couplers. We provide experimental evidence of the rapid exchange of

diffracted power between the reflected zero-order wave and a substrate wave across a small angular range, enabling this new class of resonant devices in any spectral region. Here, we present initial experimental results and compare them with theory.

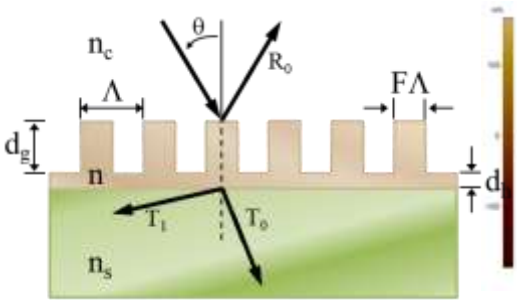


**Fig. 6.** Rayleigh reflector model denoting thicknesses (d) of the layers and refractive indices (n) of the various regions as well as the period (Λ) and fill factor (F) of the grating.

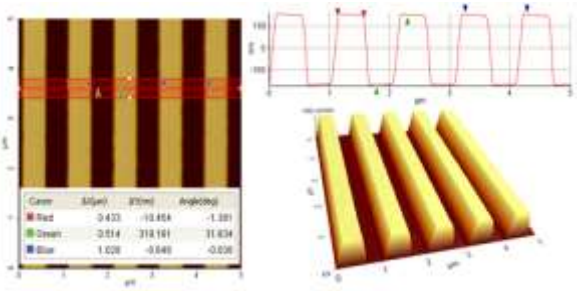

**Fig. 7.** AFM image of a fabricated Rayleigh reflector. Parameters: Λ = 1028 nm, F = 0.43, and $d_g$=319 nm.

Figure 6 schematically illustrates the model of the Rayleigh reflector. The angle of incidence θ is variable, generating the +1 diffraction order denoted as $T_1$ in the substrate for the numerical regimes treated. The period is sufficiently small such that only the zero-order transmitted ($T_0$) and reflected ($R_0$) waves propagate at normal incidence. The grating fabrication commences by sputtering a film of amorphous silicon (a-Si) on a clean glass substrate. The film is characterized by ellipsometry to determine its thickness and index of refraction. After spin coating a layer of photoresist (PR) on the a-Si film, patterning using a holographic interferometer operating at a wavelength of 266 nm is performed. With the PR as a mask, the a-Si layer is etched partially to form a 320-nm deep grating, leaving a sublayer next to the substrate as shown in Fig. 6. The device is inspected by atomic force microscopy (AFM). The AFM image of the fabricated device is shown in Fig. 7 with the experimental parameter values listed in the figure caption.

Figure 8 shows theoretical and experimental spectra at normal incidence. In the computation, we use optimized design parameters yielding a flat spectrum with $R_0$ = 1 across a 300-nm range. These parameters are close to the fabricated device parameters as determined by the AFM data. We apply our computer codes based on rigorous coupled-wave analysis for theoretical computations. Experimentally, we obtain a wideband reflector with spectral efficiency >95% across a ~220-nm wavelength range. Fundamentally, the device works as a GMR reflector with only $R_0$ prevailing above the Rayleigh wavelength ($\lambda_R = n_s\Lambda$ = 1548 nm) at normal incidence. For an arbitrary operating wavelength, the onset of the $T_1$ substrate wave occurs at the Rayleigh angle expressed as $\sin\theta_R = -n_s+\lambda/\Lambda$. If the operating wavelength is 1620 nm, the diffraction efficiency of $R_0$ is transferred to $T_1$ at $\theta_R = 4°$. To experimentally verify the predicted effect, we measure spectra across the same wavelength band for numerous selected angles of incidence.

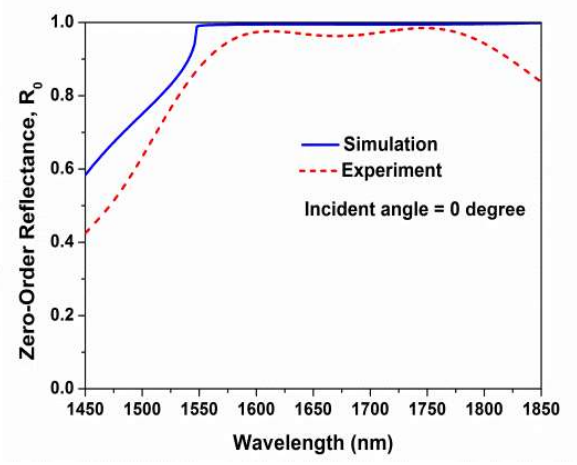


**Fig. 8.** Calculated and experimental spectral response of the Rayleigh reflector for TE-polarized light at θ=0°. Parameters: $d_g$ = 320 nm, $d_h$= 58 nm, n = 3.56, $n_c$ = 1, $n_s$ = 1.5, Λ = 1032 nm, and F = 0.43.

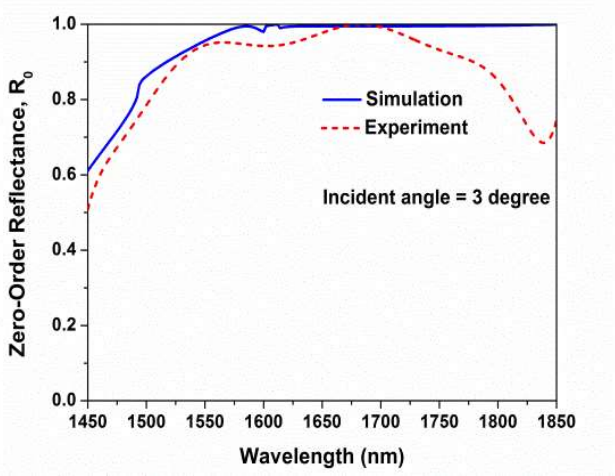


**Fig. 9.** Calculated and experimental spectral response of a Rayleigh reflector for TE polarized light at θ = 3°.

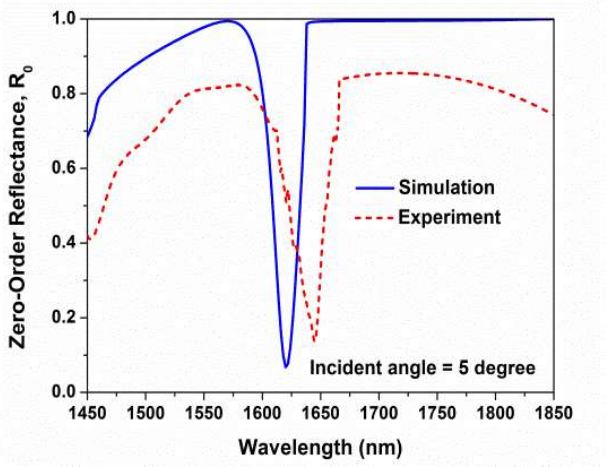


**Fig. 10.** Calculated and experimental spectral response of a Rayleigh reflector for TE polarized light at θ = 5°.

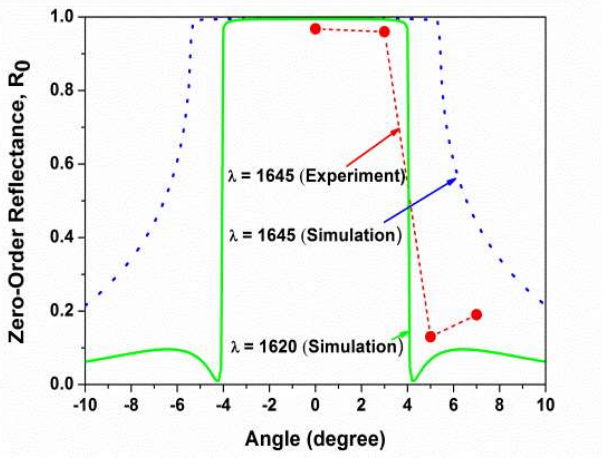


**Fig. 11.** Calculated and experimental angular spectra of a Rayleigh reflector under variation of the observation wavelength.

Figures 9 and 10 show the spectral responses at the incident angles of 3° and 5° respectively. In the experimental measurements, we see that when the incident angle changes from ~3° to 5° the diffraction efficiency of $R_0$ drops from ~96% to 13% at λ = 1645 nm. According to simulation, the operating wavelength at which the minimum reflectance occurs at an incident angle of ~5° is 1620 nm, variant from that of the experimental result, as seen in Fig. 10. The deviation can be attributed to differences in the experimental and model device parameters. Figure 11 provides experimental results and computed results at different operating wavelengths. Although there is considerable deviation between theory and experiment, the existence of a sharp efficiency exchange is experimentally verified. Spectral measurements at smaller angular intervals are expected to provide better match between theory and experiment. The ideal Rayleigh reflector

exhibits a wideband high-efficiency flattop spectrum and extremely rapid angular transitions as shown in Fig. 11 for $\lambda = 1620$ nm. Whereas we do not achieve this performance in the experiments reported here, these preliminary results indicate the existence of the enabling power exchange effect as seen in Fig. 11. Future experimental challenges reside in improving the fabrication precision to achieve the predicted performance.

## Testing of Meta-Optics at CREOL

As part of this project, the primary goal of the UCF team has been to provide/develop high power/high energy light sources based on Tm-doped fiber lasers for damage and thermal testing of novel GMRF devices. These efforts builds upon early collaborative research as part of our project on "*Multi-KW 2 μm Emission by Spectrally Combining many Tm Fiber Lasers"* (AFRL/JTO contract FA945110D0234) and a previous MRI on *"High Power Fiber Lasers"* (ARO/JTO contract W91NF0510517).

As summarized first in our annual report for 2011, these efforts have focused on improved development of high energy/peak power nanosecond mid-IR sources and the development of a method for "in-situ" characterization of laser-induced thermal distortion of optical materials. Based on advances in the development of metaoptic devices for 2 μm wavelength as part of this program, the UCF team has been able to expand these efforts to include application of annual beams.

1. Nanosecond Source Development
   As part of this project, significant achievements have been made in the development of high energy/high peak power Tm:fiber lasers and using these to pump mid-IR optical parametric oscillators (OPO). In order to improve the performance of Tm:fiber pumped mid-IR OPOs, the primary effort was focused on increasing the output pule energy while maintaining nearly diffraction-limited beam quality, highly polarized output, and narrow spectral linewidth. In large part this has been achieved by implementing ultralarge mode photonic crystal fiber (PCF) such as shown in figure 1.

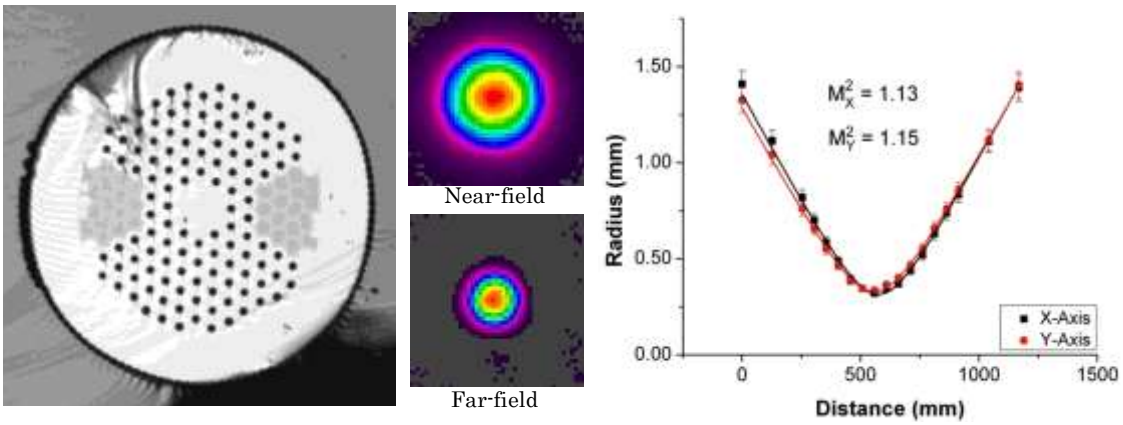


Figure 1: Image of PCF facet and associated beam quality

Table 1. DRO cavity results for 7 ns and 100 ns pump pulse durations

| Pump Pulse Duration (ns) | Wavelength (μm) | Max. Peak Power (kW) | Max. Pulse Energy (μJ) | Threshold Avg. Pump Power (W) | Avg. Power Slope Efficiency (%) |
|---|---|---|---|---|---|
| 7 | 3.7 | 14.8 | 88 | 0.27 | 38 |
| 7 | 4.1 | 13.1 | 78 | 0.27 | 38 |
| 100 | 3.7 | 2.08 | 150 | 1.27 | 49 |
| 100 | 4.1 | 1.86 | 134 | 1.27 | 49 |

Utilizing PCF technology, the UCF team developed a Tm:fiber MOPA system with >100 kW peak power to pump a mid-IR OPO. The performance of the laser and the OPO are described in[1] and the results are summarized in table 1 and figure 2. As part of related efforts, the UCF team was able to demonstrate amplification to ~1 MW peak power by utilizing a rod-type PCF[2] however the final amplifier was destroyed before this system could be applied for OPO pumping.

2. "In-situ" Characterization of Laser-induced Thermal Distortion

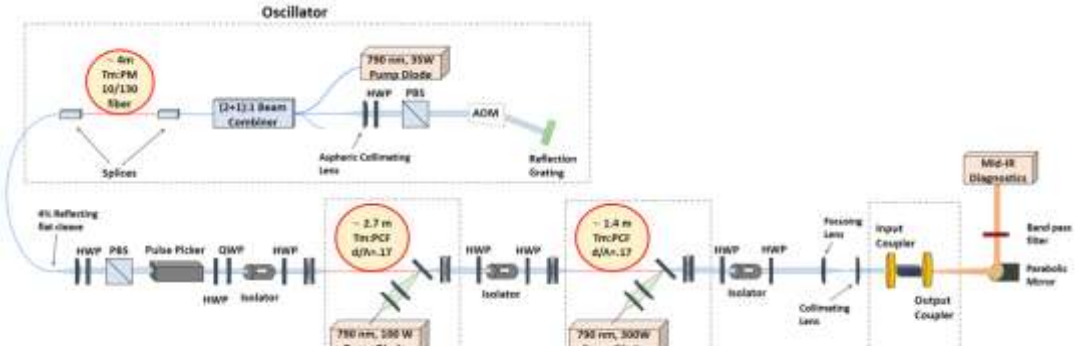


*Figure 1: Tm:fiber MOPA pumped mid-IR OPO schematic*

In support of efforts to power scale spectral beam combining of lasers at 2 μm wavelength, there was a clear need for an in-situ diagnostic of thermal distortion in passive optics for use at high power with 2 μm wavelength. An image of the laboratory setup is shown in figure 3. The setup consists of a CW "pump/probe" configuration in his the distortion induced by the "heating" beam is characterized by measuring the induce wavefront distortion on a probe beam. Data from this characterization method was critical to publications[3,4].

[1] M. Gebhardt, C. Gaida, P. Kadwani, A. Sincore, N. Gerlich, L. Shah, M. Richardson, "High peak power mid-IR $ZnGeP_2$ optical parametric oscillator pumped by Tm:fiber master oscillator power amplifier system," Opt. Lett **39** (2014) 1212-1215.

[2] C. Gaida, M. Gebhardt, P. Kadwani, L. Leick, J. Broeng, L. Shah, M. Richardson, "Amplification of nanosecond pulses to megawatt peak power levels in $Tm^{3+}$-doped photonic crystal fiber rod," Optics Letters **38** (2013) 691-693.

[3] L. Shah, R.A. Sims, P. Kadwani, C.C.C. Willis, J.B. Bradford, A. Sincore, M. Richardson, "High-power spectral beam combining of linearly polarized Tm:fiber lasers," Applied Optics **54**, 1 (2015) 757-762.

[4] C.C.C. Willis, J.D. Bradford, J. Haussermann, E. McKee, E. Maddox, L. Shah, R. Gaume, M. Richardson, "Rapid thermo-optical quality assessment of laser gain media," Optical Materials Express **5**, 6 (2015) 1389-1398.

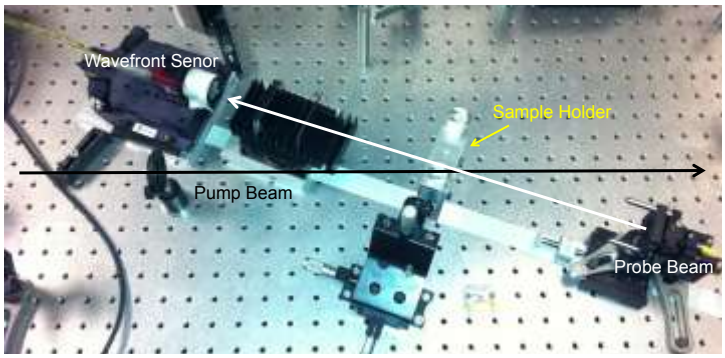


**Figure 2: Laser-induced thermal distortion setup**

As part of this project, this thermal distortion characterization system was used to characterize variations in the induced distortion associated with different coating materials based on sample from Prof. Talghader as shown in figure 4. The spectral beam combining system, was also used as a test bed to evaluate the potential of GMRF devices for high power spectral beam combining Tm:fiber lasers.

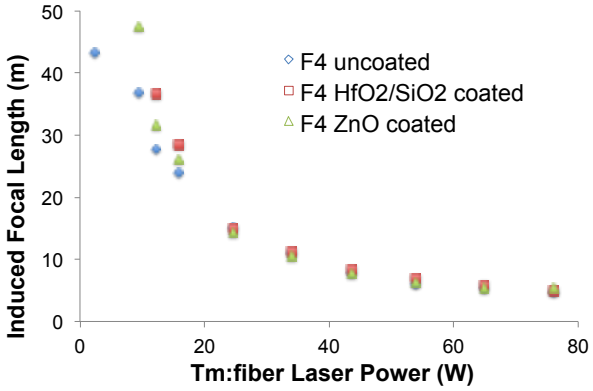


**Figure 3: Thermal induced distortion in coated samples supplied by Prof. Talghader**

These elements were designed (as shown in Figure 5) to provide selective reflectivity sensitive to angle of incidence, wavelength, and polarization to act as combining elements for SBC experiments. The experimental setup is shown schematically in Figure 6. The results of analysis of several initial samples fabricated by Prof. Johnson's group are summarized in table 2.

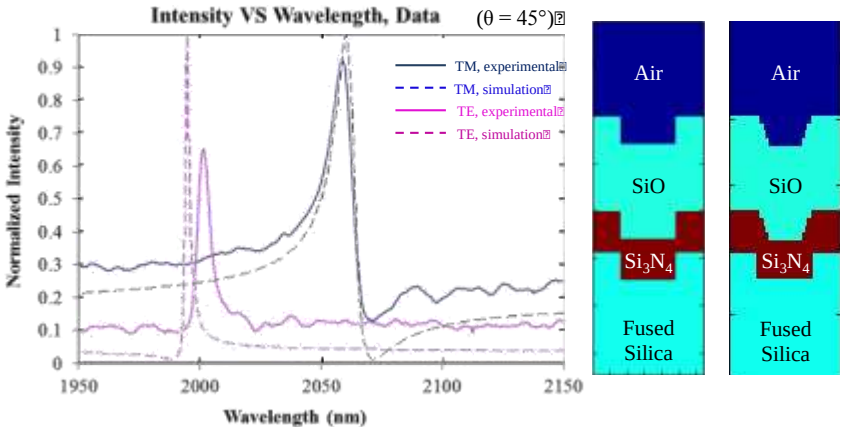


Figure 4: Configuration of GMR-based SBC elements

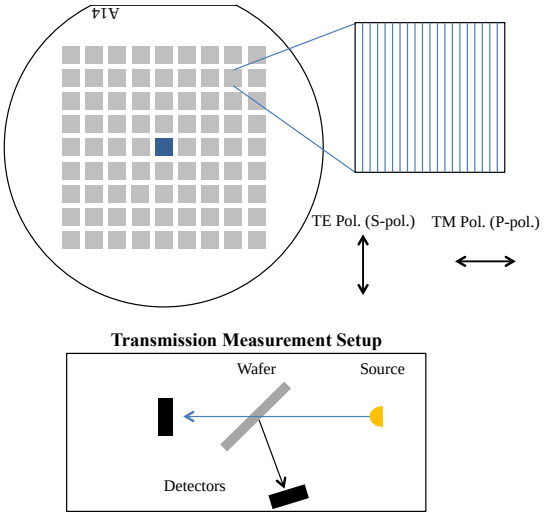


Figure 5: Wafer layout (top), experimental schematic (bottom)

Table 2: Evaluation of polarized reflection and transmission for two samples at several wavelengths and angles of incidence (AOI)

| A1 @ 31 AOI | %R @ 2039 nm | %T @ 2039 nm | %R @ 2044 nm | %T @ 2044 nm |
|---|---|---|---|---|
| S-Pol | 52.6 | 35.2 | 47.2 | 40.2 |
| P-Pol | 83.3 | 8.8 | 83.9 | 6 |
| | | | | |
| A1 @ 45 AOI | %R @ 2039 nm | %T @ 2039 nm | %R @ 2044 nm | %T @ 2044 nm |
| S-Pol | 45.7 | 38.6 | 43.1 | 38.5 |
| P-Pol | 71.7 | 8.3 | 81.4 | 10.3 |
| | | | | |
| A13 @ 43 AOI | %R @ 2039 nm | %T @ 2039 nm | %R @ 2044 nm | %T @ 2044 nm |
| S-Pol | 76.8 | 14.8 | 15.5 | 80.4 |
| P-Pol | 11.4 | 84.5 | 8.2 | 92.5 |
| | | | | |
| A1 @ 45 AOI | %R @ 2039 nm | %T @ 2039 nm | %R @ 2044 nm | %T @ 2044 nm |
| S-Pol | 39.7 | 61.2 | 37.1 | 58.9 |
| P-Pol | 9.6 | 87.4 | 7.5 | 91.9 |

We have further utilized the setup we have developed to characterize laser-induced thermal distortion to investigate the propagation of annular relative to Gaussian beams in the presence of thermal lensing[5]. The setup, illustrated in Figure 7, utilizes a homemade single-mode Tm:fiber laser and a BK7 window to induce thermal lensing. Using a vortex phase plate fabricated by the Clemson team to transform the Gaussian beam profile into an annular beam, we characterize the thermal distortion associated with the differences in beam profile.

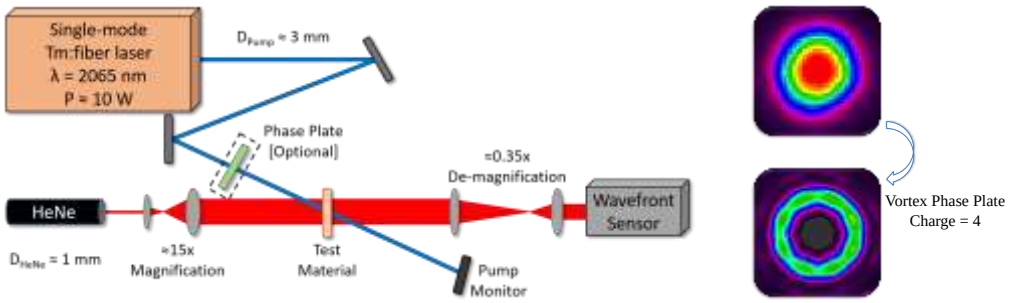


**Figure 6: Setup for laser-induced thermal distortion with a vortex phase plate to transform the Gaussian to an annular beam profile**

The wavefront characterization reveals that there is lower overall thermal distortion for an annular beam profile. This is most clearly shown in the lineouts of the phase profiles from which it is clear that the thermal distortion induced by the annular beam has a more flattop profile than for the Gaussian beam. These results have potential implications for applications requiring long-range propagation of high power lasers, and engaging in the implementation of annular beams at 2 μm wavelength for materials processing.

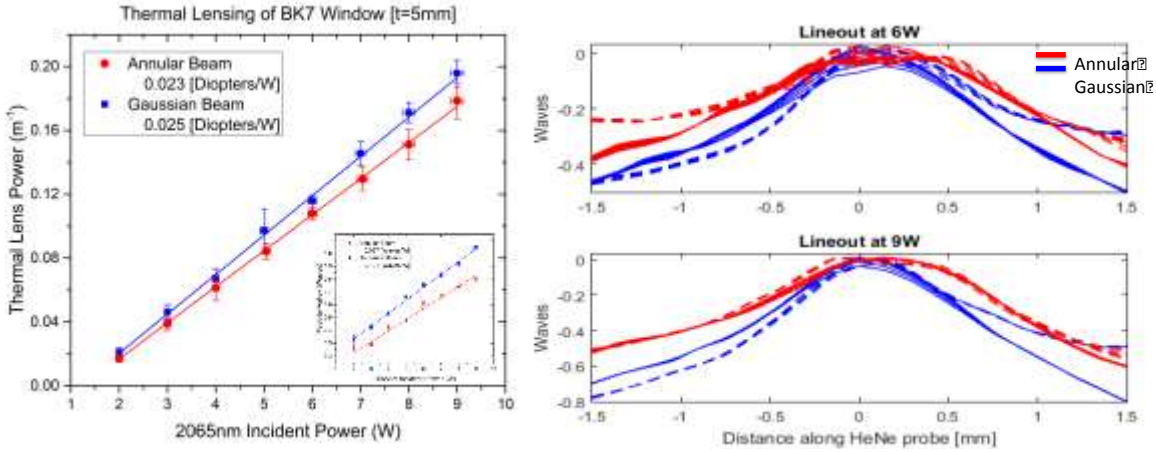


**Figure 7: (left) Thermally induced dioptric power as a function of incident power for Gaussian and annual beam profile (right) Lineouts of the thermally induced phase for annular and Gaussian beams at 6 and 9 W**

[5] A. Sincore, J. Cook, W. Li, E. Johnson, J. Bradford, L. Shah, M. Richardson, "Beam propagation of Gaussian and Annual Beams at 2 μm in the presence of thermal lensing," CLEO Science and Innovations 2016, paper JTh2A.77

## Meta-Optics Physics and Interface Studies (University of Minnesota)

One of our prominent achievements has been the development of a high speed interferometry system that can measure dynamic changes in optical and meta-optical surfaces. From our previous results, we found that metaoptic surfaces rebound and change spatially when impinged upon by a high power laser. In essence, an acoustic wave initiate upon the impact of the high power light on the surface which modulates the height of the meta-optic surface and changes the optical properties (which can be beneficial, detrimental, or of no consequence, depending on design and circumstances). In order to track this effect and determine its magnitude, we needed to develop a high-speed means of measuring acoustic waves generated by high power light.

Long-pulse and continuous-wave (CW) laser systems are often vital for specific applications requiring steady radiation to maintain high temperatures at a surface. The design of high-power long-pulse and CW laser systems has unique challenges. The damage process during ultra-short pulse irradiation has been well explored theoretically and experimentally to follow from field-induced carrier generation in pristine samples [1-4]. Fast pump-probe imaging studies have shown excellent agreement with carrier-induced breakdown theory [5-7]. On the other hand, CW damage often involves thermal effects from the longer irradiation time that are unrelated to ultra-short pulse field effects. Samples that perform well during short-pulse irradiation may actually perform poorly during CW irradiation. For example, polycrystalline films have higher scattering than amorphous films, resulting in diminished short-pulse performance [8], yet they also have higher thermal conductivity, which improves their CW performance [9,10]. CW irradiated samples have been known to break down during irradiation well after the substrate has reached steady state in field and temperature. Furthermore, the damage morphology and topography of a CW breakdown event can be more complex, involving larger volumes of material with more computationally-intensive modeling than short-pulse damage. Some damage features apparently are the result a combination of thermal and mechanical effects, which warrant further study [11].

In exploring these issues, it is desirable to have a monitoring system, which is able to observe temperature and mechanical variations at timescales faster than the thermal diffusion time. Furthermore, the temperature measured could potentially be a part of a single irreversible thermal process (i.e. laser damage). We desired an experimental setup

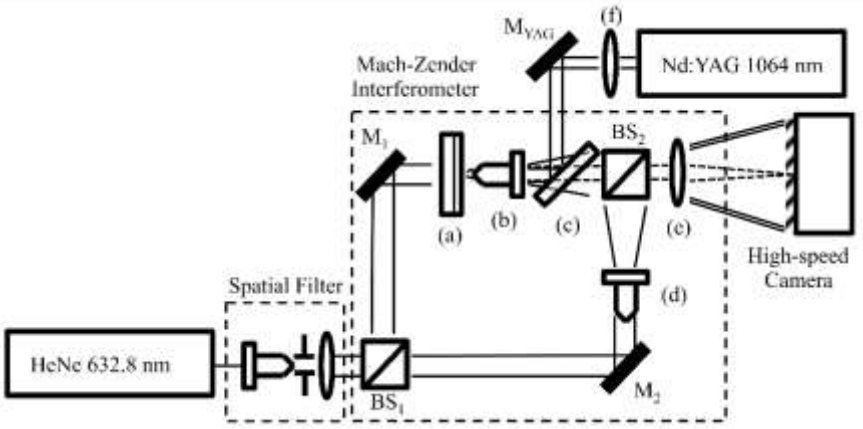


Fig. 1. High-speed phase measurement system. Our system utilized a HeNe laser, a Mach-Zender interferometer and a high-speed camera. The Mach-Zender interferometer was composed of mirrors M1 and M2 and non-polarizing beam-splitters BS1 and BS2. The temperature of a yttria-coated glass slide (a) was imaged with an objective asphere lens (b) and camera lens (e). The image was compared with a reference beam traversing an identical lens (d). The angle between beams was such that the temperature distribution was due to energy absorbed by a high-power Q-switched Nd:YAG laser coupled-in via a dichroic mirror (c) that reflected 1064 nm light and transmitted 632.8 nm light. Since the two lasers shared an objective lens, a dispersion-compensating lens (f) was necessary. The interferograms captured with the high-speed camera were transferred to a computer for conversion.

with the ability to capture individual irreversible events. Therefore, chopped or stroboscopic methods for measuring periodic events could not be used. Traditional thermal cameras have frame rates that are too slow and therefore this technique was also unavailable. In glass substrates, the thermal diffusion time is on the order of 1 millisecond ($\tau = L^2/D$, where $L$ = 25 μm and $D = 5\times10^{-7}$ m$^2$/s). We have developed a 2-dimensional monitoring system capable of capturing phase images of the sample surface at a rate of 11,800 frames-per-second (fps). These phase images correlate well with thermal phenomena via substrate thermal expansion and temperature-dependent refractive index effects.

*Experimental Setup*

Our experiment studied the temporal decay of the thermal wave created by laser energy absorbed by our yttria-coated microscope slide sample. The microscope slide was a Gold Seal 3010 soda lime silica glass slide. A distributor, Ted Pella, Inc., listed glass slide composition as follows: 72.2% silicon dioxide, 14.3% sodium oxide, 6.4% calcium oxide, 4.3% magnesium oxide, 1.2% aluminum oxide, 1.2% potassium oxide, 0.03% sulfur trioxide, 0.03% iron oxide. The yttria coating was deposited by thermal evaporation and was 300 nm thick. The total sample absorption was 0.1% as measured by our photothermal common-path interferometry (PCI) system. We did not notice significant difference in uncoated sample absorption vs. coated sample absorption, although absorption in both samples was primarily at the surface during PCI measurements. To

measure the temporal decay of a thermal wave, a fast method of measuring temperature was needed.

Phase measurement methods are often a convenient way of measuring physical quantities with traditional optical instruments. In particular, a Hilbert phase imaging technique suitable for transmission methods was developed for relatively high speed imaging systems [12]. We extended this system for use with an even higher frame rate camera with a suitably powerful probe beam, as shown in Figure 1. This required redesign of the magnification loop to meet our imaging needs as well as a different compensation scheme in the reference arm. We opted for an identical lens in the reference arm to simplify the setup. A common camera lens refocused the interfering light from both arms onto the camera. We added ND filters in the reference arm to compensate for the loss in the sample arm. We also added the ability to couple in an on-axis pump beam. Our system utilized an adapted Mach-Zender interferometer (MZI), operating at a wavelength of 632.8 nm, a high-speed camera capable of up to 20,000 fps and appropriate thermal models for substrate dynamics. In addition to commercial off-the-shelf optics, we utilized a polarized 15 mW JDSU HeNe laser, which was spatially filtered to be single mode, and an IDT NX4-S3 high-speed camera. We captured videos of our sample surface irradiated by Q-switched pulses from a multi-mode Nd:YAG laser operating at 1064 nm with a pulse width of 100 ns, a pulse energy of 10 mJ and a repetition rate of 2 kHz. Our Nd:YAG system was manufactured by U.S. Laser Corp. as model number 405-Q. We coupled the high-power pump beam via dichroic mirror, which transmitted the probe beam. This coaxial imaging system allowed the use of a commercial high numeric aperture objective lens for both pump and probe beams. The focused spot size of the Nd:YAG beam was approximately 10 microns. There was difficulty verifying this because the focused beam was too intense for use with a camera and it damaged our knife-edge methods. The beam width and $M^2$ were measured before focusing by a laser-beam analyzer and the focused spot was calculated. Our calculated beam waist was later verified by experimental data from the phase measurements. The sample was back-illuminated with the HeNe beam, which had a beam width of 3 mm. The image magnification system allowed a sample view area of 100 microns square. This sample area was magnified to fill an area on the 1" focal plane array of the high-speed camera. A smaller-than-maximum area was used to increase the camera frame rate. The small spot sizes and Rayleigh ranges of the pump and probe beams helped guarantee that the measurement was highly localized to the sample surface. Table 1 summarizes the experimental parameters used in this study.

**Table 1. Experimental parameters.**

| Symbol | Parameter | Value | Units |
|---|---|---|---|
| $\lambda_{Nd:YAG}$ | Nd:YAG wavelength | 1064 | nm |
| $t_{pulse}$ | Nd:YAG pulse width | 100 | ns |
| $f_{pulse}$ | Nd:YAG pulse repetition rate | 2 | kHz |
| $E$ | Nd:YAG pulse energy | 10 | mJ |
| $w_0$ | Nd:YAG beam width | 10 | μm |
| $M^2$ | Nd:YAG multimode parameter | 10 | - |

| | | | |
|---|---|---|---|
| $\lambda_{HeNe}$ | HeNe wavelength | 632.8 | nm |
| $w_{HeNe}$ | HeNe beam waist (in MZI) | 3 | mm |
| $\tau_{cam}$ | Camera shutter speed | 1 | μs |
| $f_{cam}$ | Camera Frame rate | 11800 | fps |

The interferograms produced by the phase measurements were stored as raw images and then later converted to temperature by computer post-processing. An example of this process for a frame captured <84 μs after an Nd:YAG pulse is shown in Figure 2. The interferograms were first converted to phase images by way of an algorithm described in [12]. Our phase-unwrapping technique utilized an open-source algorithm and code developed in [13,14]. The phase was then converted to optical path length. Our conversion is detailed in the next section. We assumed the phenomenon was primarily temperature dependent, so this optical path length was considered to be a function of temperature. Typically, temperature-to-phase conversions are a sum of thermal expansion terms and temperature-dependent refractive index terms. There is some uncertainty with these conversions as they rely on a priori knowledge of material constants. However, assuming the temperature is a close function of phase, the temporal decay of the temperature profile can be found from the phase data. Thermal diffusivity can be extracted from the temporal data without knowledge of absolute temperature. Figure 2 (g) shows the initial spatial pulse shape of the observed wave. This decayed with time and spread out spatially (shown in Figure 4), leading us to assume we were observing thermal phenomena.

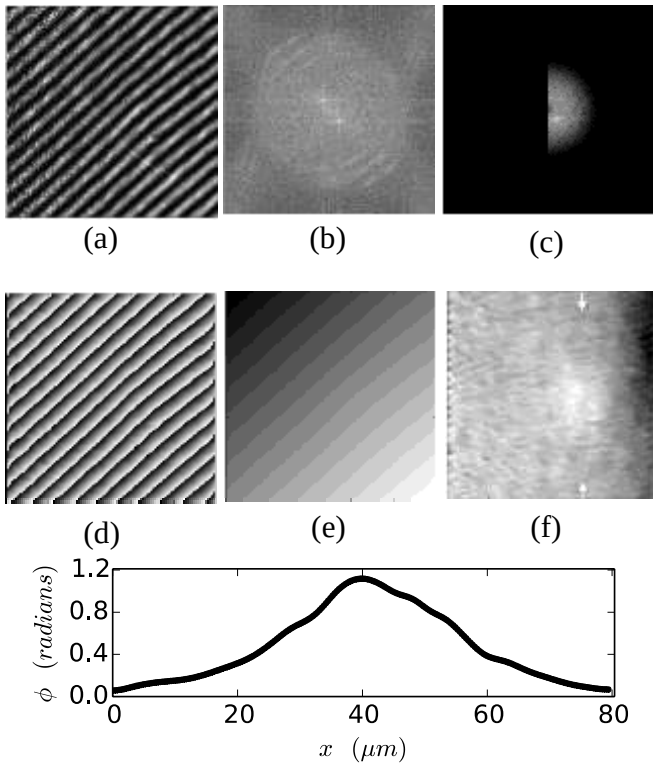

Fig. 2. Phase post-processing of an interferogram taken immediately (within 1 frame or <84 μs) after an Nd:YAG pulse. Starting with an interferogram (a), the image is Fourier-transformed (b), band-pass filtered and negative frequencies are removed (c). An inverse Fourier-transform without these negative frequencies results in a Hilbert transform. The argument of the now complex data is the phase image (d). The phase is unwrapped (e) and the fringe bias is removed (f) to give the phase image of the sample. A quantitative phase cross-section (g) is indicated by the arrows in (f). This pulse shape shows a Gaussian profile, which decayed and expanded with time - typical of thermal phenomena. All frames are 100 microns square.

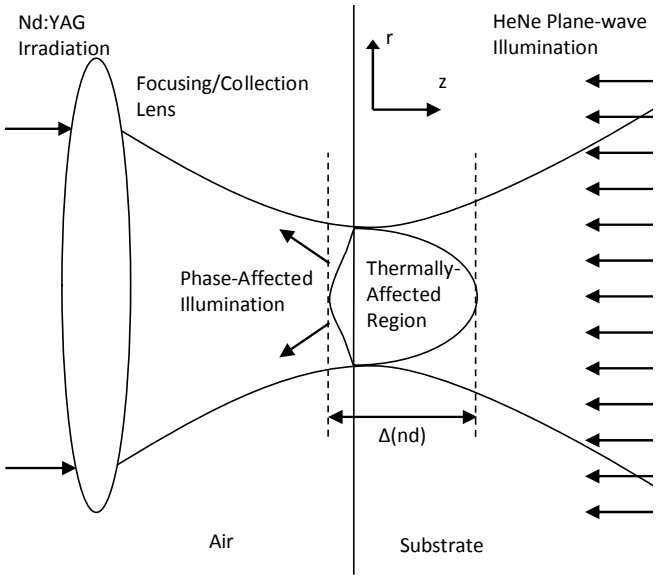


Fig. 3. Diagram of theoretical model. Energy from the pulsed Nd:YAG laser is focused to a spot on the sample surface. Absorbed energy causes material effects, which produce an optical path-length change, *Δ(nd)*, which produced a phase shift in the HeNe pseudo-plane-wave back-illumination. The phase-affected light is collected by the same focusing lens and carried to the imaging system which records the phase shift via a reference beam from the same HeNe illuminating laser. Coordinates r and z from Equations (1) and (2) are shown.

## 3. THEORETICAL BACKGROUND

The surface deformations in this work were assumed to be due to sample heating. Another effect that could produce surface deformation is photon pressure due to the high-power laser beam pushing on the sample surface. However, photon pressure was calculated to be appreciable only at microsecond timescales at high energies, given the study in [15]. Additionally, many mechanical phenomena involve a restoring force, which produces an inflection point in mechanical waves that should not be present in thermal waves and was not present in our data. To analyze experimental results, a theoretical model for the temperature distribution of a heated substrate was needed. Our temporal resolution was on the order of 100 microseconds, and we observed no anomalous behavior near the peaks. Therefore, we assumed a temperature-dependent explanation for the observed phenomena.

The temperature profile for short pulse laser heating has been calculated to have a product-solution form in cylindrical coordinates [16,17], shown in Equation (1), below. Here, $AE$ is the absorbed energy, $w_0$ is the beam waist (see Table 1), $\rho c$ is the heat capacity, $D$ is the thermal diffusivity (see Table 2) and $r$, $z$, $t$ are radial, depth and temporal coordinates, respectively. Here, short pulse means the laser pulse is short compared to the thermal diffusion time. We observed diffusion times on the order of milliseconds while the laser pulse length was under 100 ns, so our product solution temperature profile was a safe assumption.

$$\Delta T = \frac{AE}{2\pi^{3/2} r c \sqrt{Dt}\left(w_0^2 + 2Dt\right)} \exp\left(-\frac{r^2}{2\left(w_0^2 + 2Dt\right)}\right) \exp\left(-\frac{z^2}{4Dt}\right). \quad \textbf{(1)}$$

A useful quantity for optical path measurements is the integral of the temperature distribution into the sample, along the $z$-direction. This integrated quantity, at the center of the distribution ($r = 0$), is shown in Equation (2).

$$\int_{path} \Delta T \, dz \Big|_{r=0} = \frac{AE}{\pi r c\left(w_0^2 + 2Dt\right)}. \quad \textbf{(2)}$$

Our analysis uses (2) because our measurement system naturally integrates any phase measured over a finite depth. This depth contributes to the optical path length change due to the absorbed optical energy pulse. Note that, at $r = 0$, (1) and (2) are related by a $(4\pi Dt)^{-1/2}$ term. Although the temperature is theoretically larger at the time the laser pulse first hits, the path of length of the material affected is very small. Thus the measured phase distribution has reduced temporal dependence near the initial absorption event than one would expect from (1).

**Table 2. Sample parameters. Subscript *s* denotes substrate property , *f* denotes film property.**

| Symbol | Parameter | Value | Units |
|---|---|---|---|
| $A_{tot}$ | Total absorption[a] | 0.1 | % |
| $n_s^*$ | Refractive index (at 546 nm)[b] | 1.517 | - |
| $\alpha_s$ | Coefficient of thermal expansion[b] | $90.6\times10^{-7}$ | $K^{-1}$ |
| $\nu_s$ | Poisson's ratio[b] | 0.2 | - |
| $\rho_s$ | Mass density[b] | $2.48\times10^{3}$ | kg $m^{-3}$ |
| $c_s$ | Specific heat capacity[c] | 880 | J $kg^{-1}$ $K^{-1}$ |
| $D_s$ | Thermal diffusivity[d] | $4.6\times10^{-7}$ | $m^2$ $s^{-1}$ |
| $(dn/dT)s$ | Refractive index change with | $2.06\times10^{-6}$ | $K^{-1}$ |

| | | | |
|---|---|---|---|
| | temperature[e] | | |
| $(ds/dT)s$ | Optical path length change with temperature[d] | $2.1\times10^{-6}$ | $K^{-1}$ |
| $t_f$ | Film thickness[a] | 300 | nm |

[a]measured.
[b]Ted Pella, Inc. technical note.
[c]Industrial Glass Tech, Inc. technical note.
[d]Ref. [18].
[e]Ref. [19].

To extract the exact temperature dependence, the phase distribution was converted to temperature. Table 2 shows the parameters we used with Equations (1) and (2) for our theoretical model. Some data was not available from the slide distributor (Ted Pella, Inc.) and this was estimated from similar glasses from Industrial Glass Tech, Inc. and in [18,19], which were also phase measurement studies of laser absorption. The phase distribution was not imaged in these works, but they provided useful guidelines for our measurement. The phase data was assumed to be primarily due to thermal effects at the surface of the sample. However, the physical quantities in question were assumed to be primarily due to the substrate. We assumed that the film contributed negligible effects, other than some optical absorption, due to its small thickness (300 nm) compared to the thermal penetration depth (4 microns at 10 microseconds). We measured the total optical absorption at 1064 nm to be 0.1 % with our photothermal common-path interferometry system. Our theoretical framework is shown in the schematic in Figure 3. The difference in temperature caused by the pulse results in a path length change in the sample, which in turn produces a phase shift in the probe beam compared to the reference arm of the MZI. We took into account that absorbed optical energy affects the optical path length in two ways: thermal expansion and change of refractive index with temperature. These relations are expounded in Equations (3-6).

$$\Delta f_{tot}(t) = \frac{2\pi}{\lambda}\left[\int_{film}\left(\frac{ds}{dT}\right)_f \Delta T\,dz + \int_{sub.}\left(\frac{ds}{dT}\right)_s \Delta T\,dz\right] \tag{3}$$

$$\Delta f(t) = \frac{2\pi}{\lambda}\int_{path}\left[\left(n_s - 1\right)\left(n_s + 1\right)\alpha_s + \left(\frac{dn}{dT}\right)_s\right]\Delta T(z,t)\,dz. \tag{4}$$

$$\int_{path}\Delta T\,dz\Big|_{r=0} = \frac{\Delta f(t)/\left(2\pi/\lambda\right)}{\left(n_s - 1\right)\left(n_s + 1\right)\alpha_s + \left(dn/dT\right)_s}. \tag{5}$$

$$\Delta T(t) = \left[\int_{path}\Delta T(z,t)\,dz\Big|_{r=0}\right]/\sqrt{4\pi D t}. \tag{6}$$

If $s$ is the optical path length of the MZI sample arm, Equation (3) shows a total phase change due to thermal path length changes in the film, $(ds/dT)_f$, and in the substrate, $(ds/dT)_s$. The temperature in each region is integrated. However, as was previously

mentioned, because the film is so much thinner than the thermal penetration depth in the substrate and its absorption is relatively low, we neglected the film term in our analysis. Should the film terms in Equation (3) increase, in a multilayer film, for example, the phase-to-temperature relationship would be a more complicated sum of film and substrate, expansion and *dn/dT* effects. Equations (4) and (5) show our method of converting phase to integrated temperature and equation (6) shows the relationship between integrated temperature and our original distribution in (1). The values used for heating due to expansion and refractive index change were both on the order of 2 ppb per 1 °C. Therefore, the peak phase deviations of 1 radian at $t$ = 10 μs correspond to temperatures of 1700 °C. This is rather large, but becomes reasonable when one considers that the absorbed pulse energy density is approximately 1010 J/m$^3$. This matches well with the exact evaluation of (1) at $r = z = 0$, and $t$ = 10 μs with the substrate terms in Tables 1 and 2, which is 1800 °C.

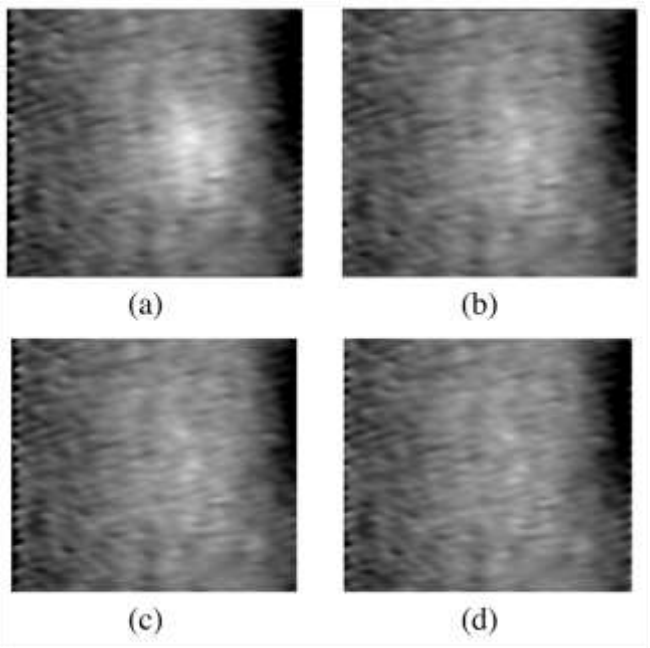


Fig. 4. Temporal phase phenomena observed on yttria-coated glass slide. The first frame (a) is the closest frame captured after the laser pulse was absorbed by the sample. Frames (b)-(d) show this initial pulse dissipating. Frames are 100 microns square. A sequenced video of this figure is available in the multimedia file, Visualization 1.

## 4. RESULTS

Figure 4 shows four successive frames out of a 100-frame measurement following 16 pump pulse cycles. The associated multimedia file, Visualization 1, sequences these images. With this data, we were in a position to test our theoretical framework. We used Equations (1) and (2), along with the parameters in Tables 1 and 2, to analyze our data spatially and temporally. Therefore, independent temperature measurements were not necessary to find meaningful quantities from the phase data.

As shown in Figures 1 and 3, we aligned the pump and probe beams such that both focal points occurred at the sample surface. After doing this, we observed faint periodic deviations in the video composed of consecutive high-speed interferogram frames, as

shown in Figure 4. After processing, we observed periodic phase waveforms closely corresponding to the Gaussian shape given by theory. Clearly evident in Figure 4 is the central phase displacement in the first frame, which decays over the next three. Additionally, there is very little wave propagation evident in the radial direction. The wave appears to simply decay with relatively small radial expansion. Looking to (1), this implies a beam area that is slightly wider than the diffusivity multiplied by time over the lifetime of the wave. These initial observations were investigated further.

### A. Temporal data

We plotted the center point of the thermal waves over time - i.e. the point at the peak of Figure 4 (a). Due to the nature of the experiment, phase measurements were a sum of effects through a finite depth of the sample. Therefore, it was appropriate to fit the data to the integral of the temperature distribution, as in Equation (2). Figure 5 shows temporal data at the center of the beam fit with a least squares fitting algorithm, using Equation (2). The fitted parameter produced a thermal diffusivity of $5.4\times10^{-7}$ m/s$^2$ which is in agreement with the substrate diffusivity in Table 2.

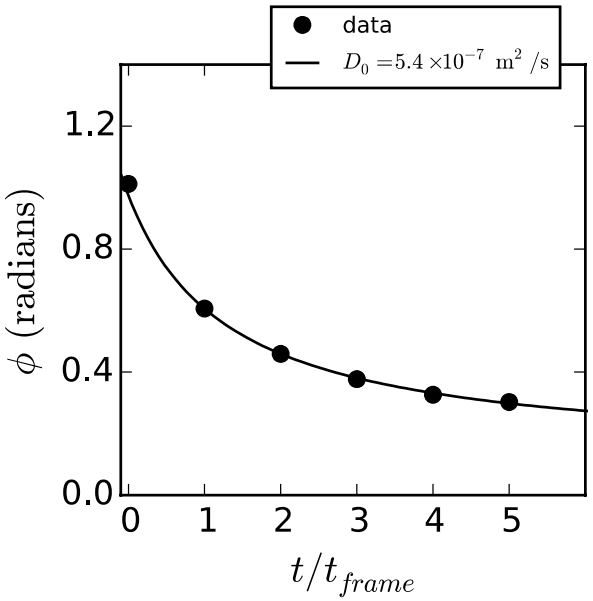


Fig. 5. Temporal decay of the temperature pulse. Data taken at the center of the temperature distribution. Also shown is a solid depicting a fit using (2). The diffusivity fit is in good agreement with literature values. The frame-rate here was 11,800 fps, which corresponds to a frame period of 84.7 μs.

**B. Spatial data**

Cross-sectional data from the images in Figure 4 are shown in Figure 5. This data shows that while the beam spread with time was small, it was measureable. Further analyzing (1), a beam-area time-dependence can be observed in the argument of the *r*-term.

$$w^2(t) = w_0^2 + 2Dt. \tag{7}$$

Where w is the beam waist. The spread of the thermal wave in the frames was found by extracting a 1D cross-section that intersected the same peak point used in the temporal analysis. This data slice was fit to a Gaussian function and the waist of this Gaussian used as the waist of a fit to (6).

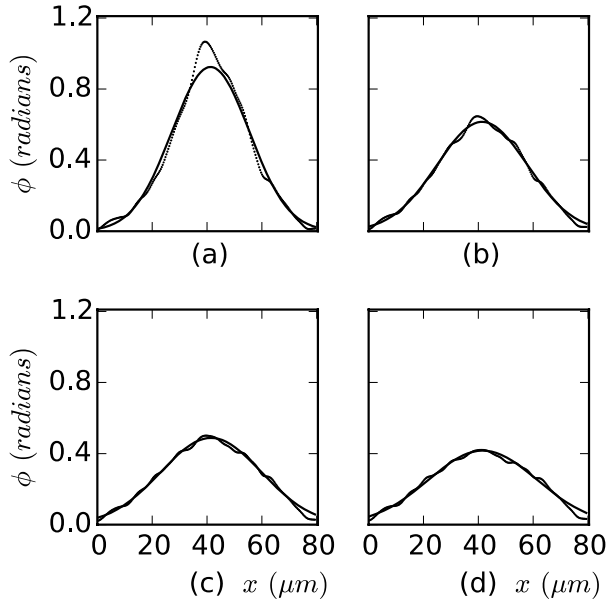


Fig. 6. Radial temperature distribution in the four frames captured immediately after the laser pulse. The beam waist was quantified by fitting a Gaussian function (solid line) to the data (points). Subfigures (a-d) show fits from four successive frames.

Figure 6 shows that the shape of the absorbed energy is Gaussian in the radial direction, as predicted by (1), and that it expands with time. The initial beam waist of 18 microns in Figure 6 (a) expanded to 21 microns, in (b), in the time between energy absorption and the first frame. It further expanded to 23 (c), 25 (d) and 27 microns (not shown) in the three successive frames. Fitting the square of the beam waist to the linear equation (6) produces a diffusivity of $5.3 \times 10^{-7}$ m$^2$/s. This linear fit is shown in Figure 7.

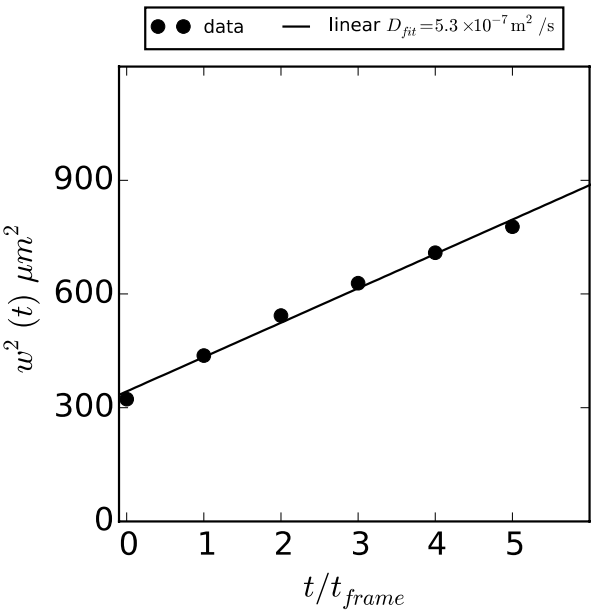


Fig. 7. Fitted Gaussian widths-squared from Figure 6, plotted against time. A thermal diffusivity can be extracted from a linear fit to this data, according to Equation (6).

## 5. DISCUSSION

It should be noted that the phase measurements were made relative to a reference point in the lower left corner of the frame (see Figure 4). The absolute phase of the frames varied strongly due to noise in the optical system. Subtracting a small reference region removed this overall frame noise while allowing us to glean physical data from within the frame. However, as the thermal wave expanded and entered the reference region an error term entered the measurement. This term was negligible in the first few frames of a pulse event, but became important as the frames accumulated as shown in Figure 8. This appeared in the temporal measurements and also complicated to the spatial measurement. Additionally, there was finite noise due to imperfections in the optical system. Some of this noise remained after reference point subtraction. This contributed to the temporal measurement and absolute temperature conversion, but was easily averaged over the spatial measurement. Finally, the lens system we used produced a finite distribution (i.e. the fringes were not perfectly straight). This produced no noticeable effects and the fringes appeared straight enough for our purposes.

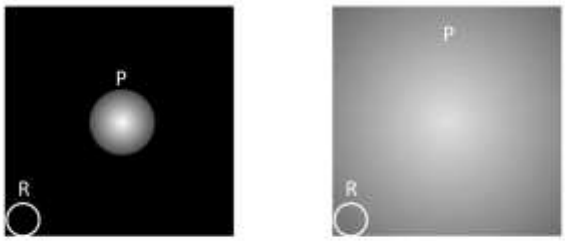

Fig. 8. Accumulation error demonstrated with mock example phase frames. In (a) the absorbed laser pulse energy, *P*, is far from the reference region, *R* and the reference region can be safely subtracted to remove any absolute noise in the frame. In (b) the pulse energy has spread into the reference region and the frame will be incorrectly referenced.

The first frame of the temporal fit was assumed to be coincident with a frame of the measurement. In reality, there was a finite delay between the pulse absorption event and the first frame of the measurement. As a worst case this delay could have been up to a full frame of 87 μs. Jitter analysis showed that the diffusivity fit varied strongly with the delay and was up to an order of magnitude larger in the worst case of being off by a full frame. However, our camera measurement was electronically triggered with a gate signal, which also triggered the laser. The trigger delay was not likely more than 1 μs and our data fit produces accurate results, so our assumption appears to be reasonable.

## References


1. B. Stuart, M. Feit, A. Rubenchik, B. Shore, and M. Perry, "Laser-Induced Damage in Dielectrics with Nanosecond to Subpicosecond Pulses," Phys. Rev. Lett. **74**, 2248 (1995).
2. B. Stuart, M. Feit, S. Herman, A. Rubenchik, B. Shore, and M. Perry, "Nanosecond-to-femtosecond laser-induced breakdown in dielectrics," Phys. Rev. B **53**, 1749 (1996).
3. J. Jasapara, A. Nampoothiri, W. Rudolph, D. Ristau, and K. Starke, "Femtosecond laser pulse induced breakdown in dielectric thin films," Phys. Rev. B **63**, 045117 (2001).
4. M. Mero, J. Liu, W. Rudolph, D. Ristau, and K. Starke, "Scaling laws of femtosecond laser pulse induced breakdown in oxide films," Phys. Rev. B **71**, 115109 (2005).
5. M. Downer, R. Fork, and C. Shank, "Femtosecond imaging of melting and evaporation at a photoexcited silicon surface," J. Opt. Soc. Am. B **2**, 595 (1985).
6. S. Demos, R. Raman, and R. Negres, "Time-resolved imaging of processes associated with exit-surface damage growth in fused silica following exposure to nanosecond laser pulses," Opt. Express **21**, 4875 (2013).
7. N. Šiaulys, L. Gallais, and A. Melninkaitis, "Direct holographic imaging of ultrafast laser damage process in thin films," Opt. Lett. **39**, 2164 (2014).
8. S. Zaitsu, S. Motokoshi, T. Jitsuno, M. Nakatsuka, and T. Yamanaka, "Laser Damage Properties of Optical Coatings with Nanoscale Layers Grown by Atomic Layer Deposition," Jpn. J. Appl. Phys. **43**, 1034 (2004).
9. N. Gabriel and J. Talghader, "Thermal conductivity and refractive index of hafnia-alumina nanolaminates," J. Appl. Phys. **110**, 043526 (2011).
10. L. Taylor, A. Brown, A. Pung, E. Johnson, and J. Talghader, "Continuous-wave laser damage of uniform and nanolaminate hafnia and titania optical coatings," Opt. Lett. **38**, 4292 (2013).
11. L. Taylor and J. Talghader, "Ring-like damage morphologies produced by continuous-wave laser irradiation," Proc. SPIE 9237, 92371L (2014).
12. T. Ikeda, G. Popescu, R. Dasari, and M. Feld, "Hilbert phase microscopy for investigating fast dynamics in transparent systems," Opt. Lett. **30**, 1165 (2005).
13. M. Herráez, D. Burton, M. Lalor, and M. Gdeisat, "Fast two-dimensional phase-unwrapping algorithm based on sorting by reliability following a noncontinuous path," Applied Optics **41**, 7437 (2002).

14. G. Thalhammer, Unwrap: a phase unwrapping module (version 0.1.1) [software] (2015), http://pypi.python.org/pypi/unwrap.
15. T. Požar and J. Možina, "Measurement of Elastic Waves Induced by the Reflection of Light," Phys. Rev. Lett. **111**, 185501 (2013).
16. J. Ready, Effects of High-Power Laser Radiation (Academic, 1971).
17. K. Olson, A. Ogloza, J. Thomas, and J. Talghader, "High power laser heating of low absorption materials," J. Appl. Phys. **116**, 123106 (2014).
18. M. Baesso, J. Shen, and R. Snook, "Mode-mismatched thermal lens determination of temperature coefficient of optical path length in soda lime glass at different wavelengths," J. Appl. Phys. **75**, 3732 (1994).
19. G. Ghosh, "Model for the thermo-optic coefficients of some standard optical glasses," J. Non-Cryst. Solids **189**, 191 (1995).

Laser Damage of Meta-Optics and Unpatterned Amorphous and Polycrystalline Materials

Studies of laser-induced damage threshold (LIDT) as a function of material properties have been mostly performed with relatively short pulse laser radiation. Some of the early studies found that amorphous materials have higher laser damage resistance in the femtosecond regime due to increased resistance to avalanche breakdown [3–7]. The fundamental damage mechanisms in this regime are multiphoton absorption followed by free electron absorption and avalanche breakdown. These mechanisms are fairly accurate for describing damage in defect-free samples. However, it is well known that laser damage thresholds and mechanisms vary widely with pulse length [3,8,9]. Damage mechanisms in the continuous-wave (CW) regime are less well understood. Studies have been performed with highly absorbing semiconductor samples [10–12] and coated dielectric optics [13–17]. These damage studies have described thermal distortion, phase change dynamics, and contamination but little is known about the role of material crystallinity. To our knowledge, the only other study of the laser damage threshold of nanolaminate (NL) films found that the nanolaminates had increased damage resistance over standard films for 1 ns pulses [18]. In that study, the authors attributed the increased damage resistance of the nanolaminate film to reduced optical scattering and, subsequently, reduced absorption, as in [1] and [2]. In Figures 1-4 below, we see images that show differences in the behavior of normal and nanolaminate thin films in the short pulse and CW regimes. In our research of the past year, Luke Taylor showed that for long duration pulses and under CW illumination, polycrystalline materials have improved laser damage thresholds compared to amorphous nanolaminates, the opposite of the behavior for ultra-short pulses as found in the cited work above.

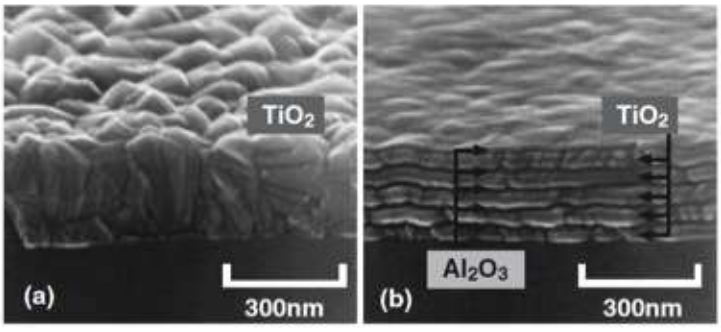


**Figure 1** – (Prior Research) SEM image of pure $TiO_2$ film (left) and nanolaminate film (right) [Zaitsu et al, 2004]

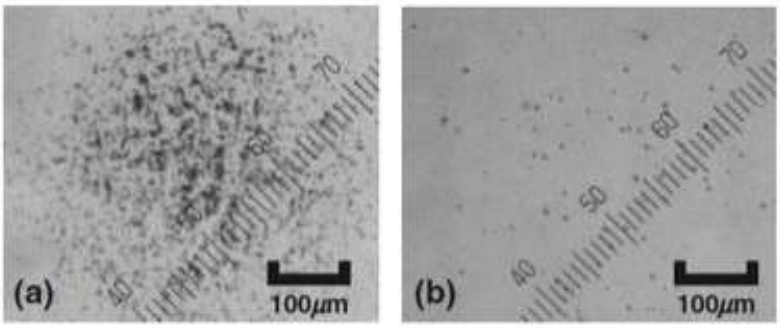


**Figure 2 –** (Prior Research) Pulsed (1 ns) damage morphologies of pure $TiO_2$ film (left) and nanolaminate film (right) [Zaitsu et al, 2004]

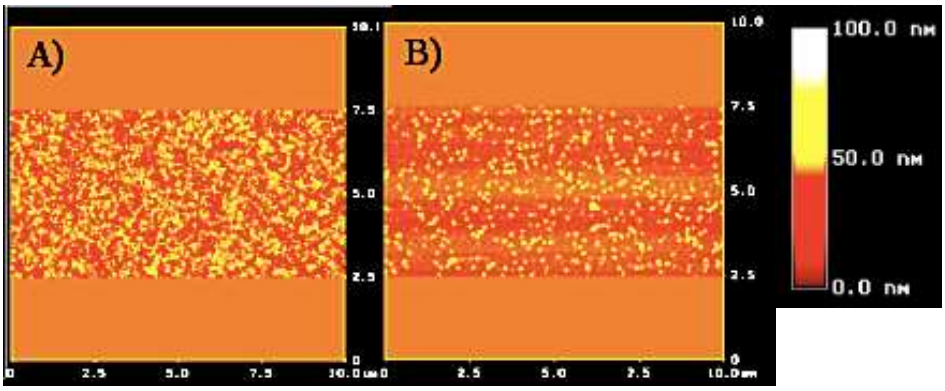


**Figure 3 -** AFM scan of pure $TiO_2$ film (left) and nanolaminate film (right) from [Taylor and Talghader DEPS Symposium 2012]

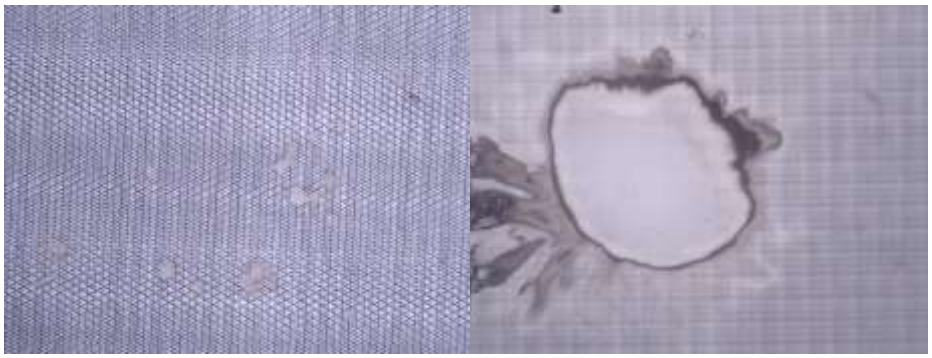

**Figure 4 -** CW damage morphologies of pure $TiO_2$ film (left) and nanolaminate film (right) at the same fluence [from Taylor and Talghader DEPS Symposium 2012]

## Deposition and Characterization

We performed laser damage experiments on two classes of coatings. The first was composed of uniform films of hafnia and titania. The hafnia and titania films had thicknesses of 100 nm and 60 nm, respectively. The second class was nanolaminate films, composed of a primary film layered with a secondary film designed to mitigate crystal grain formation in the primary film [19]. For example, the nanolaminate hafnia film was grown by depositing 10 nm of hafnia, followed by 1 nm of alumina, and repeating this period 10 times for an approximately 100 nm total film thickness. Our alumina films are amorphous and serve to mitigate crystal growth in the hafnia films. A similar recipe was followed for the titania/alumina nanolaminate. We used an atomic layer deposition process for all films using a Cambridge NanoTech Savannah ALD system. The films were grown by pulsing 1 half-cycle of metalorganic precursor, followed by a nitrogen purge, followed by 1 half-cycle of water vapor, followed by a final nitrogen purge to complete the cycle. The hafnia metalorganic precursor was tetrakis(dimethylamido) hafnium (TDMAH), the titania precursor was titanium tetra(isopropoxy) (TTIP) and the alumina precursor was trimethylaluminum (TMA). Substrate temperature for all films was 250 °C.

The films were deposited on fused-silica substrates. The substrates had patterned regions as well as smooth, unpatterned regions. The patterned regions were designed as photonic crystal filters resonant at 1.55 μm [21]. The pattern design was as follows: the substrates were fused silica and had a hexagonal pattern of pits etched into the surface; the etch pits were 600 nm in diameter and 300 nm deep; the grating period was 1150 nm in the hexagonal crystal direction. We found that the uncoated substrates were very difficult to damage with our laser system at even the highest laser power levels. The patterned regions of the coated substrates appeared to have reduced damage thresholds but still had values near the limit of our ability to measure. On a pragmatic level, the patterned substrate made identifying damage sites easy.

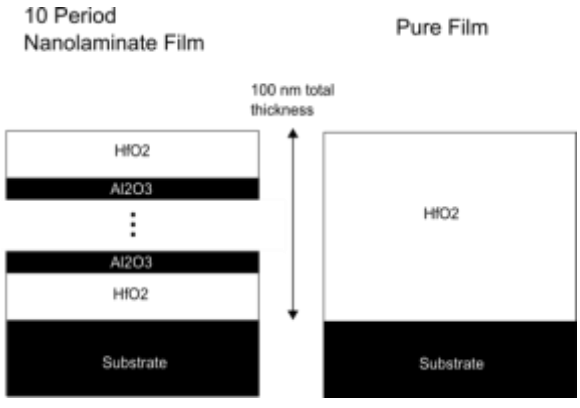


*Figure 5 – From last year's report, a typical layer structure of a nanolaminate and a normal film deposited by atomic layer deposition. These stacks were deposited on both patterned meta-optic and clean substrates.*

Film Properties

| Film | Thickness (nm) | Crystallinity* (%) | Thin Film Thermal Conductivity (W/m K) |
|---|---|---|---|
| $HfO_2$ | 100 | 40 | 1.72[1] |
| $HfO_2$ NL | 100 | 3 | 1.02[1] |
| $TiO_2$ | 70 | 9 | 1.6[2] |
| $TiO_2$ NL | 30 | 2 | - |

*Measured using JADE peak-fitting software on XRD data
**General known values
[1]Gabriel and Talghader, JAP, 2011
[2]Cahill and Allen, APL, 1994

## Crystallinity of Nanolaminates

The crystallinity of the films was measured using both atomic force microscopy (AFM) and x-ray diffraction (XRD) with films deposited on silicon substrates for testing purposes. The AFM measurements used a Brucker Dimension 3000 atomic force microscope in tapping mode and provided physical data on the surface roughness, which is often an indicator of the polycrystalline grain structure. The XRD data was collected on a Siemens D-500 Diffractometer and the crystallinity was quantified using Materials Data, Inc. JADE XRD analysis software and materials database. The data was collected for diffraction angles between 20 and 90 degrees and the results were compared against the JADE database of material XRD signatures. Crystallinity was quantified by a JADE algorithm which compares the area under the sharp crystal peaks in the data to the wider amorphous peaks. The nanolaminates had both smoother AFM profiles and drastically reduced crystal peaks in the XRD data than the uniform films, as shown in figures below. Thus we found that the nanolaminates used in our study were indeed more amorphous than the films without the alumina spacer layers, as expected from prior research [19,20].

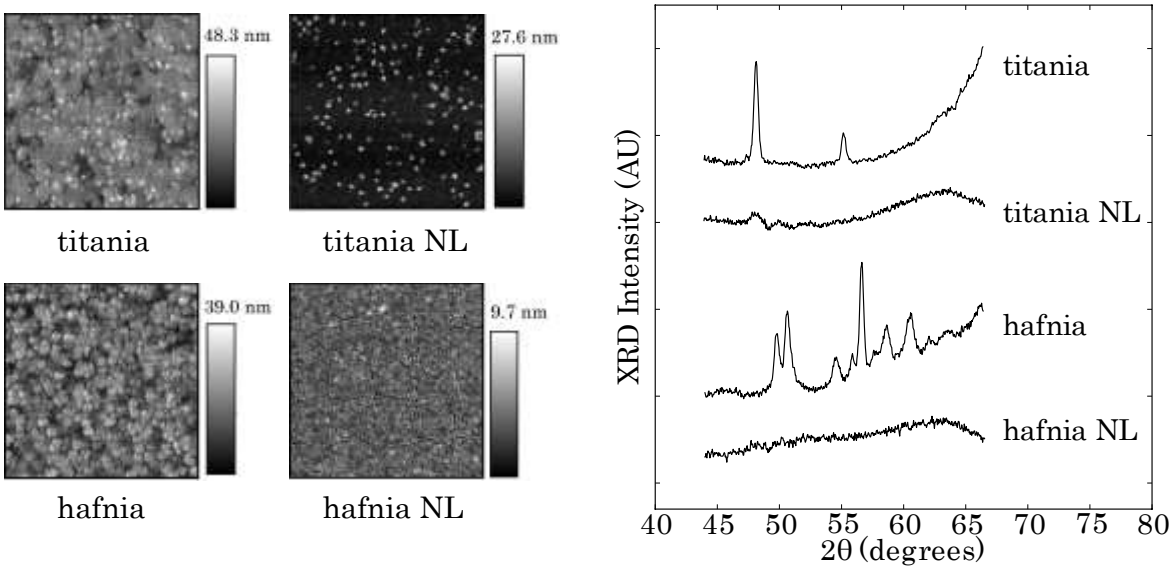


*Figure 6 – Surface rounghness and crystal structure of hafnia and titania normal and nanolaminate films.*

Laser Damage of Nanolaminates

Damage tests were performed by performing a row of 1-on-1 tests at constant irradiance while observing the samples for visible damage at 20x magnification. Our 1-on-1 tests consisted of 3 steps. First, we identified a test site free of visible defects. Second, we irradiated the sample for 6s with either CW or pulsed radiation. The pulsed radiation was a 6 s pulse train of 60 ns Q-switched pulses at a pulse repetition frequency of 5 kHz. During this step we also measured the average beam power and beam profile. Finally, the sample was examined for damage before proceeding to the next test site. On average, 5 damage sites were tested per power level. We started with our maximum irradiance and then stepped to lower values until the damage threshold was reached. The damage thresholds

were calculated as the average power levels at which damage occurred for approximately 50% of the tests. Our laser damage source was a multi-mode Nd:YAG Q-switched laser operating at a wavelength of 1064 nm. The beam was normal-incident. The spot size was nominally 200 μm. A small spot size was necessary to achieve high enough irradiance to cause damage. The laser power (average power for Q-switched pulses) was monitored using a Newport 818T thermopile detector. The beam waist was measured before focusing using a Cohu 4812 CD camera and Spiricon analysis software. Lens equations were used to estimate the spot size after focusing. These calculations were verified at low power levels using the CCD camera. Accurate beam spot size measurement at the sample was difficult at high power levels and we relied on estimation. While damage threshold numbers carry significant uncertainty, the damage levels of the different film materials and morphologies were clearly distinct. The damage setup is shown in in the figure below

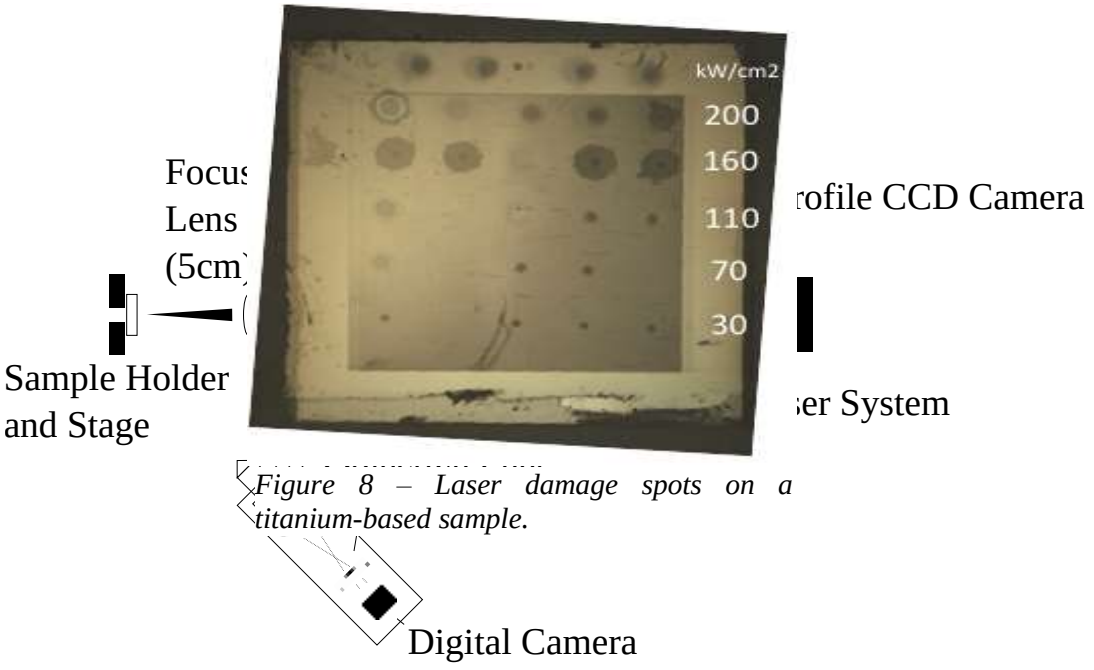


*Figure 8 – Laser damage spots on a titanium-based sample.*

*Figure 7 – Experimental set-up for CW and long-pulse laser damage testing.*

We found that the uniform films clearly had higher damage thresholds than their nanolaminates for both hafnia and titania-based films, for both patterned and unpatterned substrates and for both 60 ns Q-switched pulsed irradiation and CW irradiation. Also, the hafnia films had higher damage thresholds than the titania films, in general. This agrees with other laser damage studies of the two materials [22]. This data is summarized in Tables 1 and 2.

**Table 1: Unpatterned Substrate LIDT**

| Film | 60 ns Pulsed LIDT (kW/cm2) | CW LIDT (kW/cm2) |
|---|---|---|
| Fused Silica (Substrate) | >190 | >250 |
| hafnia | <190 | 230 |
| hafnia NL | <190 | 130 |
| titania | <60 | 80 |
| titania NL | <60 | 20 |

**Table 2: Patterned Substrate LIDT**

| Film | 60 ns Pulsed LIDT (kW/cm2) | CW LIDT (kW/cm2) |
|---|---|---|
| Patterned Fused Silica (Substrate) | >190 | >250 |
| hafnia | 110 | 160 |
| hafnia NL | 70 | 100 |
| titania | 10 | 30 |
| titania NL | 1 | 5 |

Almost all of the tests where the irradiation was significantly above threshold produced a plasma flash and audible acoustic shock wave in the air. This is indicative of material heating, ultrasonic wave generation and evaporation at the onset of damage [23–25]. The tests that produced audible shock waves did so within the first few milliseconds of the 6s laser irradiation, i.e. there were no tests which produced shock waves near the middle or end of the 6s irradiation.

Uniform and nanolaminate films had different damage morphologies. The figure below shows a 5x5 array of damage sites. Each horizontal row of sites was tested at the same power level. The power level was stepped from the high to low power levels from top to bottom in both images. The nanolaminate film had higher ratio of damaged sites to total test sites for each row of constant irradiance, except for the top row in which both films were damaged for all 5 tests. In addition, the damage spots of the nanolaminate film were larger in radius than the spots in the uniform film. The figure below shows typical laser

damage morphologies. Near threshold, laser damage spots were smaller than the beam width. Well above threshold, spots were on the order of the beam width. The ring-like morphology may be due to shock wave generation or thermally-induced stress [22,26].

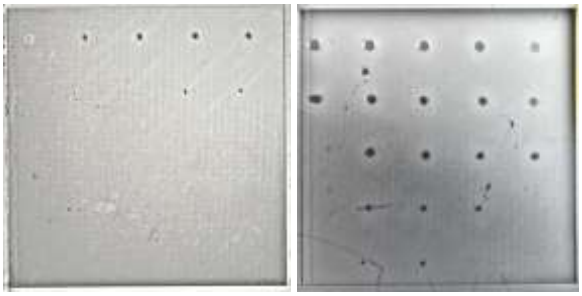

titania titania NL

*Figure 9 - Laser damage tests clearly show the reduced LIDT of the nanolaminate film (right).*

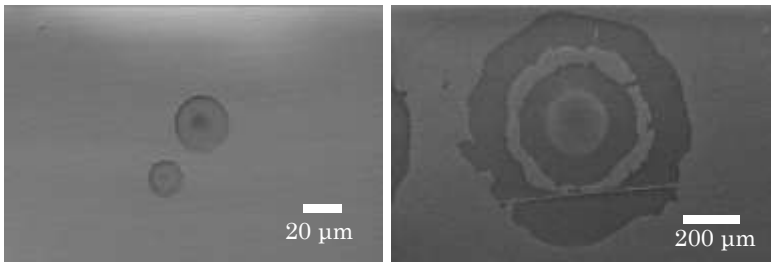


(a) (b)

*Figure 10 - Laser damage morphologies (a) near threshold and (b) well-above threshold. Note change of scale bar.*

We performed similar laser damage tests on patterned and unpatterned regions of samples fabricated by our collaborators at the University of Clemson. We found that the patterned regions had significantly reduced laser damage resistance for both CW and pulsed irradiation.

**Table 4: Q-switched and CW Laser Damage Threshold of A31 Fused Silica Substrates with Alumina Inclusions**

| Substrate | Q-switched LIDT* (kW/cm$^2$) | CW LIDT** (kW/cm$^2$) |
|---|---|---|
| Unpatterned | 50 | 250 |
| with Patterned Inclusions | 35 | 30 |

*Average power Q-switched LIDT was calculated as the power level at which damage probability was 0.5.
**CW LIDT was calculated as the power level at which damage probability was 0.5. CW test results were less conclusive.

Thermal Conductivity of Nanolaminates

Our XRD and AFM data indicate that the nanolaminates have significantly reduced crystallinity. In addition, our laser damage studies show that the nanolaminates have reduced damage resistance to CW and 60 ns pulsed laser radiation. This is an interesting

result because prior research on shorter pulse laser illumination has found the opposite dependence for nanolaminates using 1 ns 1064 nm pulses in [18], where nanolaminates had increased damage resistance. It is known that less crystalline hafnia and titania thin films also have reduced thermal conductivity [27]. In our own prior work, we measured the crystallinity and thermal conductivity of hafnia nanolaminate and uniform ALD films [20]. We found that the uniform hafnia films had a thermal conductivity of 1.72 W/m K while the hafnia/alumina nanolaminate films had a thermal conductivity of 1.02 W/m K. Data on titania nanolaminate and uniform ALD films is not available at this time, but it is reasonable to expect a similar relationship.

In addition to film thermal conductivity, film thermal expansion differences are known to affect laser damage resistance [28]. However, recent studies have implied that nanolaminates behave less like thin film multilayers and more like uniform amorphous materials with respect to stress and strain [29,30]. Nevertheless, film stress and thermal expansion should be measured in future work. These results may indicate that in the CW regime, pure heat transfer effects begin to dominate high-field damage mechanisms and the impact of light scattering may be relatively less.

Currently, we are using the 3-omega method to measure the thermal conductivity of the titania and hafnia uniform and nanolaminate films. Preliminary results put the titania film in the range of 1.3 W/m-K and the titania nanolaminate in the range of 0.7 W/m-K. Substrate conductivity is used to give more credence to results. In both these experiments, the substrate conductivity was measured at approximately 130 W/m-K (instead of 149 W/m-K, a typical number for the silicon substrates). This may imply that the thermal conductivities measured were underestimates.

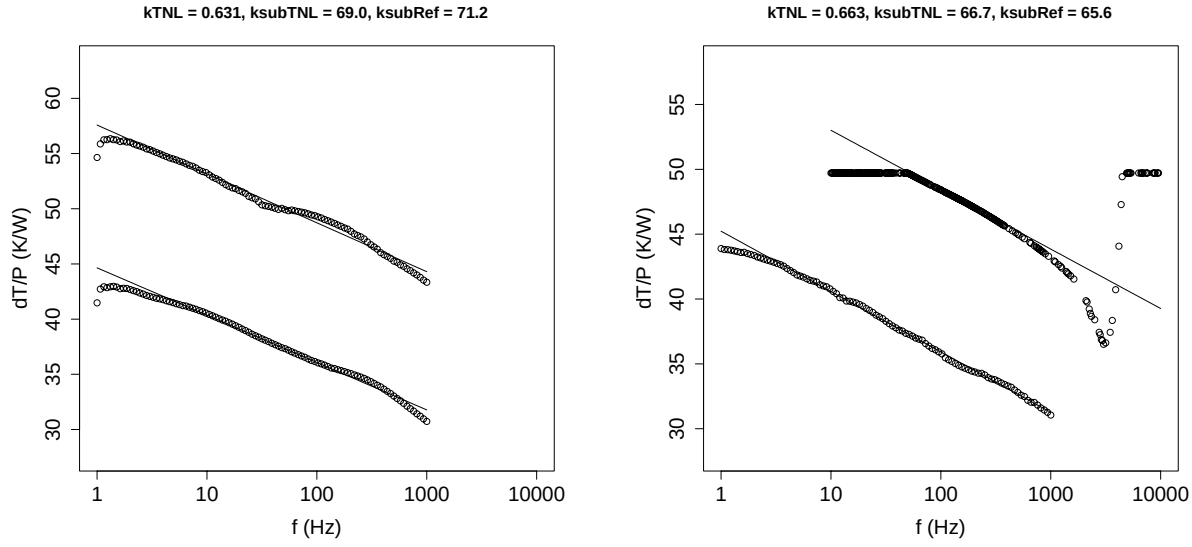


*Figure 11 - Three omega test results for titania nanolaminate films with input powers of 14 mW (left) and 32 mW(right) displaying similar 3-omega response.*

**References**


S. Chao, W.-H. Wang, M.-Y. Hsu, and L.-C. Wang, J. Opt. Soc. Am. **16**, 1477–1483 (1999).
R. Tateno, H. Okada, T. Otobe, K. Kawase, J. K. Koga, A. Kosuge, K. Nagashima, A. Sugiyama, and K. Kashiwagi, J. Appl. Phys. **112**, 123103 (2012).
B. C. Stuart, M. D. Feit, S. Herman, A. M. Rubenchik, B. W. Shore, and M. D. Perry, Phys. Rev. B **53**, 1749–1761 (1996).
D. W. Fradin and M. Bass, Appl. Phys. Lett. **22**, 206–208 (1973).
D. W. Fradin and M. Bass, Appl. Phys. Lett. **23**, 604–606 (1973).
D. W. Fradin, E. Yablonovitch, and M. Bass, Appl. Opt. **12**, 700–709 (1973).
M. J. Soileau and M. Bass, IEEE J. Quantum Electron. **16**, 814–814 (1980).
D. W. Fradin, N. Bloembergen, and J. P. Letellier, Appl. Phys. Lett. **22**, 635–637 (1973).
B. C. Stuart, M. D. Feit, A. M. Rubenchik, B. W. Shore, and M. D. Perry, Phys. Rev. Lett. **74**, 2248–2251 (1995).
J. Zhao, X. Li, H. Liu, R. Jiang, Z. Liu, Z. Hu, H. Gong, and J. Fang, Appl. Phys. Lett. **74**, 1081–1083 (1999).
H. Qi, Q. Wang, X. Zhang, Z. Liu, Z. Liu, J. Chang, W. Xia, and G. Jin, J. Appl. Phys. **103**, 033106–033106–4 (2008).
K. H. Lee, W. S. Shin, and E. C. Kang, Appl. Opt. **52**, 2055–2061 (2013).
J. R. Palmer, Opt. Eng. **22**, 224435 (1983).
K. E. Puttick, R. Holm, D. Ristau, U. Natzschka, G. Kiriakidis, N. Garawal, E. Judd, D. Holland, D. Greening, N. Ellis, M. Wilkinson, M. Garcia Pamies, and C. Sanviti, Proc. SPIE **3244**, 188–198 (1998).
H. Gong, C. F. Li, and Z. Y. Li, Proc. SPIE **3578**, 576–583 (1999).
R. S. Shah, J. J. Rey, and A. F. Stewart, Proc. SPIE **6403**, 640305–640305 (2007).
S. S. Kim, N. T. Gabriel, W. S. Chan, and J. J. Talghader, Opt. Lett. **34**, 2162–2164 (2009).
S. Zaitsu, S. Motokoshi, T. Jitsuno, M. Nakatsuka, and T. Yamanaka, Jpn. J. Appl. Phys. **43**, 1034–1035 (2004).
D. M. Hausmann and R. G. Gordon, J. Cryst. Growth **249**, 251–261 (2003).
N. T. Gabriel and J. J. Talghader, J. Appl. Phys. **110**, 043526 (2011).
M. K. Poutous, A. J. Pung, P. Srinivasan, Z. A. Roth, and E. G. Johnson, Opt. Express **18**, 27764–27776 (2010).
A. Rosencwaig and J. B. Willis, Appl. Phys. Lett. **36**, 667–669 (1980).
T. W. Murray and J. W. Wagner, J. Appl. Phys. **85**, 2031–2040 (1999).
J. Chen, X. Ni, J. Lu, and B. Bian, Opt. Commun. **176**, 437–440 (2000).
J. F. Herbstman, A. J. Hunt, and S. M. Yalisove, Appl. Phys. Lett. **93**, 011112–011112–3 (2008).
H. Jiao, T. Ding, and Q. Zhang, Opt. Express **19**, 4059–4066 (2011).
S.-M. Lee, D. G. Cahill, and T. H. Allen, Phys. Rev. B **52**, 253–257 (1995).
R. R. Austin, R. Michaud, A. H. Guenther, and J. Putman, Appl. Opt. **12**, 665–676 (1973).
D. R. G. Mitchell, D. J. Attard, K. S. Finnie, G. Triani, C. J. Barbé, C. Depagne, and J. R. Bartlett, Appl. Surf. Sci. **243**, 265–277 (2005).
R. Raghavan, M. Bechelany, M. Parlinska, D. Frey, W. M. Mook, A. Beyer, J. Michler, and I. Utke, Appl. Phys. Lett. **100**, 191912–191912–4 (2012).

# AFOSR Deliverables Submission Survey

Response ID:6864 Data

1.

**Report Type**

Final Report

**Primary Contact Email**

**Contact email if there is a problem with the report.**

pszanton@uncc.edu

**Primary Contact Phone Number**

**Contact phone number if there is a problem with the report**

704-687-0056

**Organization / Institution name**

University of North Carolina at Charlotte

**Grant/Contract Title**

**The full title of the funded effort.**

(HEL-MRI) 3D Meta-Optics for High Energy Lasers

**Grant/Contract Number**

**AFOSR assigned control number. It must begin with "FA9550" or "F49620" or "FA2386".**

FA9550-10-1-0543

**Principal Investigator Name**

**The full name of the principal investigator on the grant or contract.**

Dr, Glenn Boreman

**Program Officer**

**The AFOSR Program Officer currently assigned to the award**

Dr. Jason Marshall

**Reporting Period Start Date**

09/30/2010

**Reporting Period End Date**

09/14/2016

**Abstract**

The research team was composed of University of North Carolina at Charlotte, Clemson University, University of Texas at Arlington, and University of Minnesota. The scope of this program was to change the way components are designed and fabricated for high energy laser (HEL) applications, engineering electromagnetic fields in 3D dielectric structures. We exploited various methods based on periodic and aperiodic electromagnetic modeling techniques to accurately determine the fields throughout the structures. We developed methods of optimizing the desired spatial, spectral and polarization properties for specific platforms representational of High Energy Laser Components. Fabrication of structures with this degree of complexity requires unique methods of lithographic processing, etching and deposition. Advanced deposition methods were explored to provide high quality coatings based on atomic layer deposition and enable the engineering of structures on a monolayer by monolayer basis, with particular attention to laser-damage mechanisms. Test-beds were used to demonstrate the concept functionality, including solid-state-laser and fiber-laser based HEL systems. From and educational perspective we created a virtual laboratory for 3D Meta-Optics. This program was effective in translating the concepts into course content, laboratories for experimentation, and more than 6 PhD's granted on related subjects.

**Distribution Statement**

**This is block 12 on the SF298 form.**

Distribution A - Approved for Public Release

**Explanation for Distribution Statement**

**If this is not approved for public release, please provide a short explanation. E.g., contains proprietary information.**

**SF298 Form**

**Please attach your SF298 form. A blank SF298 can be found here. Please do not password protect or secure the PDF The maximum file size for an SF298 is 50MB.**

sf0298_UNC Charlotte.pdf

**Upload the Report Document. File must be a PDF. Please do not password protect or secure the PDF . The maximum file size for the Report Document is 50MB.**

Final_report_complete.pdf

**Upload a Report Document, if any. The maximum file size for the Report Document is 50MB.**

**Archival Publications (published) during reporting period:**


1. Morgan, Kaitlyn, Keith Miller, Wenzhe Li, Yuan Li, Brandon Cochenour, and Eric Johnson. "Free Space Propagation of Concentric Vortices through Underwater Turbid Environments." In Propagation Through and Characterization of Atmospheric and Oceanic Phenomena, pp. W2A-3. Optical Society of America, 2016.
2. Baghdady, Joshua, Keith Miller, Kaitlyn Morgan, Matthew Byrd, Sean Osler, Robert Ragusa, Wenzhe Li, Brandon M. Cochenour, and Eric G. Johnson. "Multigigabit/
s underwater optical communication link using orbital angular momentum multiplexing." Optics express 24, no. 9 (2016): 9794-9805.
3. Li, Yuan, Wenzhe Li, J. Miller, and Eric G. Johnson. "Multiplexing and Amplification of 2 μm Vortex Beams with a Ho: YAG Rod Amplifier." (2016).
4. Yuan Li, Zeyu Zhang, Wenzhe Li, Keith Miller, and Eric Johnson, "Ho:YAG Rod Amplifier For High Order Vortex Modes," in Frontiers in Optics 2015, OSA Technical Digest (Optical Society of America, 2015), paper FTu3G.3.
5. Yuan Li, Zeyu Zhang, Wenzhe Li, Keith Miller, and Eric Johnson, "Simultaneous Amplification of Multiple 2 μm Vortex Beams," in Advanced Solid State Lasers, OSA Technical Digest (online) (Optical Society of America, 2015), paper ATu2A.45.
6. Yuan Li, Zeyu Zhang, J. Keith Miller, and Eric Johnson. "Ho: YAG rod amplifier for vortex beams." In Photonics Conference (IPC), 2015, pp. 321-322. IEEE,
2015.
7. Keith Miller, Yuan Li, Wenzhe Li, Ramesh Shori, and Eric Johnson. "Pulsed Amplification of 2 μm Concentric Vortex Beams." In CLEO: Science and Innovations, pp. STu1M-7. Optical Society of America, 2016.
8. Guoliang Chen; Kyu Jin Lee; Robert Magnusson, "Periodic photonic filters: theory and experiment," Optical Engineering 55(3), 037108 (2016). doi:
10.1117/1.OE.55.3.037108.
9. 2. Jae Woong Yoon, Seok Ho Song, and Robert Magnusson, "Critical field enhancement of asymptotic optical bound states in the continuum," Scientific Reports, vol. 5, article no. 18301, pp. 1–8, November 22, 2015. doi:
10.1038/srep18301 (2015).
10. A. Sincore, J. Cook, W. Li, E. Johnson, J. Bradford, L. Shah, M. Richardson, "Beam propagation of Gaussian and Annual Beams at 2 μm in the presence of thermal lensing," CLEO Science and Innovations 2016, paper JTh2A.77
11. L. N. Taylor and J. J. Talghader, "Subsampling phase retrieval for rapid thermal measurements of heated microstructures," Optics Letters, vol. 41, pp. 3189–3192,
2016.
12. P. R. Armstrong, M. L. Mah, K. D. Olson, L. N. Taylor, and J. J. Talghader, "Reduction of thermal

emission background in high temperature microheaters,"
Journal of Micromechanics and Microengineering, vol. 26, 055004, 2016.
13. Byrd, M.; Pung, A.; Johnson, E.; Kyu Lee; Magnusson, R.; Binun, P.; McCormick, K., "Wavelength Selection and Polarization Multiplexing of Blue Laser Diodes," in Photonics Technology Letters, IEEE , vol.27, no.20, pp.2166-2169, Oct.15, 15 2015
14. Indumathi Raghu Srimathi, Yuan Li, William F. Delaney, and Eric G. Johnson,"Subwavelength grating based metal-oxide nano-hair structures for optical vortex
generation," Opt. Express 23, 19056-19065 (2015)
15. Li, Yuan, Zeyu Zhang, Wenzhe Li, Jerome Miller, and Eric Johnson. "Ho: YAG Rod Amplifier ForHigh Order Vortex Modes." In Frontiers in Optics, pp. FTu3G-3. Optical Society of America, 2015.
16. Li, Yuan, Zeyu Zhang, Wenzhe Li, Keith Miller, and Eric Johnson. "Simultaneous Amplification of Multiple 2 μm Vortex Beams." In Advanced Solid State Lasers, pp. ATu2A-45. Optical Society of America, 2015.
17. A. Brown, A. Ogloza, L. Taylor, J. Thomas, and J. Talghader, "Continuous wave laser damage and conditioning of particle-contaminated optics," Applied Optics,
vol. 54, no. 16, pp. 5216-5222, 2015.
18. E. McKee, E. Maddox, L. Shah, R. Gaume, M. Richardson, "Rapid thermooptical quality assessment of laser gain media," C.C.C. Willis, J.D. Bradford, J.
Haussermann, Optical Materials Express 5, 6 (2015) 1389-1398.
19. L. Shah, R.A. Sims, P. Kadwani, C.C.C. Willis, J.B. Bradford, A. Sincore, M. Richardson, "High-power spectral beam combining of linearly polarized Tm:fiber lasers," Applied Optics 54, 1 (2015) 757-762.
20. Byrd, M.; Woodward, R.; Pung, A; Johnson, E.; Lee, K.; Magnusson, R.; McCormick, K.; Binun, P., "Blue laser diode wavelength selection with a variable
reflectivity resonant mirror," Photonics Technology Letters, IEEE (2014).
21. Kyu J. Lee, Jerry Giese, Laura Ajayi, Robert Magnusson, and Eric Johnson, "Resonant grating polarizers made with silicon nitride, titanium dioxide, and
silicon: Design, fabrication, and characterization," Opt. Express 22, 9271-9281 (2014).
22. M. Gebhardt, C. Gaida, P. Kadwani, A. Sincore, N. Gerlich, L. Shah, M. Richardson, "High peak power mid-IR ZnGeP2 optical parametric oscillator pumped by Tm:fiber master oscillator power amplifier system," Opt. Lett 39
1212-1215 (2014).
23. Lucas N. Taylor, Andrew K. Brown, Aaron J. Pung, Eric G. Johnson, Joseph J. Talghader, "Continuous-wave laser damage of uniform and nanolaminate hafnia and titania optical coatings," Optics Letters, vol. 38, no. 21 pp. 4292-4295, Nov 1, 2013.
24. Indumathi Raghu Srimathi, Aaron J. Pung, Yuan Li, Raymond C. Rumpf, and Eric G. Johnson, "Fabrication of metal-oxide nano-hairs for effective index optical elements," Opt. Express 21, 18733-18741 (2013).
25. Pung, A. J., Srimathi, I. R., Li, Y., & Johnson, E. G. (2013, September). Fabrication Method for Encapsulation of Low-Index, Narrowband Guided-Mode Resonance Filters. In Photonics Conference (IPC), 2013 IEEE (pp. 227-228).
IEEE.
26. Pung, A. J., Carl, S. R., Srimathi, I. R., & Johnson, E. G. (2013). Method of fabrication for encapsulated polarizing resonant gratings. IEEE Photon. Technology Letters, 25(15), 1432-1434.
27. L. N. Taylor, A. K. Brown, A. J. Pung, E. G. Johnson, and J. J. Talghader, "Laser Damage of Nanolaminate HfO2 and TiO2 Optical Coatings," Technical Digest of the 2013 OSA Optical Interference Coatings Conference, Whistler, British Columbia, Canada, June 2013, 3 pages.
28. Robert Magnusson, Tanzina Khaleque, and Mohammad J. Uddin, "Optical filters enabled by the Rayleigh anomaly: Theory and experiment," IEEE Photonics Conference 2013, Bellevue, Washington, September 8–12, 2013.
29. Robert Magnusson, "Flat-top resonant reflectors with sharply delimited angular spectra: an application of the Rayleigh anomaly," Optics Letters, vol. 38, no. 6,
pp. 989–991, March 15, 2013.
30. Yuan Li; Srimathi, I.R.; Woodward, R.H.; Pung, A.J.; Poutous, M.K.; Shori, R.K.; Johnson, E.G., "Guided-

Mode Resonance Filters for Wavelength Selection in Mid-Infrared Fiber Lasers," Photonics Technology Letters, IEEE , vol.24, no.24, pp.2300,2302, Dec.15, 2012.
31. Indumathi Raghu Srimathi, Menelaos K. Poutous, Aaron J. Pung, Yuan Li, Ryan H. Woodward, Eric G. Johnson, and Robert Magnusson, "Mid-Infrared Guided Mode Resonance Reflectors for Applications in High Power Laser Systems,"
IEEE Photonics Conference 2012, Burlingame, California, September 23–27, 2012
32. Yuan Li, Ryan H. Woodward, Indumathi Raghu Srimathi, Aaron J. Pung, Menelaos K. Poutous, Eric G. Johnson, and Ramesh Shori," 2.78 μm Fluoride Glass Fiber Laser Using Guided Mode Resonance Filter as External Cavity Mirror," IEEE Photonics Conference 2012, Burlingame, California, September 23–27, 2012.
33. K. J. Lee, J. Giese, I. L. Ajayi, R. Magnusson, and E. Johnson, "Resonant dielectric-grating polarizers for normal incidence operation," IEEE Photonics Conference 2012, Burlingame, California, September 23–27, 2012, paper MX2.
34. Lawrence Shah, R. Andrew Sims, Pankaj Kadwani, Christina C.C. Willis, Joshua, B. Bradford, Aaron Pung, Menelaos K. Poutous, Eric G. Johnson, and Martin
Richardson, "Integrated Tm:fiber MOPA with polarized output and narrow line width with 100 W average power," Opt. Express 20, 20558-20563 (2012).
35. Roth, Z.A., Srinivasan, P., Poutous, M.K., Pung, A.J., Rumpf, R.C., Johnson, E.G." Azimuthally Varying Guided Mode Resonance Filters." Micromachines, 3,
180-193 (2012).
36. Pung, M. Poutous, R. Rumpf, Z. Roth, and E. Johnson, "Monolithic, Low-index Guided-mode Resonance Filters: Fabrication and Simulation," in Optical Fabrication and Testing, OSA Technical Digest (online) (Optical Society of America, 2012), paper OTu4D.6.
37. Yuan Li, Ryan H. Woodward, Indumathi Raghu Srimathi, Menelaos K. Poutous, Ramesh K. Shori, and Eric G. Johnson, "Guided mode resonance filter as wavelength selecting element in Er:ZBLAN fiber laser," 2012 OSA Specialty Optical Fibers (SOF) Topical Meeting, 1361447.
38. Indumathi Raghu, Menelaos K. Poutous, Aaron Pung, Yuan Li, Ryan Woodward, and E. G. Johnson, "Design and Fabrication of Mid-IR Guided Mode Resonance Filters," 2012 OSA Integrated Photonics Research, Silicon and Nano Photonics (IPR) Topical Meeting, 1361387.
39. Robert Magnusson, "Spectrally dense comb-like filters fashioned with thick guided-mode resonant gratings," Optics Letters, vol. 37, no. 18, pp. 3792-3794,
September 15, 2012.
40. K. J. Lee, J. Curzan, M. Shokooh-Saremi, and R. Magnusson, "Guided-Mode Resonance Polarizers With 200-nm Bandwidth," Optical Society of America Frontiers in Optics, OSA's 95th Annual Meeting, San Jose, California, October 16–20, 2011; published in Frontiers in Optics, OSA Technical Digest, paper FWU2.
41. Kyu J. Lee, James Curzan, Mehrdad Shokooh-Saremi, and Robert Magnusson, "Resonant wideband polarizer with single silicon layer," Applied Physics Letters, vol. 98, no. 21, pp. 211112-1–211112-3, May 25, 2011.
42. Aaron J. Pung, Menelaos K. Poutous, Raymond C. Rumpf, Zachary A. Roth, and Eric G. Johnson, "Two-dimensional guided mode resonance filters fabricated in a uniform low-index material system," Opt. Lett. 36, 3293-3295 (2011).
43. Pung, M. Poutous, Z. Roth, and E. Johnson, "Fabrication of Low Contrast Homogenous Guided Mode Resonance Filters," in CLEO:2011 - Laser Applications to Photonic Applications, OSA Technical Digest (CD) (Optical
Society of America, 2011), paper JTuI24.
44. N. T. Gabriel and J. J. Talghader, "Thermal onductivity and refractive index of hafnia-alumina nanolaminates," Journal of Applied Physics, vol. 110, 043526 (2011); doi:10.1063/1.3626462 (8 pages).
45. Menelaos K. Poutous, Aaron Pung, Pradeep Srinivasan, Zachary Roth, Eric G. Johnson, "Polarization selective, graded-reflectivity resonance filter, using a space-varying guided-mode resonance structure," Optics Express 2010, Vol. 18, No. 26, 27764-27776 (Dec 2010).

**New discoveries, inventions, or patent disclosures:**

**Do you have any discoveries, inventions, or patent disclosures to report for this period?**

No

**Please describe and include any notable dates**

**Do you plan to pursue a claim for personal or organizational intellectual property?**

**Changes in research objectives (if any):**

None

**Change in AFOSR Program Officer, if any:**

None

**Extensions granted or milestones slipped, if any:**

No-cost extension granted to extend period of performance from 62 months to 71.5 months.

**AFOSR LRIR Number**

**LRIR Title**

**Reporting Period**

**Laboratory Task Manager**

**Program Officer**

**Research Objectives**

**Technical Summary**

**Funding Summary by Cost Category (by FY, $K)**

| | Starting FY | FY+1 | FY+2 |
|---|---|---|---|
| Salary | | | |
| Equipment/Facilities | | | |
| Supplies | | | |
| Total | | | |

**Report Document**

**Report Document - Text Analysis**

**Report Document - Text Analysis**

**Appendix Documents**

## 2. Thank You

**E-mail user**

Sep 13, 2016 09:24:39 Success: Email Sent to: pszanton@uncc.edu